UNIVERSITE DE MONTREAL

THE INVERSE PROBLEM OF ELECTROCARDIOGRAPHY: RECOVERY AND VALIDATION USING FINITE ELEMENT METHOD IN MAN

par

Abolfazl VAHID SHAHIDI
INSTITUT DE GENIE BIOMEDICAL
ECOLE POLYTECHNIQUE
et
UNIVERSITE DE MONTREAL

THESE PRESENTEE EN VUE DE L'OBTENTION
DU GRADE DE PHILOSOPHIAE DOCTOR (PH.D.)

JULY 1991

©Abolfazl Vahid Shahidi 1991

National Library of Canada
Bibliothèque nationale du Canada

Canadian Theses Service
Service des thèses canadiennes

Ottawa, Canada
K1A 0N4

The author has granted an irrevocable non-exclusive licence allowing the National Library of Canada to reproduce, loan, distribute or sell copies of his/her thesis by any means and in any form or format, making this thesis available to interested persons.

L'auteur a accordé une licence irrévocable et non exclusive permettant à la Bibliothèque nationale du Canada de reproduire, prêter, distribuer ou vendre des copies de sa thèse de quelque manière et sous quelque forme que ce soit pour mettre des exemplaires de cette thèse à la disposition des personnes intéressées.

The author retains ownership of the copyright in his/her thesis. Neither the thesis nor substantial extracts from it may be printed or otherwise reproduced without his/her permission.

L'auteur conserve la propriété du droit d'auteur qui protège sa thèse. Ni la thèse ni des extraits substantiels de celle-ci ne doivent être imprimés ou autrement reproduits sans son autorisation.

ISBN 0-315-69597-8

Canada

Université de Montréal
Ecole Polytechnique

Cette thèse intitulée:

The inverse problem of electrocardiography: recovery and validation using finite element method in man

présentée par Abolfazl Vahid Shahidi

en vue de l'obtention du grade de Philosophiae Doctor (Ph.D.)
a été dûment acceptée par le jury d'examen constitué de :

M. Ramesh M. Gulrajani, Ph.D., président
M. Pierre Savard, Ph.D., directeur
M. B. Milan Horáček, Ph.D., membre
M. L. Joshua Leon, Ph.D., membre

Dedicated to:

my wife, Soudabeh,

for her friendship, support and understanding,

my daughter, Golta,

my son, Faraz.

Abstract

The main objective of the present study is to develop and validate different techniques for the recovery of epicardial potential distributions from measured thoracic potentials in man. This problem is known as the inverse problem of electrocardiography. The solution to this problem is based on a torso model which describes the relation between the epicardial potentials and the body surface potentials. The forward modeling was based on *matched-realistic geometry*: a high resolution geometrical model of the human thorax was constructed using anatomical data measured by CT scans in a patient with the Wolff-Parkinson-White syndrome whose epicardial and body potentials were available. Two sets of models were prepared using the finite element method. The first set had a mesh resolution of 5517 nodes and 29810 elements with four different inhomogeneity distributions, the models from the second set consisted of 12084 nodes and 67045 elements with four inhomogeneity distributions.

Forward simulations using these models were performed using different excitation sites on the epicardial surface. The inclusion of the inhomogeneities altered the maximum and minimum values of the body surface potentials but did not substantially modify the pattern of the potential distributions. The greatest effect was due to the addition of the lungs, compared with the spinal region inhomogeneity which produced only minor changes. Increasing the mesh resolution from 5517 to 12084 nodes did not change noticeably the shape or the amplitude of the simulated body surface potential maps.

A theoretical analysis of the stability of the inverse solutions after perturbation of the data and the transfer matrix was performed using singular function expansion. This showed that the condition number of the transfer matrix governs the

stability of the inversion problem and magnifies these perturbations. To solve the inverse problem, it is necessary to assure in some way the stability of the solutions. This was achieved by using the zero-order Tikhonov regularization method or *the control of dimensionality* which combines regularization and truncation. For each inverse method, three different nonlinear optimization procedures were used to find the optimal value of the regularization parameter or the truncation level. The implementation of these inverse procedures was validated by simulations.

Performance analysis of the inverse solutions was carried out in man. This is considered an important step towards a generalized application of the inverse procedure. The inverse epicardial maps reproduced the overall pattern of the measured maps during pre-excitation at the beginning of the QRS complex, with close extrema near the base of the lateral wall of the left ventricle. However, large relative errors (> 1) and low correlation coefficients (< 0.2) were measured. Two sources of errors related to the epicardial potential measurements could be responsible: the electrode location mismatch and the higher potential values at the air-exposed electrodes. Later during the QRS complex, none of the inverse methods were able to recover the complex fusion patterns with multiple breakthrough sites.

The control of dimensionality generally provided better results than the zero-order Tikhonov regularization method and it also showed some computational advantages. The choice of the estimator was found to be more important than the choice of the inverse method. The *bounded norm constraint* estimator provided the best results for both inverse methods when the maps were visually analysed. Measurement of the true conductivity values of the different inhomogeneities was found essential. No improvement in the inverse solutions occurred

with mesh refinement. Overall, clinically useful information such as the location of the pre-excitation site could be obtained from the inverse maps when the measured epicardial potential distributions were simple.

Sommaire

Le principal objectif de cette étude est de mettre au point et de valider différentes techniques pour le calcul des distributions de potentiels épicardiques à partir des potentiels mesurés sur le thorax chez l'homme. Ce probleme est connu sous le nom de problème inverse de l'électrocardiographie. La solution de ce problème est basée sur un modèle de torse qui décrit la relation entre les potentiels épicardiques et les potentiels thoraciques. Un modèle géométrique à haute résolution d'un thorax humain a été construit en utilisant des données anatomiques mesurées par tomographie sur un patient qui présentait le syndrome de Wolff-Parkinson-White et dont les potentiels épicardiques et thoraciques étaient disponibles. Deux séries de modèles ont été préparées en utilisant la méthode des éléments finis. La première série avait une résolution du treillis de 5517 noeuds et 29810 éléments avec quatre distributions de conductivité différentes, et les modèles de la deuxième série comprenaient 12084 noeuds et 67045 éléments avec quatre distributions de conductivité.

Plusieurs simulations utilisant ces modèles ont été effectuées en utilisant différents sites d'excitation sur la surface épicardique. L'inclusion des inhomogènéités a altéré les valeurs maximales et minimales des potentiels thoraciques, mais n'a pas modifié de façon substantielle le patron des distributions de potentiel. Le plus grand effet a été dû à l'addition des poumons. L'augmentation de la résolution de 5517 à 12084 noeuds n'a pas changé de façon notable la forme ou l'amplitude des potentiels thoraciques simulés.

Une analyse théorique de la stabilité des solutions inverses après perturbations des données et de la matrice de transfert a été effectuée en utilisant l'expansion en fonctions singulières. Cela a démontré que le nombre de conditionnement

de la matrice de transfert affecte la stabilité du problème d'inversion et amplifie ces perturbations. Pour résoudre le problème inverse, il est nécessaire d'assurer la stabilité des solutions. Cela a été accompli en utilisant la méthode de régularisation d'ordre zéro de Tikhonov, ou le contrôle de la dimensionnalité qui combine la regularisation et la troncation. Pour chaque méthode d'inversion, trois procédures d'optimisation non-linéaires différentes furent utilisées pour trouver la valeur optimale du paramètre de régularisation ou du niveau de troncation. L'implémentation de ces procédures inverses a été validée par des simulations.

L'analyse de la performance des solutions inverses a été accomplie chez l'humain malgré de nombreuses difficultés. Ceci est considéré comme étant un pas important vers une application généralisée de la procédure inverse. Les cartes épicardiques inverses ont reproduit les patrons généraux des cartes mesurées durant la pré-excitation au début du complexe QRS, avec des extrema situés près de la base de la paroi latérale du ventricule gauche. Cependant, des erreurs relatives importantes (> 1) et des coefficients de corrélation faibles (< 0.2) ont été mesurés. Deux sources d'erreur reliées aux mesures des potentiels épicardiques pourraient être responsables: un mauvais positionnement des électrodes, et des valeurs plus grandes de potentiel aux electrodes exposées à l'air. Par après, durant le reste du complexe QRS, aucune des méthodes d'inversion n'a été capable d'estimer les patrons complexes de fusion avec de sites multiples d'émergence de l'activation.

Le contrôle de la dimensionnalité a généralement produit de meilleurs résultats que la méthode de régularisation d'ordre zéro de Tikhonov, et a montré quelques avantages au niveau du calcul. Le choix de l'estimateur a une importance plus grande que le choix de la méthode d'inversion. L'estimateur qui fixe une contrainte sur l'amplitude de la norme a produit les meilleurs resultats pour les deux

méthodes d'inversion lorsque les cartes sont analysées visuellement. La mesure de nouvelles valeurs de conductivité pour des différentes inhomogénéités est estimée comme étant essentielle. Il n'y a pas eu d'amélioration dans les solutions inverses lors du raffinement du treillis. Finalement, des informations cliniques utiles comme la position du site de pré-excitation ont pu être fournies par les cartes inverses dans le cas où les distributions de potentiel epicardiques mesurées étaient simples.

Acknowledgments

I would like to express my sincere gratitude to Dr. P. Savard. I gratefully thank him for his invaluable guidance and encouragement in planning this study and preparing this thesis. Thanks are also extended to Dr. F.A. Roberge for his moral support and helpful advice.

I wish to thank Dr. R.A. Nadeau for his helpful clinical discussions and providing the patient. I am also grateful to the patient who voluntarily participated in this study. The Department of Radiology at Sacré-Coeur Hospital is well appreciated for preparing the CAT scan data.

I wish to express my appreciation to Dr. P.P. Silvester, McGill University, for his helpful suggestions on the modeling and computational aspects. I would like to thank Dr. R.M. Gulrajani for his technical advice and other members of the Ph.D. thesis jury for their constructive comments. I also wish to acknowledge colleagues and fellow graduate students who kindly shared their experience and generously offered their help.

Both the technical and secretarial staff provided me with their usual friendly effectiveness, making my stay at Université de Montréal and Sacré-Coeur Hospital all the more pleasant in the process.

The financial support of the Laboratoire de Modélisation Biomédicale de l' Université de Montréal is gratefully acknowledged.

Table of Contents

Abstract v

Sommaire viii

Acknowledgments xi

Table of contents xii

List of figures xvi

Table of Symboles and Abreviations xxv

1 Introduction **1**

1.1 The forward problem of electrocardiography 3

1.1.1 Review of the literature 3

1.2 The inverse problem of electrocardiography 6

1.2.1 Review of the literature 6

1.3 Purpose of this study 10

1.4 Thesis outline 11

2 The forward problem: modeling **12**

2.1 Biophysics of the problem region 12

2.1.1 Structural features 13

2.1.2 Material properties 13

2.2 Construction of the heart-torso model 14

2.3 Model formulation 20
2.3.1 The source model 20
2.3.2 Governing equations 20
2.3.3 Boundary conditions. 21
2.3.4 Finite-element formulation 21
2.3.5 Global transfer matrix 25
2.4 Model construction and field computation 26

3 The forward problem: validation and field solutions 34
3.1 Model validation 34
3.1.1 Solid cylinder with a prescribed source 35
3.1.2 Model convergence 36
3.2 The field solution of the human heart-torso model 42
3.2.1 Potential distributions 42
3.2.2 Electric field maps 57

4 The inverse problem: theory and methods 61
4.1 Mathematical description of the problem 61
4.2 Stability analysis and limitations 64
4.2.1 Singular function expansion 65
4.2.2 Perturbations 67
4.2.3 Spectral analysis of the signal matrix 70
4.2.4 Resolution limits 71
4.3 Methodologies of solution 73
4.3.1 Tikhonov regularization 76
4.3.2 Resolution by control of dimensionality 78

4.3.3 Estimators and the discrepancy principle 80
4.3.4 Search schema 83
4.3.5 Determination of the transfer matrix 83

5 The inverse problem: computational analysis 86

5.1 Performance criteria 86
5.1.1 Accuracy criteria 87
5.1.2 Performance indices 89
5.2 The measured potential data 89
5.3 The heart prototype 91
5.4 SVD analysis of the heart-torso models 92
5.5 Spectral analysis of signal matrices 95
5.6 Inverse simulations 97
5.6.1 Inverse simulation using the epicardial potentials (InvSim-1) 101
5.6.2 Inverse simulations using the torso potentials (InvSim-2) . . 108

6 The inverse problem: validation with measured epicardial potentials 114

6.1 Spatial inverse solutions 115
6.1.1 Regularization 115
6.1.2 Control of dimensionality 115
6.1.3 Recovered maps 116
6.1.4 Evaluation of the results 118
6.2 Temporal inverse solutions 131
6.2.1 Regularization 134
6.2.2 Control of dimensionality 135

6.2.3 Recovered electrograms 135

6.2.4 Evaluation of the results 139

6.3 Performance analysis of the spatial and temporal inverse solutions 140

7 Conclusion **146**

References **151**

APPENDIX **161**

A Shape functions and simplex coordinates **161**

A.1 Shape functions 161

A.2 Simplex coordinates 162

B Coordinate transformation and integral formulas **165**

C Analytical solution of potential distribution for a solid cylinder **167**

D Forward simulations **170**

E Transfer matrix **178**

List of figures

2.1 X-ray image and the position levels where x-ray CT images were taken from a patient. 16

2.2 Cross-sectional image of the patient shown in Fig. 2.1. The image corresponds to a transverse section through the thorax at the level of 24cm below the neck. 17

2.3 The topological volumes constructed from two consecutive cross-sectional images at (top) z= 24 and 25, (bottom) z= 29 and 30. The global coordinate system is shown in the lower left corner. . . 27

2.4 The finite element volumes for $HLST_1$ constructed using the topological volumes of Fig. 2.3. 28

2.5 The finite element volumes for $HLST_2$ constructed using the topological volumes of Fig. 2.3. 29

2.6 Cross-section of the thorax T_1 model cut vertically. The external and internal surfaces are represented in orange and white, respectively. 30

2.7 Three views of the thorax model $HLST_2$. In (top) frontal view of the model of a WPW patient, with heart and lungs; the spinal region is not shown for clarity. In (bottom) left lateral view. (Continued) 31

2.7 (Continued) The model is seen from above. 32

2.8 The data processing flow for the 3-D modeling and analysis, using a CT scanner, PATRAN and MagNet3D application interfaces. . . 33

3.1 A cylindrically shaped volume conductor, modeled by FEM for validation purposes. This is the fine mesh model. 36

3.2 Contours of potentials on the outer surface of the cylinder calculated by FEM. 37

3.3 Computed isopotential fringes for a cylindrically shaped body on the vertical cross-sections parallel to the $x-z$ plane for: (top) coarse (363 nodes), (bottom) medium (803 nodes) models. (Continued) . 38

3.3 (Continued) Fine (1358 nodes) model. 39

3.4 Computed body surface potentials for the cylindrically shaped model. Symbols: (–) analytical, (- -) FEM. 40

3.5 Convergence of the FEM solutions for different mesh resolutions. Symbols: (—) fine, (- -) medium and (- . -) coarse models. 41

3.6 Top: anterior view of the front of the heart cut at the base level, displaying the different activation locations over the heart surface at L_1, L_2, L_3, L_4 or L_5. LV: left ventricle, RV: right ventricle, LAD: left anterior descending artery. Bottom: Side view of the heart depicting the the excitation L_1. 44

3.7 Computed body surface fringe maps on (top) anterior view and (bottom) posterior view. These were obtained using the T_1 model with the activation of the heart surface at location L_1. 47

3.8 Computed body surface fringe maps as in Figure 3.7 for the LT_1 model and the activation at location L_1. 48

3.9 Computed body surface fringe maps as in Figure 3.7 for the $HLST_1$ model and the activation at location L_1. 49

3.10 Computed body surface fringe maps as in Figure 3.7 for the $HLST_1$ model the activation at location L_2. 50

3.11 Computed body surface fringe maps as in Figure 3.7 for the $HLST_1$ model and the activation at location L_3. 51

3.12 Computed body surface fringe maps as in Figure 3.7 for the $HLST_1$ model and the activation at location L_4. 52

3.13 Computed body surface fringe maps as in Figure 3.7 for the $HLST_1$ model and the activation at location L_5. 53

3.14 Computed body surface fringe maps as in Figure 3.7 for the T_2 model and the activation at location L_1. 54

3.15 Computed body surface fringe maps as in Figure 3.7 for the LT_2 model and the activation at location L_1. 55

3.16 Computed body surface fringe maps as in Figure 3.7 for the $HLST_2$ model and the activation of heart surface at location L_1. 56

3.17 Isopotential fringes displayed on the heart and lungs calculated with FEM as in Figure 3.7 for the $HLST_1$ model and the activation of heart surface at location L_1. 58

3.18 Calculated isopotential contours displayed on the frontal surface of the thorax and on a cross-section cut at about $1cm$ above the base of the heart. 59

3.19 Top: anterior view of the T_1 model. Computed isofield map of electric field intensity due to the activation shown in Fig. 3.18. Bottom: side view showing the vector field across the heart boundary. 60

5.1 Magnitude of time-aligned RMS signals for the 63 epicardial and 63 thoracic leads from the patient who suffered from WPW syndrome; thoracic CAT scans were obtained from the same patient. 91

5.2 The heart prototype and the sock electrode array which was used to measure the epicardial potential distribution. 92

5.3 Decay characteristic of the singular values for the transfer matrices of the different heart-torso models. The curves are defined as: (–) T_1, (- -) LT_1, (x) $HLST_1$, (+) T_2, (o) LT_2 and (*) $HLST_2$. The inset is shown with a larger scale at the bottom. 94

5.4 Decay of the singular values (logarithmic scale) of the transfer matrix of the $HLST_1$ model showing three regions with distinct rate of change. 95

5.5 Decay of the singular values (logarithmic scale) of the signal matrices for the epicardium (*) and the torso (o). 96

5.6 First 8 principal components in time, as produced by the SVD analysis of the epicardial potential matrix. 98

5.7 First 8 principal components in space, as produced by the SVD analysis of epicardial potential matrix. The maps are represented in a polar format as shown in Fig. 3.6. The thicker lines represent the zero lines. 99

5.8 Time course of the magnitude for the 63 leads of the measured (–) and recovered (o) epicardial potentials in InvSim-1 for the $HLST_2$ model using the TikReg inverse method with the OPT estimator. . 104

5.9 Isopotential lines representing the measured epicardial potentials (left-side) and those computed by solving the inverse problem in InvSim-1 (right-side). The maps are represented in a polar format introduced in Fig. 3.6. 105

5.10 Comparison between the measured (–) and computed (o) electrograms at four different lead locations on the epicardium. Inverse simulation-1 was used; electrode sites were: left posterior (top-left); left anterior (top-right); right anterior (bottom-left) sites on the base; and (bottom-right) on the apex of the heart using the $HLST_1$ model with the DimCon inverse method. 106

5.11 Time course of the magnitude of the measured (–) and recovered (o) potentials in inverse simulation-2 for the $HLST_2$ model using the TikReg inverse method with the OPT estimator. 110

5.12 Isopotential lines representing the measured thoracic potentials (left-side) and those computed by the inverse simulation-2 procedure (right-side). The maps are represented in a rectangular format with the anterior torso on the left and posterior torso on the right of each map. 111

6.1 Epicardial maps drawn at every $10ms$ during the QRS complex for the patient with WPW syndrome. Maps are drawn in a polar format, with the apex at the center and the base on the circumference. The right ventricle (RV) corresponds to the upper half of the maps and the left ventricle (LV) to the lower half. The interval between isopotential lines is indicated in the lower left corner of each map. The values of the maximum and minimum are indicated under each map (in mv). 119

6.2 Comparison between the measured (top) and inverse epicardial maps at 20 ms (left- and right-side). The computed maps were recovered using the T_1 model. The map on the top is the measured one, the maps on the left are those obtained using the TikReg inverse method and the maps on the right are those obtained using DimCon with their corresponding estimators. 120

6.3 Comparison between the measured (top) and inverse epicardial maps at 20 ms (left- and right-side). The computed maps were recovered using the $HLST_1$ model. 121

6.4 Comparison between the measured (top) and inverse epicardial maps at 20 ms (left- and right-side). The computed maps were recovered using the $HLST_2$ model. 122

6.5 Comparison between the measured (top) and inverse epicardial maps at $50ms$ (left- and right-side). The computed maps were recovered using the T_1 model. 123

6.6 Comparison between the measured (top) and inverse epicardial maps at $50ms$ (left- and right-side). The computed maps were recovered using the $HLST_1$ model. 124

6.7 Comparison between the measured (top) and inverse epicardial maps at $50ms$ (left- and right-side). The computed maps were recovered using the $HLST_2$ model. 125

6.8 Time course of the magnitude of the measured (–) and recovered epicardial potential using the T_1 (o) and $HLST_1$ (- -) models with the TikReg inverse method and the BNC estimator. 129

6.9 Temporal behavior of the RMSD between the measured body surface maps and those computed from recovered epicardial potentials for the T_1 model using TikReg and DimCon inverse methods with BNC (–), OPT (- -), CRESO (-.-) and AIC (o) estimators. 130

6.10 Time course of the correlation coefficient of the epicardial maps using the T_1 model with the TikReg (–) and DimCon (- -) inverse methods with the BNC, OPT, CRESO and AIC estimators. 132

6.11 Temporal behavior of the relative error of the epicardial maps using the T_1 model with the TikReg (–) and DimCon (- -) inverse methods with the BNC, OPT, CRESO and AIC estimators. 133

6.12 Temporal behavior of logarithm of the regularization parameter (γ) as obtained using the TikReg inverse method with the BNC (–), OPT (- -), and CRESO (-.-) estimators using the T_1 model. 134

6.13 Time course of the optimum dimension level as obtained using the DimCon inverse method with the BNC (–), OPT (- -), and AIC (-.-) estimators using the T_1 model. 135

6.14 Comparison between the measured (- -) and recovered (–) epicardial electrograms for two lead locations, 32 and 27, using the T_1 model and the DimCon inverse method with the BNC, OPT and AIC estimators. The isopotential map measured at $20ms$ is shown for reference. 137

6.15 Comparison between the measured (- -) and recovered (–) epicardial electrograms for two lead locations, 3 and 15, using the T_1 model and the DimCon inverse method with the BNC, OPT and AIC estimators. The isopotential map measured at $50ms$ is shown for reference. 138

A.1 Tetrahedral element. 163

D.1 Measured thoracic isopotential maps at $10 - 100ms$ time intervals. The torso surface is represented in a rectangular format with the anterior torso surface on the left and the posterior torso surface on the right. 172

D.2 Simulated thoracic isopotential maps using the T_1 model and the measured epicardial maps at $10 - 100ms$ time intervals. 173

D.3 Simulated thoracic isopotential maps using the LT_1 model and the measured epicardial maps at $10 - 100ms$ time intervals. 174

D.4 Simulated thoracic isopotential maps using the $HLST_1$ model and the measured epicardial maps at $10 - 100ms$ time intervals. 175

D.5 Simulated thoracic isopotential maps using the T_2 model and the measured epicardial maps at $10 - 100ms$ time intervals. 176

D.6 Simulated thoracic isopotential maps using the LT_2 model and the measured epicardial maps at $10 - 100ms$ time intervals. 177

Table of Symbols and Abbreviations

∇^2	:	Laplacian operator
∇	:	Gradient operator
$\vec{n}$	:	Normal unit vector
$f(.)$	:	Continuous function
$\mathbf{f}$	:	Vector
$\mathbf{H}$	:	Matrix
$\mathcal{H}$	:	Integral operator
δ_n^0	:	Kronecker delta
$d\Omega$	:	Volume element
dS	:	Surface element
$\|\cdot\|$	:	L_2 norm
$\|\cdot\|_H$	:	H_2 norm
EM	:	Electromagnetic
ECG	:	Electrocardiography
LAD	:	Left anterior descending (artery)
SVD	:	Singular value decomposition
BEM	:	Boundary element method
FEM	:	Finite element method
σ_h	:	Conductivity of heart media (S/m)
σ_l	:	Conductivity of lungs media (S/m)
σ_s	:	Conductivity of spinal media (S/m)
σ_b	:	Conductivity of thorax media (S/m)
T_1	:	Homogeneous thorax model, 5517/29810 nodes/elements

LT_1	:	Thorax model with σ_l, 5517/29810 nodes/elements
HLT_1	:	Thorax model with σ_l and σ_h, 5517/29810 nodes/elements
$HLST_1$	:	Thorax model with σ_l, σ_h and σ_s, 5517/29810 nodes/elements
T_2	:	Homogeneous thorax model, 12084/67045 nodes/elements
LT_2	:	Thorax model with σ_l, 12084/67045 nodes/elements
HLT_2	:	Thorax model with σ_l and σ_h, 12084/67045 nodes/elements
$HLST_2$	:	Thorax model with σ_l, σ_h and σ_s, 12084/67045 nodes/elements
$InvSim$	:	Inverse simulation
ϕ_h	:	Measured epicardial potentials (μV)
ϕ_b	:	Measured body surface potentials (μV)
$\mathbf{\Phi}_h$	:	Measured epicardial potential vector
$\mathbf{\Phi}_b$	:	Measured body surface potential vector
ϕ_h^{γ}	:	Recovered epicardial potential for TikReg method (μV)
$\phi_h^{n,\gamma}$	:	Recovered epicardial potential for DimCon method (μV)
$BSPM$	:	Body surface potential map
N_t	:	Dimension of time instants
N_h	:	Dimension of epicardial potentials
N_b	:	Dimension of body surface potentials
$TikReg$	:	Zero-order Tikhonov regularization
$DimCon$	:	Dimensionality control with fixed $\gamma > 0$
γ	:	Regularization parameter
n	:	Truncation level
BNC	:	Bounded norm constraint
OPT	:	Optimal estimate
$CRESO$	:	Composite REsidual and Smooth Operator

AIC	:	Akaike information criterion
$RMSD$	:	Root-mean-square difference
RE	:	Relative error
CC	:	Correlation coefficient
$IRMSD$	:	Performance efficiency in terms of $RMSD$
IRE	:	Performance efficiency in terms of RE
ICC	:	Performance efficiency in terms of CC

Chapter 1

Introduction

The bioelectric sources arising during propagated activation of the heart produce electrical currents that flow in the surrounding conductive tissues. A consequence is the establishment of electrical potentials on the body surface. Recordings of these time-varying potentials are known as electrocardiograms (ECG). The ECG is one of the most useful non-invasive diagnostic tools in medicine. It can provide information about the function and state of the cardiac system.

Inverse problems are encountered in different areas of electromagnetic (EM) theory [7, 11]. Remote observations provide data about components of the conducted or scattered EM fields (amplitude, frequency, etc.) from which information about the sources which cause the EM fields, or the scattering, is sought. One such problem is also encountered in electrocardiography.

Problem definition. The determination of body surface potential distributions from measured or hypothesized epicardial potential distributions and conversely, the estimation of epicardial potentials from thoracic potential distributions, constitute respectively the *forward* and *inverse problems* of electrocardiography. The inverse problem of electrocardiography is a Cauchy problem for a

second order elliptic operator. Although this problem is ill-posed, since the observed data is incomplete, theoretically, a unique solution does exist [2].

Significance. The estimation of the epicardial potential distribution has physiological importance. It permits the direct interpretation of the underlying cardiac events in a fashion that is not possible from body surface potentials. Hence, solution of the inverse problem may facilitate identification of cardiac pathologies.

Although the solution of the inverse problem is theoretically possible, the complexity of the volume conductor in which the heart is embedded, in terms of geometry and material distribution, and the complex pattern of the spread of excitation in the heart render the solution very difficult. Uncertainties of electrode positions, the estimation of material distribution by constant conductivity values, measurement noise, geometric variations among individuals and the limited number of thoracic electrodes contribute to the uncertainty of any solution. Thus, any practical inverse solution needs to be stabilized or regularized using some predefined criteria or constraints. These issues of complexities and regularization are among those previously investigated [13, 43]. The feasibility of inverse procedure has been investigated on simulated and experimental data and encouraging results have been reported [6, 13, 73].

Despite many potential clinical applications, the inability to validate inverse solutions in man has hampered its clinical use in the past. The other major problem is the demand for a higher degree of resolution of the recovered information than current inverse procedures have provided. Before applying any inverse procedure in a clinical setting, these two problems should be addressed. In the present study, epicardial potential maps recorded during antiarrhythmia surgery [8] along

with carefully measured geometric data are used to validate inverse procedures in man. In addition, new software developments for solid modeling and computational analysis such as finite element method (*FEM*) software are applied to solve the forward problem of electrocardiography.

1.1 The forward problem of electrocardiography

The aims of the forward modeling and simulations are to study the basic biophysical processes which determine epicardial and body surface potentials, to examine the diagnostic capability of these potential distributions, and to obtain volume-conductor relationships to be used in the inverse problem. Different approaches to the forward problem, its mathematical developments and its applications can be found in recent review articles by Gulrajani et.al. [27, 28]. Considering different levels of solution, the forward problem can be divided into three categories : the first is used for the simulation of activation process at successive time instants during the cardiac cycle, the second category involves heart-torso modeling to determine body surface potential maps from epicardial potentials or equivalent cardiac sources. The third category involves combination of both previous problems.

1.1.1 Review of the literature

Methods of solution. One of the earliest methods used for solving the forward problem was analytic. In this approach, the solutions were confined to cases with a regular geometry such as cylinders and spheres. Another early method was analogue, in which the thorax was represented by physical means, such as an electrolytic tank. Both of these methods have provided useful insights. Later,

several numerical schemes were developed.

Biophysical modeling. In this approach, the determination of the transfer coefficients is based on electromagnetic theory and the volume-conductor properties, i.e., geometry and conductivity, of the region of interest. The conductive regions are represented either by boundary surfaces or volumes. The earliest approach utilized surface integral equations and formulated the foward problem in terms of the net charges that accumulate on each boundary surface element of the volume conductor [23]. An alternative surface integral equation was later introduced in which the potentials at these boundaries are derived without computing the surface charge density [3]. Both approaches formulate the problem as a Neumann type with prescribed equivalent heart generators and yield solid angle matrices. Later, Barr et al. [4] extended the integral equation formulation used in [3] to obtain the transfer coefficients which permitted the calculation of body surface potentials from the epicardial surface potentials instead of equivalent heart generators. This is a boundary element method (*BEM*) with mixed boundary conditions which satisfies both Dirichlet and Neumann boundary conditions. The modeling techniques based on surface integral equations were used extensively for model studies on the effects of geometry and conductivity parameters. They were also applied to reconstruct body surface potentials for *in vivo* experiments [Ramsey et.al. 1977] and to find transfer coefficients to be utilized for inverse solutions [Barr et.al. 1978]. More recently, the BEM, with linear polynomial interpolation over all elements was applied by Messinger-Rapport and Rudy for an eccentric sphere model and a realistic model [43].

Finite element method is based on the minimization of an energy function within the volume. It is mathematically equivalent to solving the governing equa-

tions for the electric field distribution. In this method, the volume conductor is discretized by a set of contiguous finite volume elements and can be adapted to an irregular geometry including regions of anisotropic conductivity. The FEM was first applied to solve the forward problem of electrocardiography in 1974 by Silvester and Tymchyshyn [61]. They used a clay reproduction of a human thorax to form the elements. Later, this method was applied in two dimensions (2-D) by Yamashita and Takahashi [72] and in three dimensions (3-D) by Kim [38], Yamashita and Takahashi [73] and Colli Franzone et.al. [13]. General differences between FEM and the integral equation techniques are: i) The integral equation formulations represent only the surfaces separating dissimilar materials, leaving the material and potential distributions in the volume implicit, and most assume that the potential or the potential gradient are constant on each surface element. ii) FEM, in the present work, describes the volume distribution of the material and utilizes a piecewise linear potential distribution inside each element in the volume. iii) Discretization of the problem region in the integral techniques is easier than in FEM. iv) The integrands involved in integral equation formulations tend toward infinity as the observer approaches the surface; however, they do converge. v) The integrands used in FEM are well behaved. vi) Integral equation formulations produce a full matrix; in contrast, FEM involves a higher number of nodes leading to a very sparse matrix. A recent study using a regular geometry suggests that integral equation and FEM approaches yield similar accuracies for forward simulations [64, 65].

Another formulation applied in biophysical modeling is based on the finite difference method. The advantage of this method is its simplicity. It uses regular meshing schemes to discretize the geometry. Therefore, this makes it difficult to

adapt to irregular geometries such as the human torso. Lo [40] and later Walker and Kilpatrick [70] used a finite difference scheme to discretize a 3-D realistic human geometry by 3-D resistor network.

Statistical analysis. This approach is based on estimation theory and uses a set of measured epicardial and body surface potential data. It utilizes parameter estimation techniques to obtain the coefficients of the transfer matrix without any hypothesis about the biophysical properties of the problem region, apart from a linearity hypothesis. In general, this approach requires *a priori* assumptions about the probability density functions involved. This approach was successfully applied by Herch et al. [31] using a Bayesian estimation technique from potential data measured in an intact dog.

1.2 The inverse problem of electrocardiography

The inverse procedure consists of two distinct steps: first, the computation of a transfer matrix using a forward model, second, forming an optimization problem to find the unknown cardiac sources from the given thoracic potentials.

There are various regularization techniques available for stabilizing ill-posed problems. These techniques include the Tikhonov regularization [66], statistical constraints [22], the Twomey regularization [69] and rank methods based on singular decomposition techniques [39]. Most of these methods produce similar results or reduce to a similar form under certain conditions [52].

1.2.1 Review of the literature

Model studies on the inverse problem of electrocardiography can be divided into two broad categories. The first category assumes that cardiac electrical activity

can be represented by equivalent cardiac generators. In these studies, the resultant activity of the heart as a whole is represented by a single dipole [33], multiple-dipoles [57], multipole expansion [24], a single moving dipole (*SMD*) [55] or higher-order moving dipoles such as two moving dipole (*TMD*) [19]. The second category, which offers an alternative approach, characterizes cardiac electrical events by the epicardial potential distribution. These model studies include the use of transfer coefficients based on biophysical modeling and statistical analysis. A review of inverse solutions in term of equivalent sources and epicardial potentials is in recent articles by Gulrajani et al. [29, 28] and Rudy and Messinger-Rapport [52].

Equivalent sources. The SMD has been found adequate for the recovery of a single pre-excitation wavefront or an ectopic focus, and can localize the site of origin within 2.5 cm [45]. However, it cannot recover complex activity in the presence of infarcted regions and multiple activation wavefronts [54]. The TMD can be used in cases where two active wavefronts are suspected [29].

Inverse determination of surface isochrones from the body surface potentials is another method studied by Cuppen and van Oosterom [17] using the activation data reported by Durrer et al. [20]. They assumed that the geometry and position relative to the torso surface of the ventricular muscle are known. Their results show that inverse solutions were more sensitive to geometry and conductivity than to normal noise encountered in the body surface potentials [17] and concluded that to obtain a reliable inverse solution, true "tailored" geometry should be used [36].

Epicardial potentials. The idea of using epicardial potentials as surface sources for representing cardiac activity was proposed by Zablow [74]. This has initiated an alternative approach to the inverse problem in terms of epicardial potentials [5]. This approach is interesting for the following reasons [71]: (i)

The uniqueness of the epicardial potentials is mathematically guaranteed. (ii) The recovered epicardial potential distribution can be validated by experimental mesurements. (iii) The inclusion of the source and intracardiac transfer factors is not required which greatly simplifies the modeling aspect of the problem and the validation of results.

In an *in vivo* study, Barr and Spach [6] used an intact canine preparation with approximately 75 epicardial electrodes and developed a transfer matrix using surface integrals. Inverse epicardial potentials were computed from 150 measured body surface potentials, using statistical regularization techniques. Their results show that the general patterns of the epicardial potentials are preserved, with high correlation coefficient in the range of $0.6 - 0.8$, but the detailed features were shifted and the relative error values were 0.7 or more.

In an *in vitro* study, Colli Franzone et al. [15] applied regularization techniques and modeled the inverse problem in terms of control theory and tested their results for a 2-D geometry. Later, Colli Franzone et al. [12] compared the various regularization techniques to recover epicardial potentials from potentials acquired from an isolated canine heart placed in a cylindrical electrolytic tank. In a subsequent study, a canine heart was placed in a realistically shaped human-torso tank and modeled by FEM in 3-D [13]. Colli Franzone et al. [13] performed a comprehensive theoretical study of the inverse problem and investigated the performance of different constraints to determine quasi-optimal regularization using test functions, simulated data and experimental data. They reported results of a high quality in terms of pattern match between the recovered and the measured epicardial maps, and with a relative error less than 0.5 in the QRS and T waves [14]. More recently, Soucy [62] modeled an experimental set up, an isolated dog heart

placed in a cylindrical tank, and compared the Tikhonov zero order regularization method with the Twomey regularization method. These two methods produced similar inverse maps that were smoothed in comparison with the measured maps.

In a simulation study, Yamashita and Takahashi examined the inverse procedure with 2-D [72] and 3-D [73] inhomogeneous realistic geometry. They computed the transfer matrix using FEM and a current source within the cardiac region. While smoothness of the epicardial potentials and minimization of their norm were carried out in the 2-D case, the norm was minimized in 3-D. The inverse potentials compared very well to the simulated epicardial potentials, except in regions having large potential gradients or in regions that were distant from the torso surface.

There have been few reports of an inverse solution applied in humans. In a normal subject, Horáček et al. [32] and Colli Franzone et al. [13] have applied the inverse procedures and compared their results with known activation sequences. In an abnormal subject, Huiskamp [35] has computed the isochrones and compared the results with the activation sequence of the heart removed during the transplant operation. Geometrical mesurements of this heart-transplant patient were made by X-ray pictures for determining the heart orientation. Therefore, the geometrical accuracy in this case is not the same as those obtained using cross-sectional images. In patients with anterior and inferoposterior infarcts, Toyama et al. [68] applied the inverse procedure of Yamashita and Takahashi [73] to recover the infarcted areas on the epicardial map. They compared their results with the infarcted areas detected by the scintigram and reported that this method might be useful for predicting infarcted areas. MacLeod [41] compared inverse epicardial potential maps calculated from BSPMS recorded during the occlusion of a known

coronary artery in patients undergoing percutaneous coronary angioplasty, and found a good match between the calculated epicardial maps corresponding to the ST segment, and the epicardial regions affected by the occlusion.

1.3 Purpose of this study

The main objectives of this thesis are:

(i) *Improving the forward modeling* by constructing a high-resolution geometrical model of the human thorax, using anatomical data measured by CT scan in a patient whose epicardial and body surface potentials are available (i.e., *matched-realistic geometry*), instead of previously used primitive shapes (i.e., *regular geometry*) [43, 64] or standard body cross sections (i.e., *realistic geometry*) [38, 73].

(ii) *Formulation of the inverse problem of electrocardiography* using the control of dimensionality by revising the space of the regularized inverse solution.

(iii) *Assessment of the inverse solution in terms of epicardial potentials in man* by comparing inverse solutions with epicardial potentials measured invasively in the same subject for which the anatomical data was obtained, rather than using simulated data [38, 73] or comparing the calculated epicardial potentials with results from other subjects [13].

(iv) *Studying the role of estimators*, used to determine imposed criteria or constraints, in the optimization process of the inverse solution.

1.4 Thesis outline

In chapter 2, the procedures involved in the modeling of a human thorax using anatomical images are described. The FEM formulations for the three-dimensional field problem with irregular boundary conditions are presented.

In chapter 3, the FEM modeling procedures are first evaluated using a cylindrically shaped volume conductor for which analytical solution is known and then forward simulations with the realistic torso model are presented.

In chapter 4, the methods of solution for the inverse problem of electrocardiography that are used in this thesis are described, and the stability and sensitivity of the solutions are studied.

In chapter 5, the performance criteria applied for the evaluation of the inverse potential maps and the optimization procedures used for regularization are presented, and the inverse results validating the implementation of the inverse procedures are described.

In chapter 6, quantitative assessment of the inverse procedure in man is made, based on the invasively measured epicardial potentials.

Chapter 7 summerizes the main results and presents the conclusions.

Chapter 2

The forward problem: modeling

Forward modeling in electrocardiography involves four basic stages:

(i) representation of the cardiac bioelectric sources as an equivalent generator,

(ii) definition of the volume conductor in terms of geometry and electric properties,

(iii) determination of the relationship between the sources and the body surface potentials, and

(iv) application of a solution method to obtain the field distributions.

This chapter describes the procedures that are used in the development of the geometrical and analysis models of the human thorax, and specifically, in the model formulation using FEM.

2.1 Biophysics of the problem region

The *electromotive forces* (emfs) which arise within the myocardium as a result of the excitation and recovery of the cardiac cells produce electromagnetic field

throughout the thorax. The biophysical factors that influence the potential distribution measured over the body surface are those affecting the cellular source of emfs (*source factor*), the volume conduction in the heart region (*intracardiac transfer factor*) and finally the volume conduction in the tissue between the epicardial and body surfaces (*extracardiac transfer factor*). These factors depend on the spatial distribution of the bioelectric sources and on the geometry and electromagnetic properties of the media.

2.1.1 Structural features

The human thorax comprises highly irregular boundaries, with no translational symmetry or axisymmetric properties. Hence, a three-dimensional model of the problem region is required.

Variations of size, shape and relative position of the heart and thorax can be encountered in different subjects. These variations may be even more pronounced under abnormal conditions (e.g. ventricular hypertrophy). The main consequence of these variations are a change of the area and shape of the contact surfaces between the different inhomogeneous regions. This suggests that realistic geometry matched for a given subject is required for highly accurate field solution.

2.1.2 Material properties

The electrical properties of the tissues in the human thorax can be considered as purely resistive due to negligible inductive and capacitive effects within the body, as a consequence of the low-frequency components of the electrocardiogram. In other words, displacement currents are negligible compared to the conduction currents [51]. Hence, the human thorax can be modeled as a volume conductor

under time-invariant electric field conditions with electrically inhomogeneous media (Table 2.1). Blood is a relatively good conductor (conductivity $\sigma = 0.67 S/m$) at body temperature, while the effective conductivities of the lung and the thorax are about 0.05 and 0.356 S/m, respectively [53].

Table 2.1: Conductivity values used for modeling the human heart and torso.

Tissue	*Conductivity*	
	symbol	*value S/m*
Heart	σ_h	0.233
Lungs	σ_l	0.050
Spinal Region	σ_s	0.182
Thorax	σ_b	0.356

2.2 Construction of the heart-torso model

A three-dimensional finite element torso model has been constructed from serial cross-sectional images of the human body, which were obtained via x-ray computerized tomography (CT) scans. This section describes the steps required to generate this model. The finite-element approach is particularly well suited to this task, because it provides a means to test solutions to problems involving highly irregular, inhomogeneous and anisotropic volume conductors [60, 75]. It is especially useful when the uncertainties due to geometry and/or position may have an influence on the computational analysis (see, e.g., [10]). The method also has the advantage of being able to use readily available serial cross-sectional images obtained from techniques such as nuclear magnetic resonance CT or x-ray CT. FEM uses the notion of structural partitioning, which makes the model easier to manipulate without reducing the size of the structure. In the case of large bound-

ary value problems, with substructuring of the region of interest, formulation and analyzis are greatly facilitated.

The geometrical model has a direct influence on the analysis to be carried out, hence certain factors must be taken into account during modeling. These are [58]:

(a) selection of suitable element types such as tetrahedra, wedges and hexahedra, for the discretization to match the geometric shape;

(b) compatibility of interfaces such as nodes, edges and faces, between subdomains;

(c) local uniform or nonuniform refinement wherever necessary; and,

(d) satisfying the physical laws and appropriate constraints in the problem region.

The procedure we followed to construct the heart-torso model consisted of three phases [58]: (i) data collection and formatting, (ii) construction of topological volumes, and (iii) generation of the FEM analysis model.

Data collection and contour detection. Anatomical data was obtained from a male subject using a Picker 1200 CT scanner. Fourty-three slices were taken from neck to abdomen at $1cm$ intervals (Fig. 2.1). Figure 2.2 shows a typical cross-sectional X-ray CT image; It is apparent that the boundaries of the inner organs are well defined. The boundaries of interest were digitized manually using a HIPAD digitizing tablet. Next, the formatting of the data was carried out using a data linker (running on a Masscomp mini-computer and a micro-VAX computer) to translate and reformat the data for the solid modeller system, PATRAN [21].

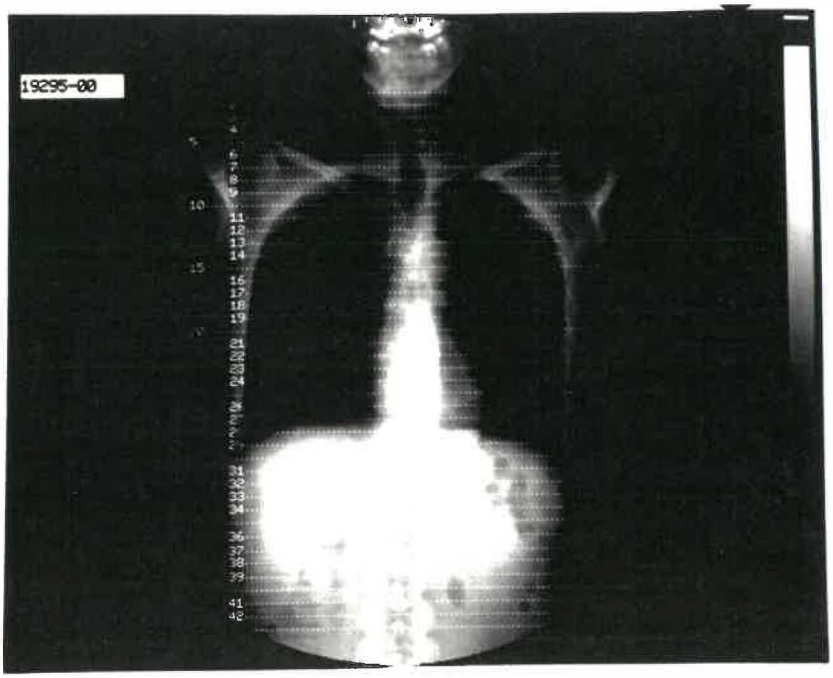

Figure 2.1: X-ray image and the position levels where x-ray CT images were taken from a patient.

Geometrical modeling. Before generating the mesh, the solid structure was built using a parametric mapping approach. The work was carried out on an IRIS 3020 graphics workstation. This required first gross-partitioning of the structure into simpler sub-blocks and then sub-blocks were modeled by approximating its boundary edges by parametric space curves with low-order polynomials, which blended together to form boundary surfaces or patches. Next, two consecutive patches were defined as the top and bottom surfaces of the sub-block, by matching a pair of patches together to form a solid hyperpatch. Finally, the sub-blocks were placed in contact and the topology of the entire structure was defined. The total number of grids, lines, patches and hyperpatches used in geometrical modeling

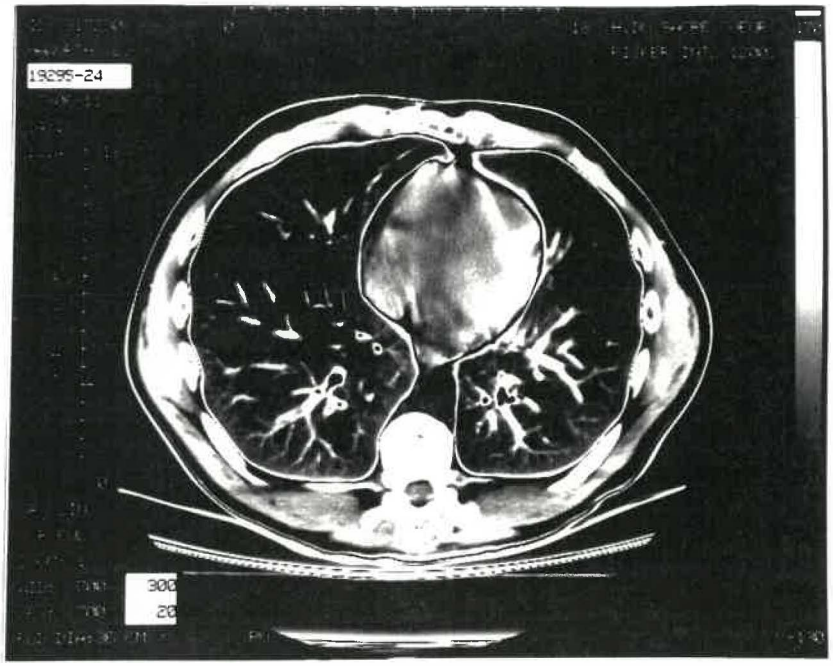

Figure 2.2: Cross-sectional image of the patient shown in Fig. 2.1. The image corresponds to a transverse section through the thorax at the level of $24cm$ below the neck.

phase are given in Table 2.2. Figure 2.3 shows typical segments of the topological volumes taken from the geometrical model at two different levels.

Analysis modeling. In this phase, the irregular and inhomogeneous topological-solids were decomposed into a valid union of finite elements to form the final geometrical model. The steps required were:

Table 2.2: Geometric elements used to form topological volumes for the geometrical model from the anatomical data images.

Grid	*Line*	*Patch*	*Hyperpatch*
16017	1465	1275	1505

(a) Node-point generation within and on the surface of the solid; this process was controlled over the local coordinate system of the hyperpatch.

(b) Element generation to form a mesh of wedge elements, which were then subdivided into tetrahedral elements.

(c) Material property definition, which required assigning conductivity values for the heart, lungs, spinal region and the rest of torso,

(d) Definition of the constraints, i.e., boundary conditions on the interfaces between regions of different conductivity.

(e) Node and element numbering compactions and deletion of duplicate entries,

(f) Visual testing by color coding of the regions of interest.

(g) Node resequencing, using Cuthill-McKee and Gibbs-Pool-Stockmeyer [60, 75] techniques, to optimize the connectivity definitions of all elements, in order to reduce the computation time.

When all segments had been processed, they were reconstituted to form the complete 3-D finite element model. This was not too difficult since there was compatibility between nodes, edges and faces for any two consecutive slices. Two sets of

torso models were developed with different conductivity regions and spatial resolution (Table 2.3). The first set comprised 232 and 872 nodes on the epicardial and body surfaces, respectively; the second set had an improved resolution, with 352 and 1312 nodes on the epicardial and body surfaces. Each set comprised three models with different conductivity regions: homogeneous (T), with lung inhomogeneities (LT), heart and lung inhomogeneities (HLT) and with heart, lung and spine inhomogeneities ($HLST$).

Table 2.3: Eight different human torso models constructed from a single geometrical model having two nodal resolutions (1 and 2) and different conductivity regions: homogeneous (T), with lungs (LT), with heart, lungs, spine (HLST).

Model	*Total*		*Inhom.*	*No. of nodes on*		*B.W.*	
symbol	*element*	*nodes*	*tissue*	*heart*	*torso*	*before*	*after*
T_1	29810	5517	σ_b	232	872	1676	187
LT_1	29810	5517	σ_b,σ_l	232	872	1676	187
HLT_1	29810	5517	$\sigma_b,\sigma_l,\sigma_h$	232	872	1676	187
$HLST_1$	29810	5517	$\sigma_b,\sigma_l,\sigma_h,\sigma_s$	232	872	1676	187
T_2	67045	12084	σ_b	352	1312	3770	384
LT_2	67045	12084	σ_b,σ_l	352	1312	3770	384
HLT_2	67045	12084	$\sigma_b,\sigma_l,\sigma_h$	352	1312	3770	384
$HLST_2$	67045	12084	$\sigma_b,\sigma_l,\sigma_h,\sigma_s$	352	1312	3770	384

These models are easily modifiable with respect to material and geometrical properties. For example, the number of nodes on the epicardial boundary can be changed, or translations of node locations can be performed. Figure 2.4 and 2.5 show segments of the finite element volumes at levels 24 and 29 taken from the $HLST_1$ and $HLST_2$ models, respectively.

The total number of nodes and tetrahedral elements used for the different models are also given in Table 2.3. The matrix bandwidth (B.W.) of the analysis

model before and after optimizing the nodal connectivity (using both Cuthill-McKee and Gibbs-Pool-Stockmeyer techniques) are also presented in Table 2.3. Figure 2.6 shows the T_1 model in volume form cut vertically through inner organs. Figure 2.7 shows the complete $HLST_2$ model in shell form in different views.

The next stage was model formulation for computational analysis. Its objective was to calculate the scalar potential and the electric field distribution generated by bioelectric sources in the extracardiac region.

2.3 Model formulation

2.3.1 The source model

The active sources within the myocardium which give rise to the potentials in the surrounding tissues can be represented by a set of potentials, $\{\phi_{h,i} | i = 1, ...N_h\}$, over the epicardial surface at positions $\psi_{h,i} = \{x_{h,i}, y_{h,i}, z_{h,i}\}$.

2.3.2 Governing equations

Consider the thorax as an irregular volume-conductor region, Ω, with conductivity $\sigma(\psi)$. The distribution of the electric potential (ϕ) in this volume conductor must satisfy the laws governing electromagnetic fields. Under quasi-static conditions, the solution of Maxwell's equation becomes independent of the dielectric properties and is thus governed by the internal conductivity distribution and the external insulating boundary. In this case, the governing potential equation is

$$\nabla.\sigma(\psi)\nabla\phi(\psi) = -I_s(\psi) \quad \forall \quad \psi \in \Omega \tag{2.1}$$

with a prescribed source $I_s(\psi)$. If the media is source free, equation (2.1) reduces to Laplace equation:

$$\nabla.\sigma(\psi)\nabla\phi(\psi) = 0 \qquad \forall \ \psi \in \Omega \tag{2.2}$$

2.3.3 Boundary conditions.

At each interface between different organs, there are discontinuities in the conductivity, but both the potential and the normal component of current density are continuous; hence the boundary condition across each interface is:

$$\sigma' \frac{\partial \phi'}{\partial \vec{n}'_\Gamma} = \sigma'' \frac{\partial \phi''}{\partial \vec{n}''_\Gamma} \qquad on \ \Gamma \tag{2.3}$$

$$\phi' = \phi'' \tag{2.4}$$

where primes and double primes represent the media on opposite sides of boundary Γ, and $\vec{n}$ is the outward normal to the surface. The two specific boundary conditions are: explicitly prescribed potential distribution over the epicardial surface,

$$\phi = \phi_h \qquad on \ \Gamma_h \tag{2.5}$$

and vanishing normal components of current density over the body surface,

$$\frac{\partial \phi}{\partial \vec{n}_{\Gamma_b}} = 0 \qquad on \ \Gamma_b \tag{2.6}$$

2.3.4 Finite-element formulation

The finite element method uses the notion of structural partitioning. Either the variational method or the weighted residual method can be applied to obtain the functional equation for the solution of the differential operator (2.1) [60, 75]. This

section presents a finite element formulation to the forward problem, using the weighted residual approach subject to a general Neumann boundary condition:

$$\sigma(\psi)\frac{\partial\phi}{\partial\vec{n}_{\Gamma_b}} - \phi_q(\psi) = 0 \qquad with\ \ \psi \in \Gamma_b \tag{2.7}$$

and Dirichlet boundary condition (2.5).

Consider a set of arbitrary weighting functions w_n, w_{n_N} and w_{n_D}, and let $\hat{\phi}$ be the approximate potential solution; then the weighted residual for the present boundary value problem yields,

$$R_n = \int_\Omega w_n(\nabla.\sigma\nabla\hat{\phi} + I_s)d\Omega + \int_{\Gamma_b} w_{n_N}(\sigma\frac{\partial\hat{\phi}}{\partial\vec{n}} - \phi_q)dS + \int_{\Gamma_h} w_{n_D}(\hat{\phi} - \phi_h)dS \tag{2.8}$$

which explicitly includes and satisfies the boundary conditions. It is noted that the residual obtained by substitution of the approximation into the differential equation and the residual of the boundary conditions are presented as weighted integrals of such residuals as in Eq. (2.8), for more details, see [75]. N linearly independent equations can be constructed by setting each weighted residual to zero. The operator part of first integral term may be written as,

$$w_n\nabla.(\sigma\nabla\hat{\phi}) = \nabla.(\sigma w_n\nabla\hat{\phi}) - \sigma(\nabla w_n).(\nabla\hat{\phi}). \tag{2.9}$$

Applying the divergence theorem on the first term of right side we get,

$$\int_\Omega \nabla.(\sigma w_n\nabla\hat{\phi})d\Omega = \int_\Gamma w_n\sigma\frac{\partial\hat{\phi}}{\partial\vec{n}}dS, \tag{2.10}$$

where Γ, comprises Γ_h, Γ_l, Γ_s and Γ_b, the surface boundaries for the heart, lung, spine and body, respectively, in the volume Ω. After substitution of equations (2.9) and (2.10), equation (2.8) becomes

$$
\begin{aligned}
R_n = & - \int_\Omega \sigma(\nabla w_n).(\nabla \hat{\phi}) d\Omega + \int_\Omega w_n I_s d\Omega \\
& + \int_{\Gamma_b} (w_n + w_{n_N}) \sigma \frac{\partial \hat{\phi}}{\partial \vec{n}} dS - \int_{\Gamma_b} w_{n_N} \phi_q dS \\
& + \int_{\Gamma_l} w_n \sigma \frac{\partial \hat{\phi}}{\partial \vec{n}} dS + \int_{\Gamma_s} w_n \sigma \frac{\partial \hat{\phi}}{\partial \vec{n}} dS \\
& + \int_{\Gamma_h} w_n \sigma \frac{\partial \hat{\phi}}{\partial \vec{n}} dS + \int_{\Gamma_h} w_{n_D} (\hat{\phi} - \phi_h) dS.
\end{aligned} \tag{2.11}
$$

This is a general formulation for the potential distribution. However, for the present problem, the Neumann boundary condition is considered to be homogeneous (i.e., $\phi_q = 0$ and $\partial\phi/\partial\vec{n} = 0$ on the surface Γ_b). Thus the third and fourth terms on the right side of Eq. (2.11) are cancelled. While the conductivity is allowed to be discontinuous between elements, the normal flux density, $\sigma\partial\hat{\phi}/\partial\vec{n}$, must be continuous on the these boundaries. Therefore, the fifth, sixth and seventh terms on the right side of Eq. (2.11) should cancel when the residuals for adjacent elements are combined, since there exists a common surface, either on Γ_h, Γ_l or Γ_s, between two elements. Neglecting the fifth, sixth and seventh terms in Eq. (2.12) is equivalent to enforcing continuity of the normal flux density, i.e., satisfying Eq. (2.11), and so there is no need to evaluate their residuals. Therefore, Eq. (2.11) becomes

$$
R_n = - \int_\Omega \sigma(\nabla w_n).(\nabla \hat{\phi}) d\Omega + \int_\Omega w_n I_s d\Omega + \int_{\Gamma_h} w_{n_D} (\hat{\phi} - \phi_h) dS. \tag{2.12}
$$

Examining Eq. (2.12), the third term should be cancelled because the boundary surface Γ_h is externally constrained. The Dirichlet condition, Eq. (2.5), holds on the surface Γ_h (i.e., $\hat{\phi} = \phi_h$). Hence the final equation becomes,

$$
R_n = - \int_\Omega \sigma(\nabla w_n).(\nabla \hat{\phi}) d\Omega + \int_\Omega w_n I_s d\Omega \tag{2.13}
$$

which explicitly includes and satisfies the boundary conditions, equations (2.5) and (2.6) [60, 75]. If the Galerkin procedure is applied, then it is required that the weighting function w_n be identical with the basis function, that is,

$$w_n = \alpha_m. \tag{2.14}$$

The region Ω is subdivided into tetrahedral elements. Within each element, the potential $\hat{\phi}$ is approximated by a set of polynomials α_m, complete to order n_o as:

$$\hat{\phi} = \sum_{m=1}^{N} \phi_m \alpha_m(x, y, z) \tag{2.15}$$

where,

$$N = (n_o + 1)(n_o + 2)(n_o + 3)/6 \tag{2.16}$$

and ϕ_m represents the potential values at N interpolation points. For details of the interpolation polynomials, see Appendix A. Substituting equation (2.15) into equation (2.13), the contribution of a typical element in the problem domain yields a set of linear equations,

$$A^e \hat{\phi}_m = C^e \tag{2.17}$$

where,

$$\begin{aligned} C^e &= \int_{\Omega^e} \alpha_m I_s d\Omega \\ A^e &= \sigma \int_{\Omega^e} \nabla\alpha_m . \nabla\alpha_n d\Omega. \end{aligned} \tag{2.18}$$

To evaluate matrix A^e, a coordinate transformation from global to normalized coordinates is required to facilitate the use of the shape functions (2.15) and to obtain the integral formulas for tetrahedral elements (see Appendix B), which have the final form:

$$A_{mn} = \sum_{i=1}^{3} \sum_{j=i+1}^{4} \sigma K_{ij} Q_{mn}^{ij} \tag{2.19}$$

$$K_{ij} = \frac{b_i b_j + c_i c_j + d_i d_j}{36V} \tag{2.20}$$

$$Q^{ij}_{mn} = -6 \int_{\Omega_e} (\frac{\partial \alpha_m}{\partial \psi_i} - \frac{\partial \alpha_m}{\partial \psi_j})(\frac{\partial \alpha_n}{\partial \psi_i} - \frac{\partial \alpha_n}{\partial \psi_j}) d\psi_1 d\psi_2 d\psi_3 \tag{2.21}$$

$$C_m = 6V \int \alpha_m I_s \; d\psi_1 \; d\psi_2 \; d\psi_3. \tag{2.22}$$

$$\begin{aligned} m, n &\equiv 1, 2, ..., N \quad (tetrahedron \;\; node \;\; numbering) \\ i, j &\equiv 1, 2, 3, 4 \quad (tetrahedron \;\; vertex \;\; numbering). \end{aligned} \tag{2.23}$$

Computing equation (2.17) involves matrix Q, which is independent of the tetrahedron geometry, and matrix Q^{ij}_{mn} which is a numerical array that will be calculated once for a given order of shape function. Matrix K must be computed for each element with respect to the cartesian coordinates of the tetrahedron vertices, but it involves no numerical integration. K_{ij} is a numerical array which includes information about geometrical shape, size and position of the tetrahedral element in the problem region with respect to the global coordinate system.

2.3.5 Global transfer matrix

Since each problem region is subdivided into finite element volumes, the total energy contributed by all elements in the entire model is the sum of the energies in the individual elements,

$$W = \sum_{all} W^e. \tag{2.24}$$

Using a standard elemental assembly procedure yields a set of linear equations with inforced boundary constraints of the final form,

$$A\hat{\phi} = C. \tag{2.25}$$

Matrix A is a symmetric, sparse and positive definite for the present boundary value problem with the given weighting function. It is sometimes called the global

matrix, $\hat{\phi}$ represents a vector of nodal potentials to be determined and C is column vector associated with the prescribed sources.

2.4 Model construction and field computation

The general approach for geometrical modeling and computational analysis is shown in Fig. 2.8. It consists of [59]: (i) geometrical image preparation and pre-processing; (ii) construction of the volume conductor and definition of the active sources; (iii) problem definition and solution of the model equations; (iv) post-processing and representation of the isopotential and isofield maps.

The FEM software system, MagNet3D [16], running on SUN 3/260 was used for computational analysis. It requires the geometric data base as its input and the output of this solver includes the three vector components of the electric field intensity and the scalar potential at each node of the finite element mesh. The geometric data base includes boundary conditions on the irregular surfaces, sources within the domain or on the boundary surface of the volume conductor and the definition of material properties in any region in the body. It contains all this data without reference to the real values of the material properties and without specifying the excitations or boundary constraints applicable to a particular case. It uses abstract labels avoiding any specific problem-dependent information. The specific attributes of the material properties, excitations and boundary constraints are introduced during computational analysis.

The analysis cycle comprises two interface programs, namely the analysis-translator and the result-translator. The interface programs convert PATRAN neutral files to MagNet3D data files, and *vice versa*, permitting the import and export of the data between the two systems.

Figure 2.3: The topological volumes constructed from two consecutive cross- sectional images at (top) z= 24 and 25, (bottom) z= 29 and 30. The global coordinate system is shown in the lower left corner.

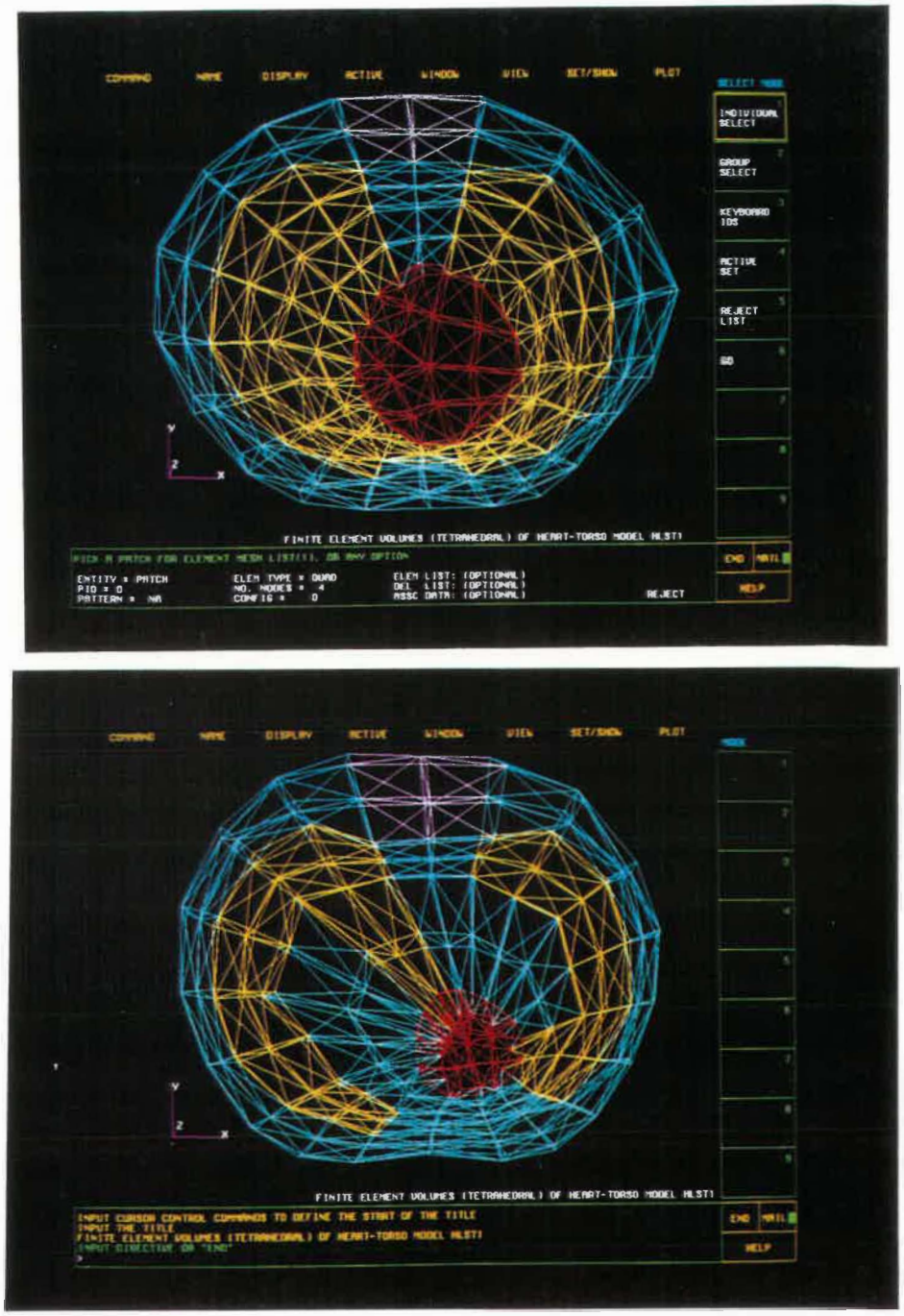

Figure 2.4: The finite element volumes for $HLST_1$ constructed using the topological volumes of Fig. 2.3.

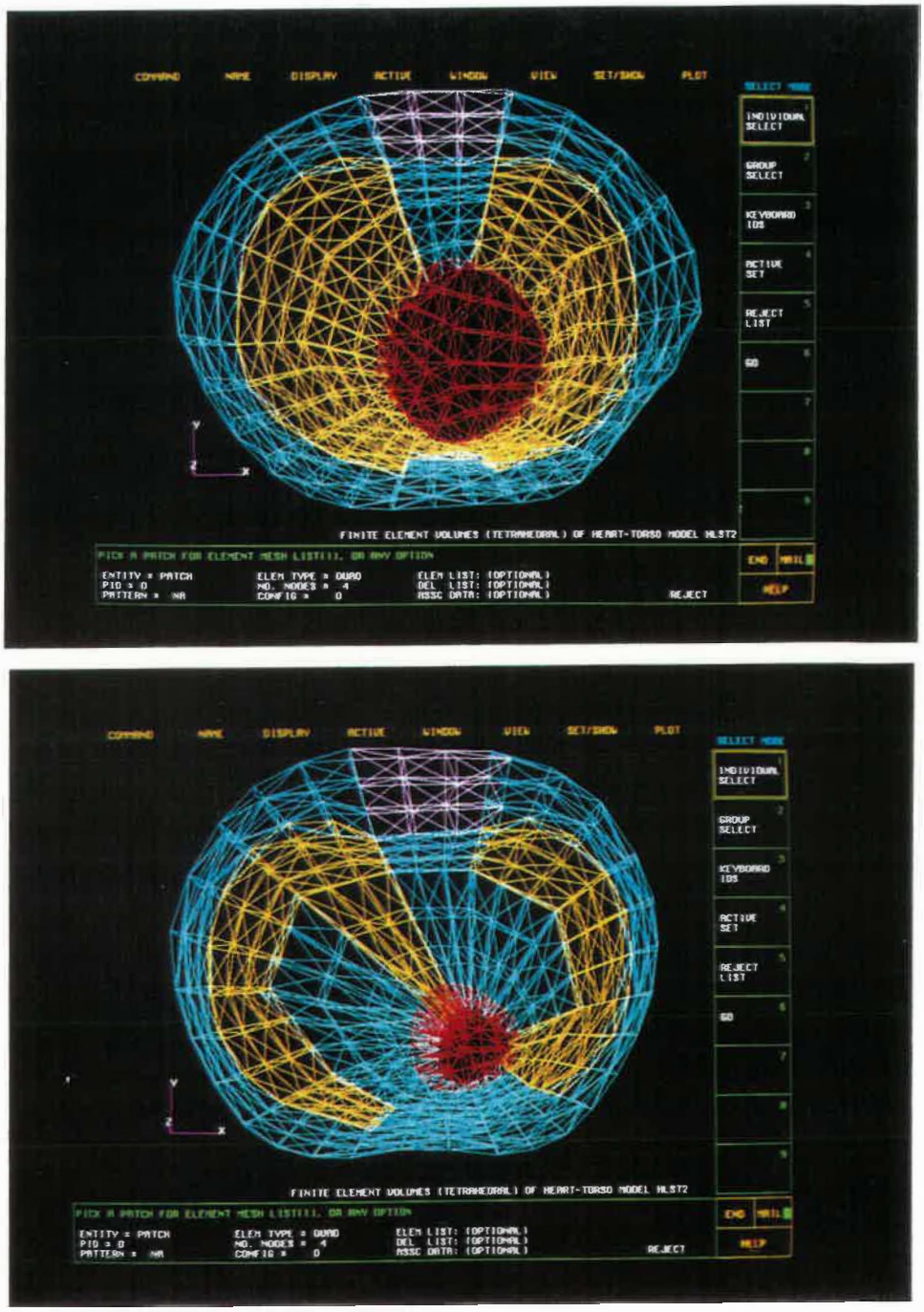

Figure 2.5: The finite element volumes for $HLST_2$ constructed using the topological volumes of Fig. 2.3.

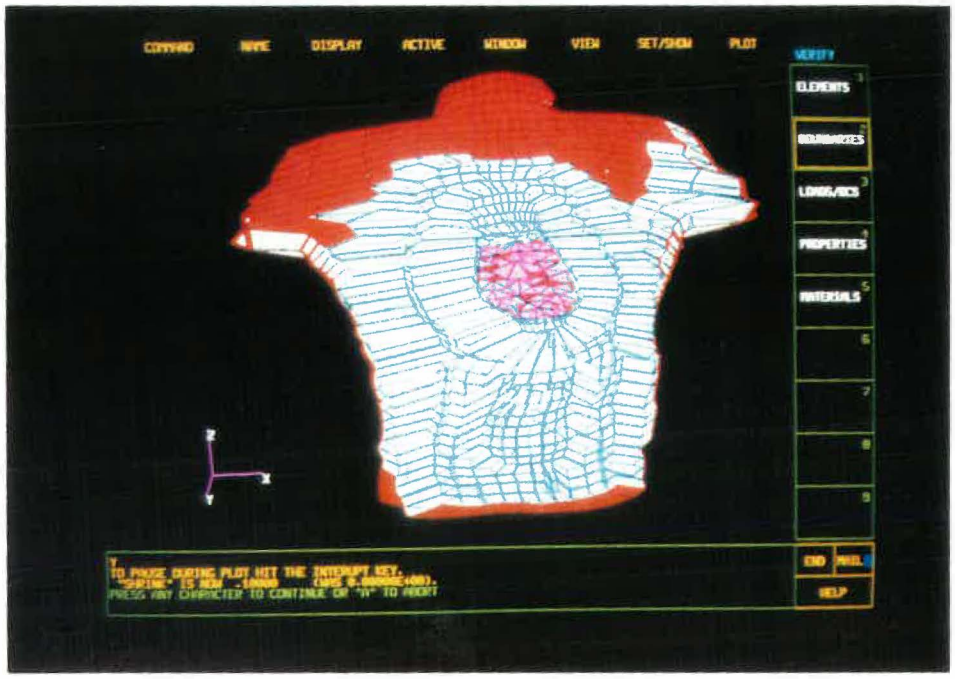

Figure 2.6: Cross-section of the thorax T_1 model cut vertically. The external and internal surfaces are represented in orange and white, respectively.

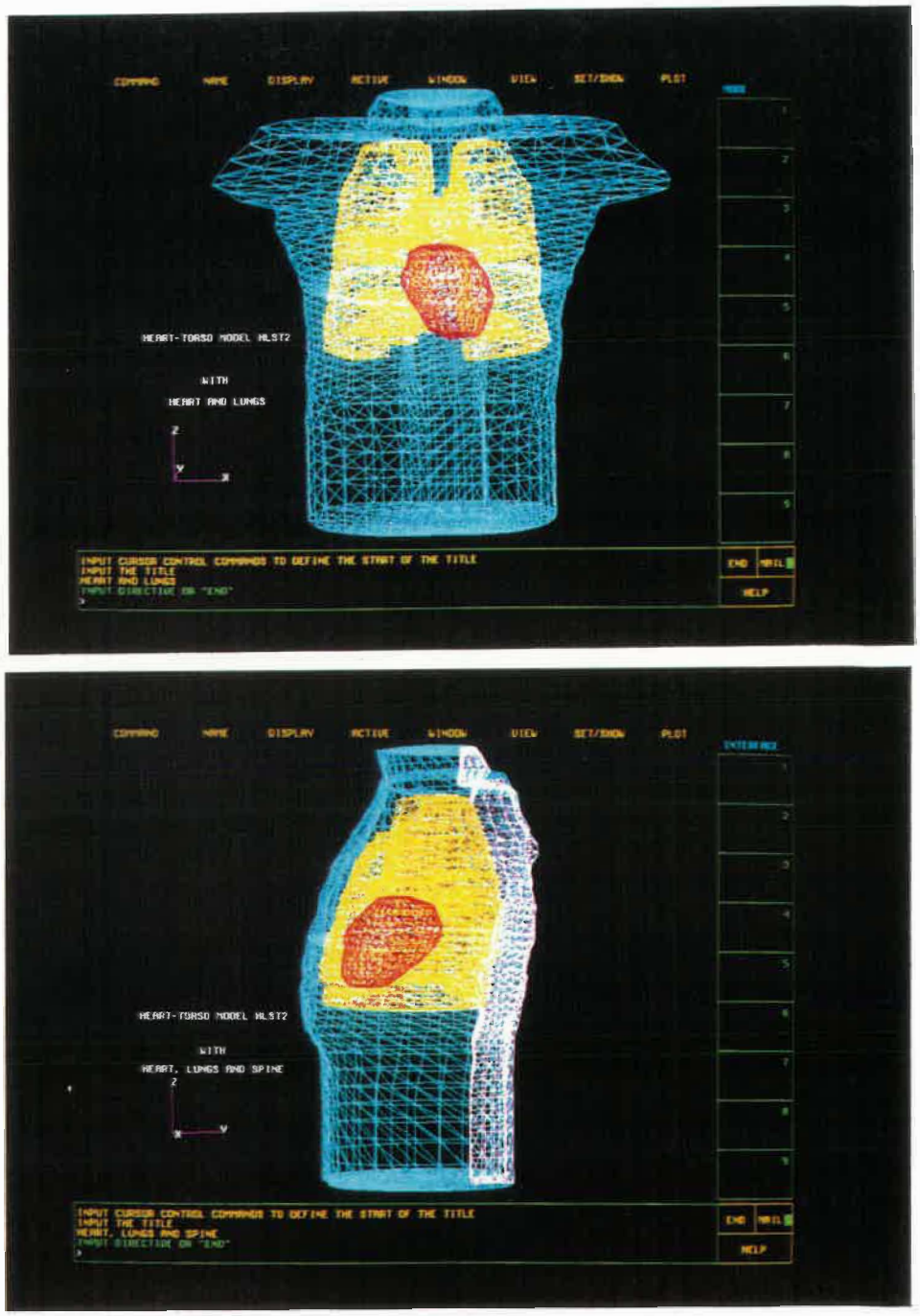

Figure 2.7: Three views of the thorax model $HLST_2$. In (top) frontal view of the model of a WPW patient, with heart and lungs; the spinal region is not shown for clarity. In (bottom) left lateral view. (Continued)

Figure 2.7: (Continued) The model is seen from above.

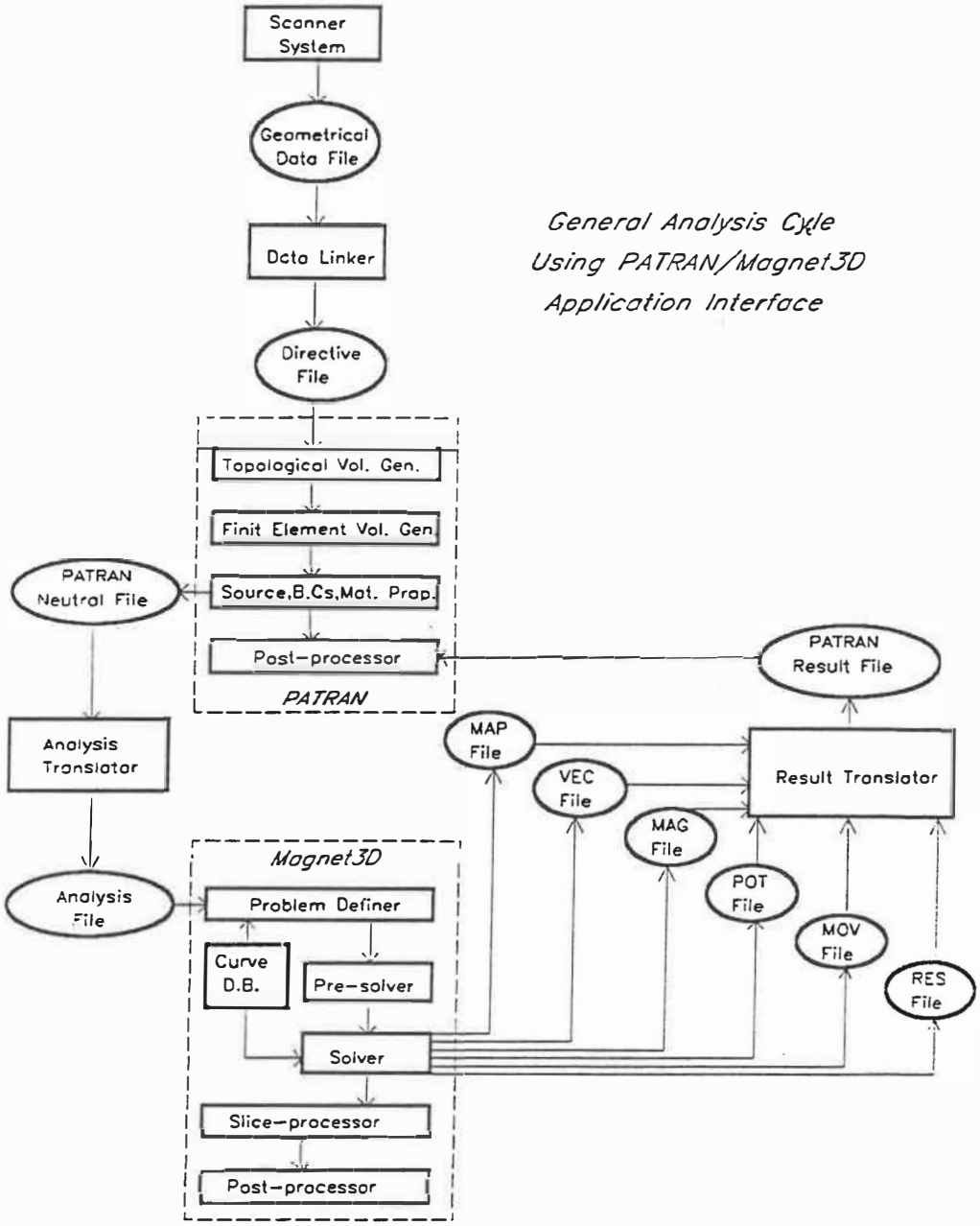

Figure 2.8: The data processing flow for the 3-D modeling and analysis, using a CT scanner, PATRAN and MagNet3D application interfaces.

Chapter 3

The forward problem: validation and field solutions

A cylindrically shaped volume conductor was used as a simple model of the thorax. Since an analytical solution for this primitive shape exists, it allowed us to assess the accuracy and convergence of the FEM solution applied to the heart-torso model.

This chapter presents the results obtained for the evaluation and validation of the forward problem. The simulation results are presented as isopotential and isofield maps on the surface of the body and in cross-sections of the model.

3.1 Model validation

Model validation is considered an essential step in modeling. It enables us to assess the methodology (e.g. to test the interface programs) and to evaluate the accuracy of the solutions. Here, a numerical experiment was performed in which the FEM technique was applied to a geometry for which there exists a known analytic solution. In cases such as ours, where severe limitations are imposed by experiment (e.g. *in situ* measurements in human subjects), and by the technical complexities

(e.g. accurate boundary and conductivity matching between the subject and the model), this numerical experiment was an ideal method of validation.

3.1.1 Solid cylinder with a prescribed source

Analytical solution. Consider a cylinder of height $a = 40\ cm$ and radius $b = 15\ cm$. The potential distribution resulting from a dipole moment in the cylinder must satisfy Laplace's equation and the boundary condition of vanishing normal component of the derivative at the outer surface. For a dipole located on the axis of the cylinder (i.e. $\rho' = 0$), the potential on the outer surface is (Appendix C),

$$\phi_z = \frac{-p_z}{ab\pi\sigma} \sum_{n=0}^{\infty} (2 - \delta_n^0) \frac{cos(\frac{n\pi z}{a}) sin(\frac{n\pi z'}{a})}{I_1(\frac{n\pi b}{a})}, \tag{3.1}$$

where p_z is the dipole moment centered at $z' = 24\ cm$, σ is the conductivity of the medium, I_1 is a modified Bessel function and δ_n^0 is the Kronecker delta (see for example, Okada [49]).

Finite element solution. The human thorax is modeled as a cylindrical volume conductor of height 40 cm and radius 15 cm (Fig. 3.1) with two potential patch sources centered at $z = 24\ cm$ in the direction of the cylinder axis and solved using the FEM analysis described in Fig. 2.8.

Fig. 3.2 shows the calculated isopotential contours on the surface of the cylinder. This result was obtained with a fine mesh model comprising 1358 nodes. The calculated potentials are zero in the transverse plane through $z = 24\ cm$. This is the level of the center of the prescribed source. Fig. 3.3 shows computed potential distribution within the cylinder on the $x - z$ plane. The results shown in this figure demonstrate how the field solution changes as the model mesh is refined from coarse to fine as described in the following section.

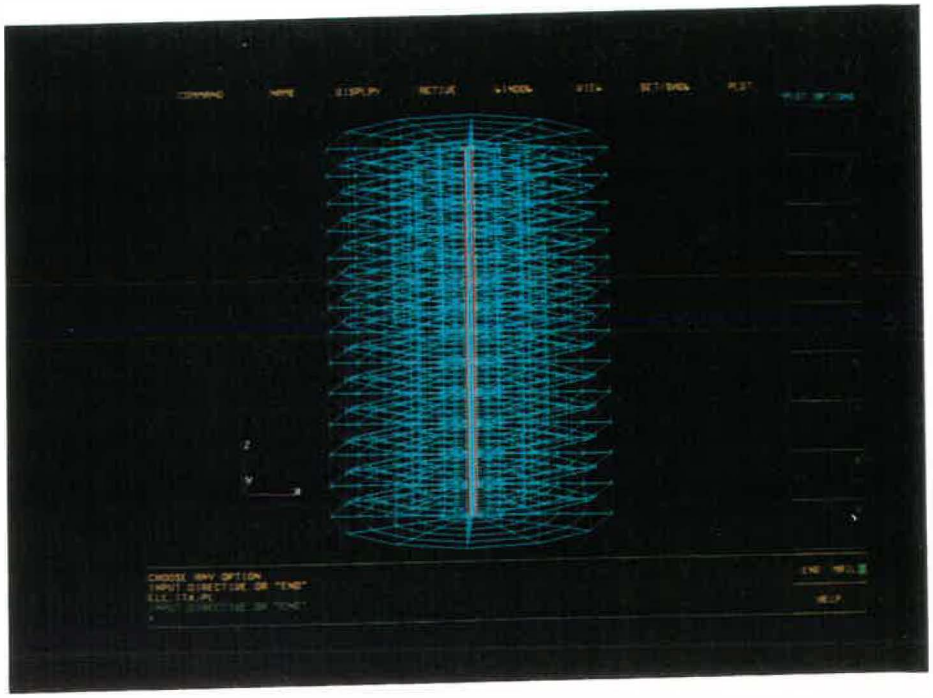

Figure 3.1: A cylindrically shaped volume conductor, modeled by FEM for validation purposes. This is the fine mesh model.

3.1.2 Model convergence

The FEM solution used here is based on a discretization of a continuum problem. This discretization limits the degree of freedom of the system and hence, may prevent reaching the true minimum energy. How close the computed solution is to the exact solution and whether or not it converges to the exact solution are both important questions. In practice, model convergence is the ever closer solution of successive computations to the limiting solution as some computational parameter, such as mesh size, is refined. This parameter is considered to be important and consequently, a systematic analysis of its influence is necessary. The following

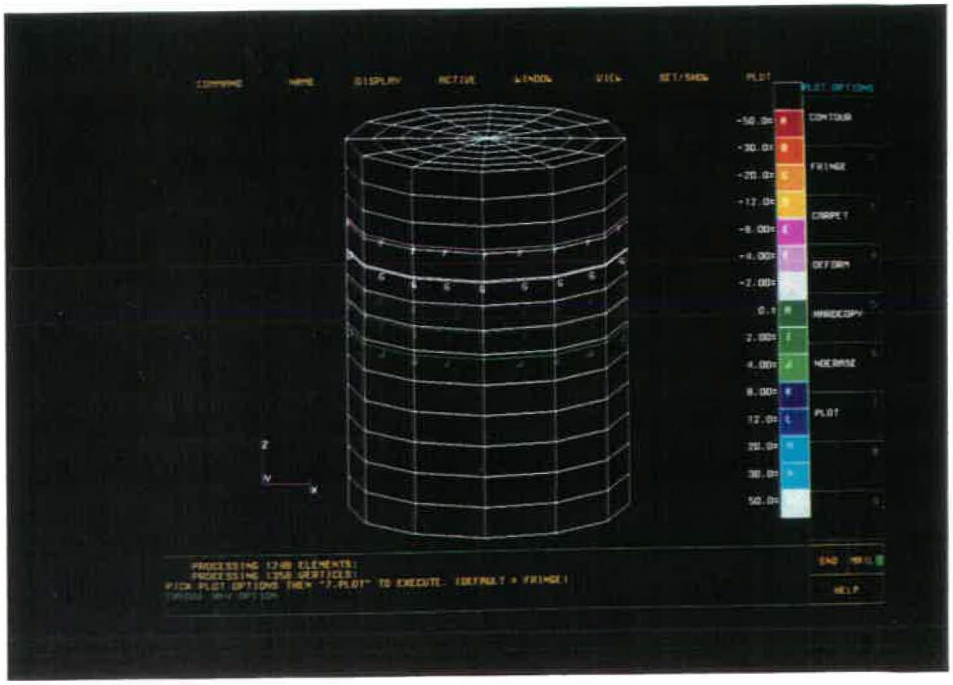

Figure 3.2: Contours of potentials on the outer surface of the cylinder calculated by FEM.

approach was chosen to assess the convergence of the solution:

i) start from an initial coarse mesh and compute the solution;

ii) perform non-uniform mesh refinement of the volume;

iii) compute the solution after every mesh refinement;

iv) examine the residual and the direction of convergence and accept the level found from the discretization having the minimum residual.

Unlike the uniform mesh which starts with a uniform division of edges, the localized fine mesh division was chosen in accordance with external criteria (see

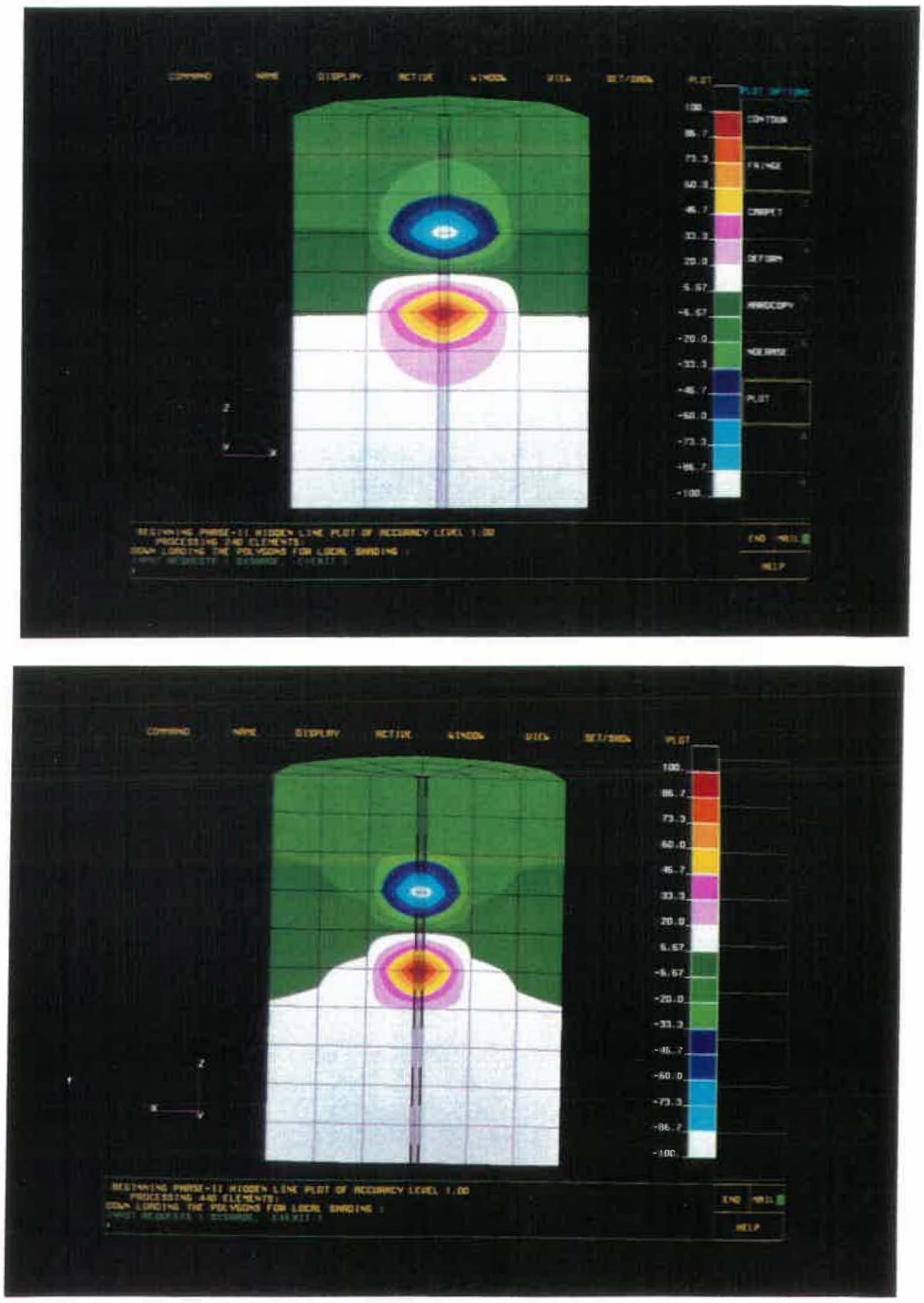

Figure 3.3: Computed isopotential fringes for a cylindrically shaped body on the vertical cross-sections parallel to the $x - z$ plane for: (top) coarse (363 nodes), (bottom) medium (803 nodes) models. (Continued)

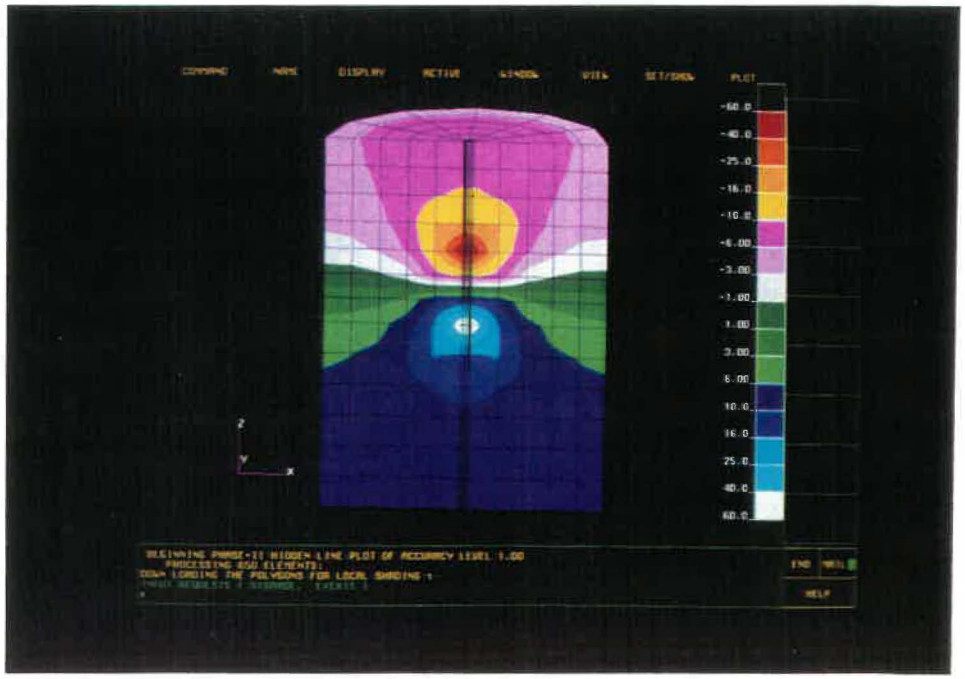

Figure 3.3: (Continued) Fine (1358 nodes) model.

below). The coarse model had 363 nodes (320 elements), the medium model had 803 nodes (720 elements) and the fine model had 1358 nodes (1248 elements). Figure 3.4 compares the analytical solution for the potentials calculated on the surface of the cylinder with the FEM solution using the fine mesh. It is clear that the FEM results are similar to the analytical solution.

The convergence results are plotted in Fig. 3.5 for the three different meshes. These results and the comparison with the analytical solution, indicate that the fine mesh provides an acceptable potential distribution over the entire domain. There is a close match at the center (i.e. at $z = 24\ cm$). The solutions are symmetric about this center and converge toward a constant level.

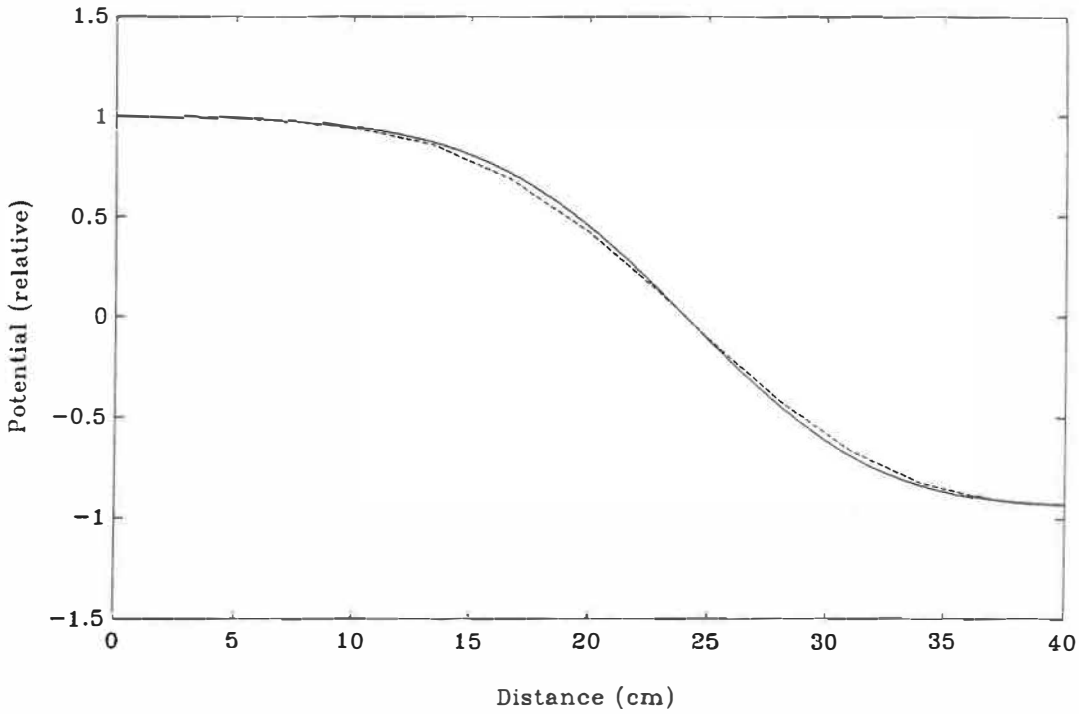

Figure 3.4: Computed body surface potentials for the cylindrically shaped model. Symbols: (–) analytical, (- -) FEM.

Concerning model convergence, a sequence of approximate solutions is obtained as the element size is successively reduced. The sequence is guaranteed to converge to the exact solution as long as certain criteria are met. The one basic rule of mesh planning is to use a fine mesh where the field gradient is expected to be high, and a coarser mesh where the field gradient is expected to be low. In the present work, non-uniform refinement was used. It is an efficient mesh grading and it involves finer subdivisions of the elements in regions where higher accuracy is needed, so as to optimally improve the accuracy of the solution without unnecessarily increasing the cost of computation (i.e., we need to refine the mesh only where the error is highest).

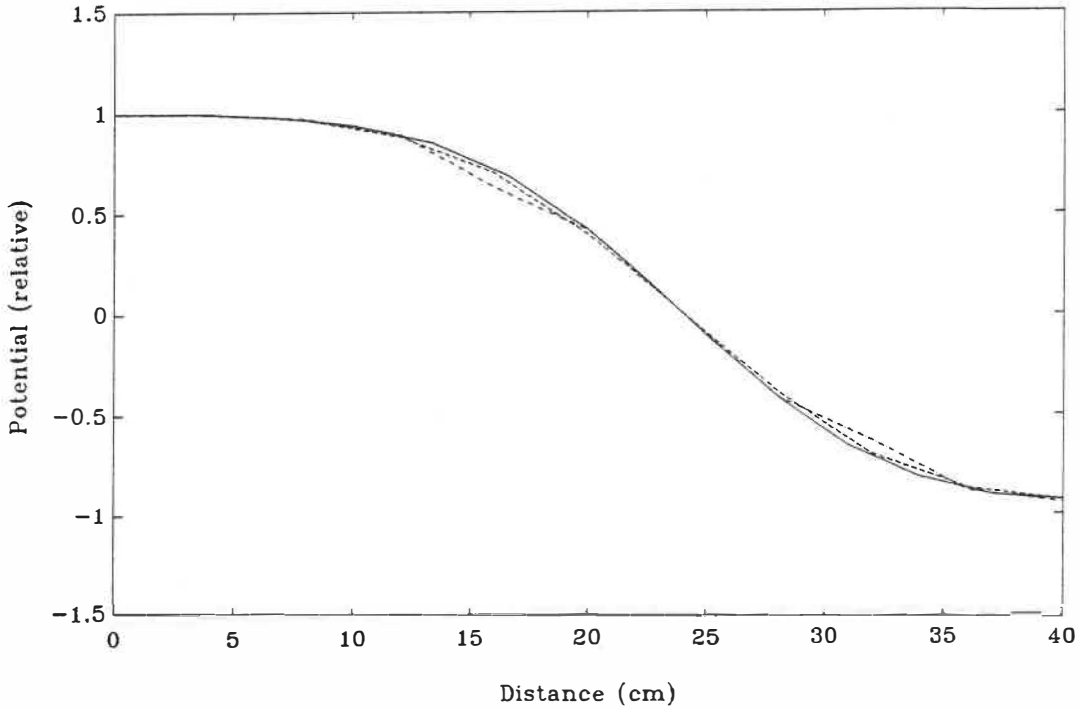

Figure 3.5: Convergence of the FEM solutions for different mesh resolutions. Symbols: (—) fine, (- -) medium and (- . -) coarse models.

Adaptive algorithms for mesh refinement require local refinement criteria which calculate bounds for the difference between the exact and the calculated solution. The error estimate in the FEM solution for electrical potential problems with linear elements is given by

$$\| \hat{\phi} - \phi \| \leq c\, h^2 \, \| \phi \|_H \tag{3.2}$$

where $\| \, . \, \|$ is the L_2 norm $([\int_\Omega (\hat{\phi} - \phi)^2 d\Omega]^{1/2})$, $\| \, . \, \|_H$ is the H_2 norm $([\int_\Omega (\phi^2 + \phi_{,x}^2 + \phi_{,y}^2 + \phi_{,xx}^2 + \phi_{,xy}^2 + \phi_{,yy}^2) d\Omega]^{1/2})$, h is mesh spacing and c is a constant (see for example Hughes [34]). In practice, employing refinement criteria representing element-

by-element errors is an expensive task, due to computation time and memory requirements, and it is difficult to apply regarding the error estimation, $\| \hat{\phi} - \phi \|$. Further, to achieve monotonic convergence, the elements must be complete[1] and compatible[2], that is, the accuracy of the solution increases continuously as the mesh grading increases. Here, all the elements used in the analysis models are complete upto first degree, and they are compatible. Using higher order elements will provide another convergence test (p convergence) where elements have fixed form, but the degree of the polynomial (p) is successively increased. The p convergence test was not made here, since MagNet3d cannot handle the higher order elements at present time.

3.2 The field solution of the human heart-torso model

This section presents the field solutions obtained for the human heart-torso model (chapter 2).

3.2.1 Potential distributions

Two series of numerical experiments were performed. In the first, a model with 5517 nodes was used with three different conductivity distributions. The conductivities are given in Table 2.1. In the second series, calculations were carried out using a higher mesh resolution again with three different conductivity distributions. The heart region and the volume which extends from the epicardial

[1]Completeness means that a constant value of mth derivative (if mth derivative occurs in the functional integral) be attainable in the element domain as the element size tends toward zero.

[2]Compatibility means that the functions within the elements and across the element boundaries must be continuous and it assures that no gaps occur between elements.

surface to the torso surface have different conductivities; the region surrounding the body surface is considered to be non-conductive air. The geometrical structure of the inhomogeneous conductivity regions was kept the same. Potential sources on the epicardium produce an excitation field. Figure 3.6 illustrates the location of the excitation fields defined as a patch source on the epicardium, two sources are located anteriorly near the base (L_1 and L_2), two other sources are located posteriorly (L_3 and L_4) near the base and one source is located at the apex (L_5). The strength of the source on the heart surface was set at one mv with respect to all the other node points on the epicardium. Fig. 3.6 also shows the polar format that will later be used to represent the epicardial isopotential maps. The forward simulations were then tackled with the FEM computational procedure described in section 3.1, [59].

A survey of the experiments is summarized in Table 3.1. These numerical experiments can be divided into three cases.

Let us consider the first case (experiments 1-3). Here, the mesh resolution of the volume conductor was fixed at 5517 nodes and the excitation was located at L_1, but the conductivity values of the inhomogeneous regions were varied. In experiment 1, the thorax was defined as homogeneous while in experiment 2, lung inhomogeneities were added and in experiment 3, the complete inhomogeneous volume conductor was used. Plots of resulting solutions for this set of forward simulations are shown in Figs. 3.7, 3.8 and 3.9. These plots show the calculated isopotential maps in fringe form on the surface of the body in the frontal view (top plot) and posterior view (bottom plot).

The effects of inhomogeneities on the computed body surface maps presented here are related to the activation in which a potential is imposed on individual

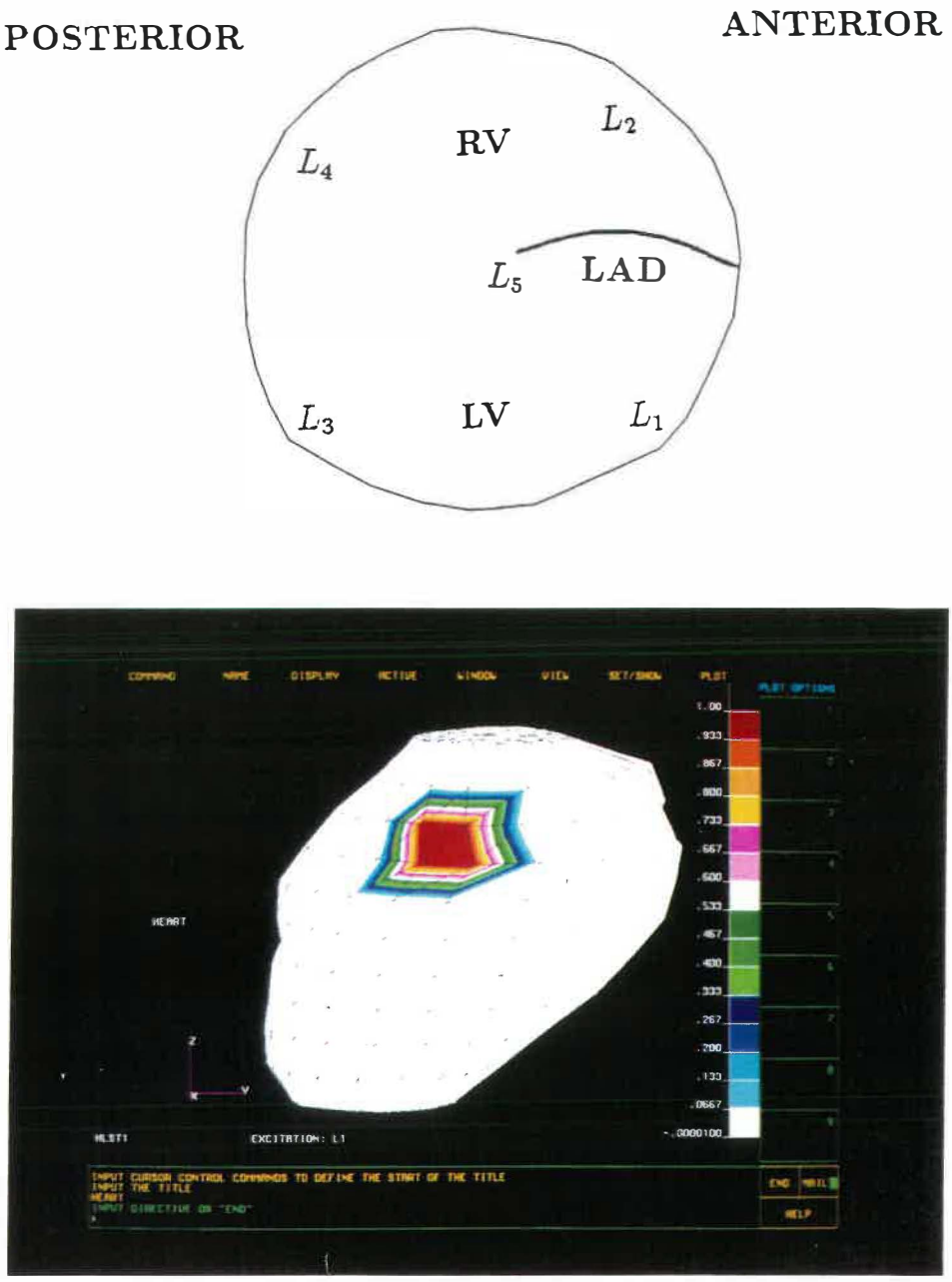

Figure 3.6: Top: anterior view of the front of the heart cut at the base level, displaying the different activation locations over the heart surface at L_1, L_2, L_3, L_4 or L_5. LV: left ventricle, RV: right ventricle, LAD: left anterior descending artery. Bottom: Side view of the heart depicting the the excitation L_1.

Table 3.1: Specifications of the forward simulations. Column 1 indicates an experiment number; columns 2 and 3 show the torso configuration and the conductivities; column 4 gives the mesh resolution; column 5 specifies the location of the initial excitation patch over the epicardium; and column 6 gives the corresponding figure number. The different locations, L_1, L_2, L_3, L_4 or L_5 are shown in Figure 3.6.

Exp. No.	*Model*	*Conductivities*	*Nodes*	*Excitation*	*Figure*
1	T_1	σ_b	5517	L_1	3.7
2	LT_1	σ_b, σ_l	5517	L_1	3.8
3	$HLST_1$	$\sigma_b, \sigma_h, \sigma_l, \sigma_s$	5517	L_1	3.9
4	$HLST_1$	$\sigma_b, \sigma_h, \sigma_l, \sigma_s$	5517	L_2	3.10
5	$HLST_1$	$\sigma_b, \sigma_h, \sigma_l, \sigma_s$	5517	L_3	3.11
6	$HLST_1$	$\sigma_b, \sigma_h, \sigma_l, \sigma_s$	5517	L_4	3.12
7	$HLST_1$	$\sigma_b, \sigma_h, \sigma_l, \sigma_s$	5517	L_5	3.13
8	T_2	σ_b	12084	L_1	3.14
9	LT_2	σ_b, σ_l	12084	L_1	3.15
10	$HLST_2$	$\sigma_b, \sigma_h, \sigma_l, \sigma_s$	12084	L_1	3.16

heart surface elements. The inclusion of the inner inhomogeneities alters the body surface potential distribution, it changes the maximum and the minimum values, it changes also the location of the zero line but does not substantially modify the pattern of potential distributions. The greatest detected effect is due to the addition of the lungs. The spinal region inhomogeneity produces only minor changes.

Now, consider case 2 (experiments 3-7). Here, the effects of the location of the excitation on the potential distribution for the volume conductor with 5517 nodes is investigated. As can be seen in Table 3.1, the complete inhomogeneous volume conductor was used with the same mesh resolution ($HLST_1$). The source element was placed consecutively at 5 different sites ($L_1 - L_5$). Four of them were located near the base of the heart and the fifth source was positioned on the apex. The

results of experiments 3-7 are plotted in Figs. 3.9-3.13, respectively.

The locations of the epicardial sources appear to be projected into the torso surface as potential maxima. The anterior sites L_1 and L_2 produce maxima on the anterior side of torso, the posterior sites L_3 and L_4 produce maxima on the back, and apical site L_5 produces a maximum just under the precordial region. Overall, these thoracic potential distributions do not show any gross errors and they are consistent with the site of the sources.

Finally, the third case involves experiments 8-10. These experiments were set up in order to gain information about the influence of the mesh resolution on the field solution. The influence of the discretization level on the potential distribution at different levels of inhomogeneity can be seen by comparing these experiments (8-10) with their counterpart experiments (1-3). The results of experiments 8-10 are plotted in Figs. 3.14-3.16, respectively. Note that the color coding of the isopotential fringes is different in the two cases.

Increasing the level of mesh resolution from 5517 to 12084 nodes did not change noticeably the shape or the amplitude of the body surface potential maps; rather, it generally smoothed the isopotential contours.

Although the solutions shown in this section are presented on the surface, they are accessible within the volume conductor. Displaying the field distributions is also possible on any organ defined in these models. Fig. 3.17 shows typical computed isopotential contours on the heart and lungs surfaces. Multiple excitations are also possible at any region within the model, inside or outside the heart (Fig. 3.18). These features of the post-processing allow modeling flexibility that is very useful for field studies of inhomogeneous regions with irregular geometry.

Finally, results of forward simulations using measured epicardial potentials

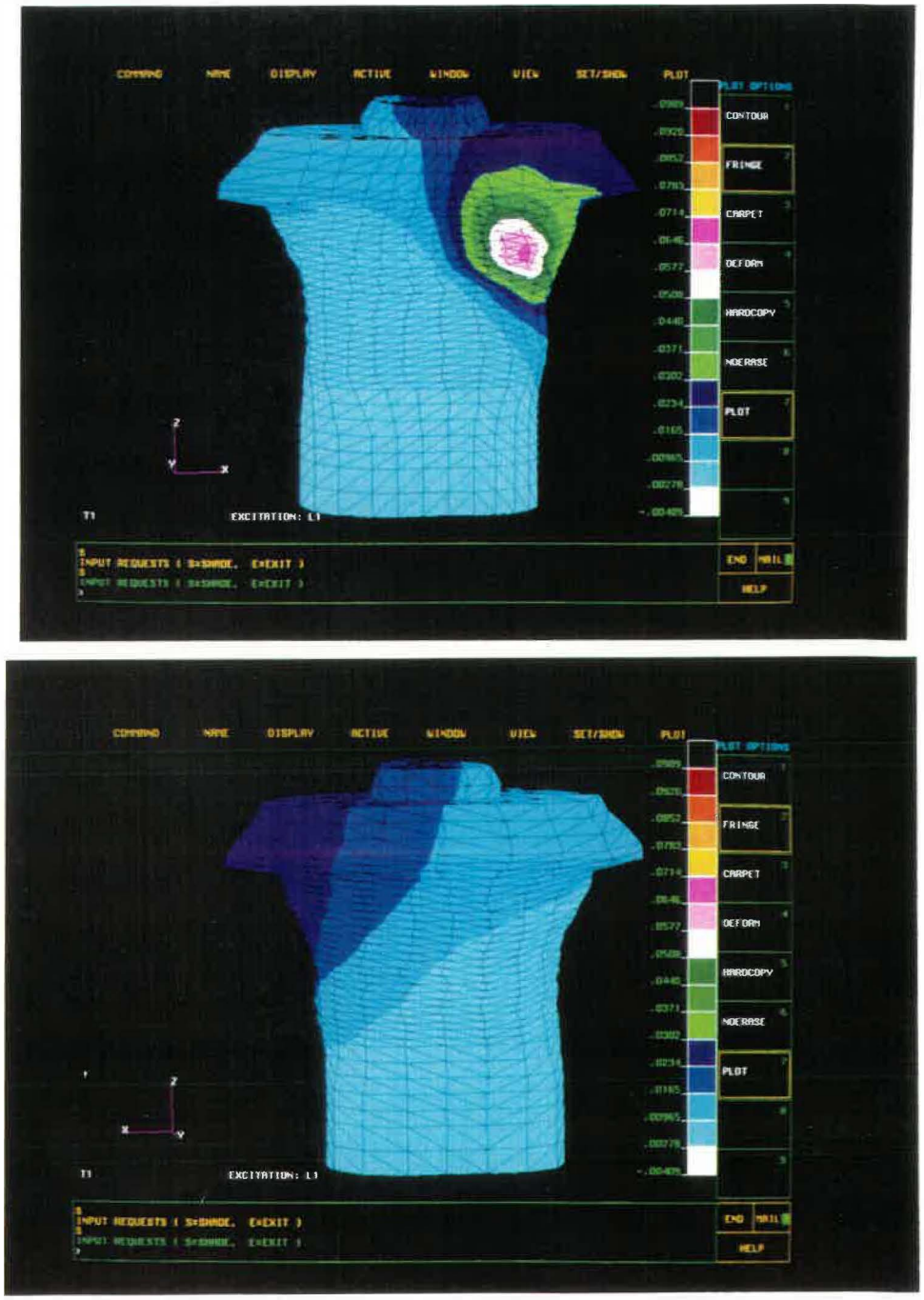

Figure 3.7: Computed body surface fringe maps on (top) anterior view and (bottom) posterior view. These were obtained using the T_1 model with the activation of the heart surface at location L_1.

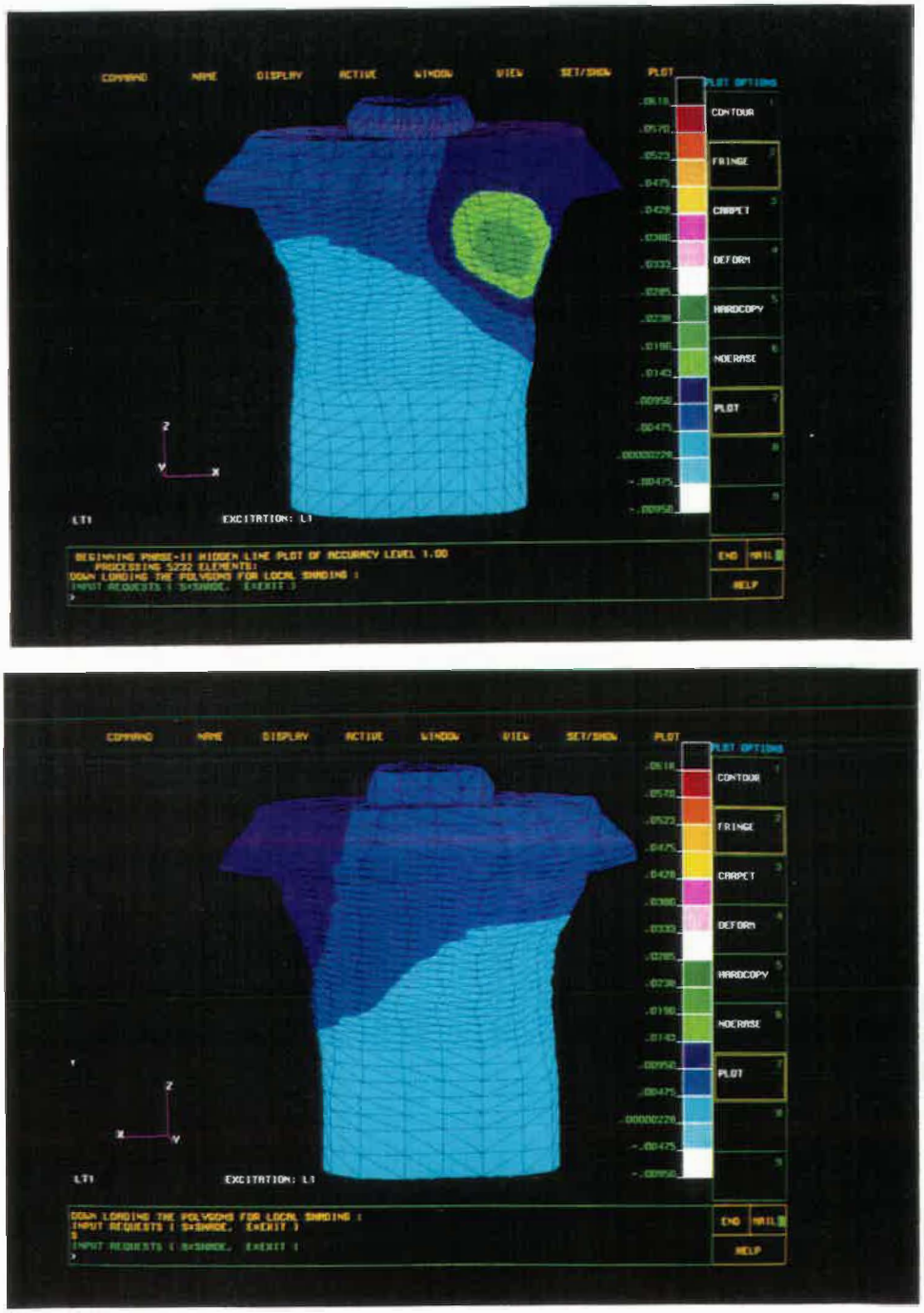

Figure 3.8: Computed body surface fringe maps as in Figure 3.7 for the LT_1 model and the activation at location L_1.

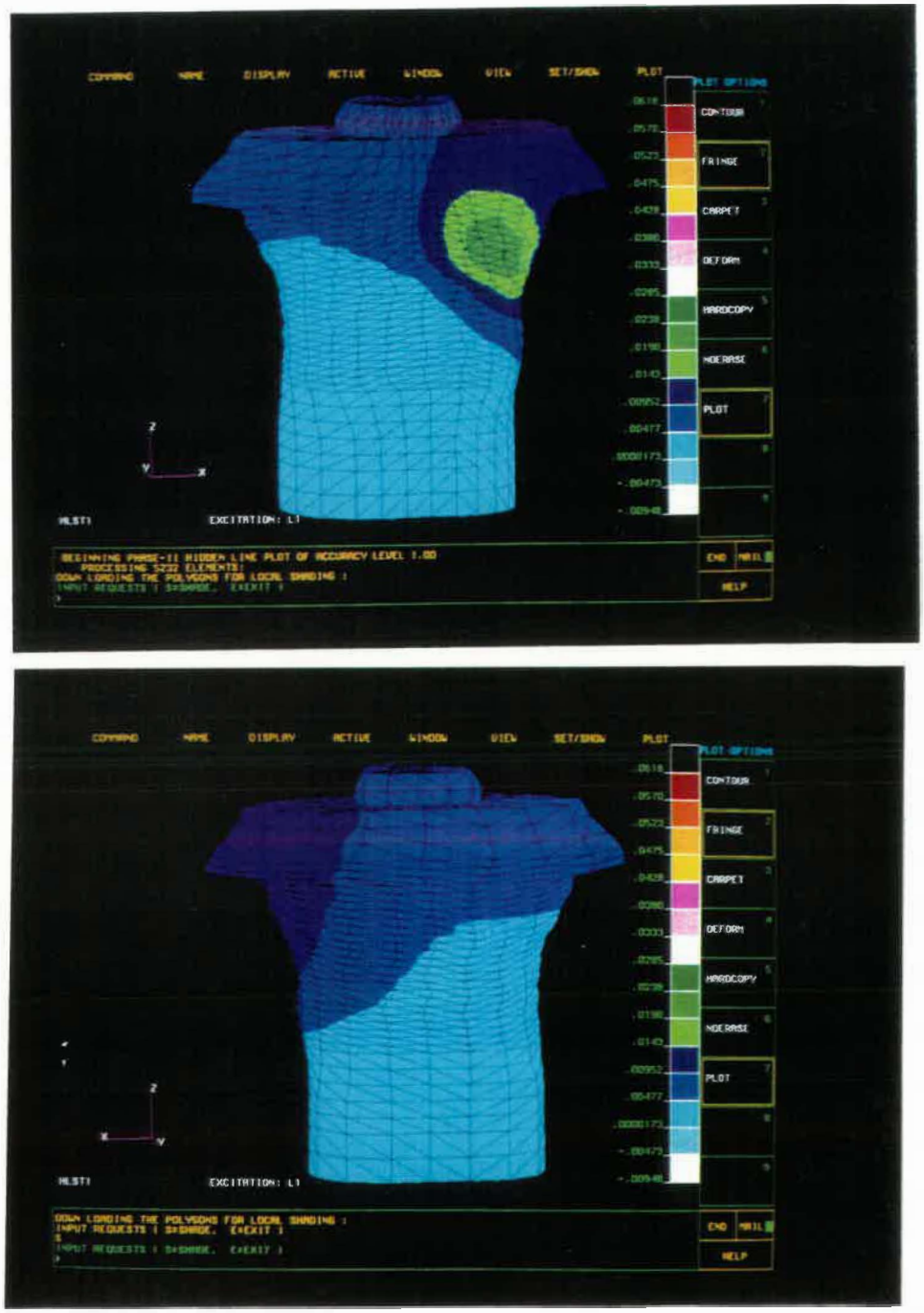

Figure 3.9: Computed body surface fringe maps as in Figure 3.7 for the $HLST_1$ model and the activation at location L_1.

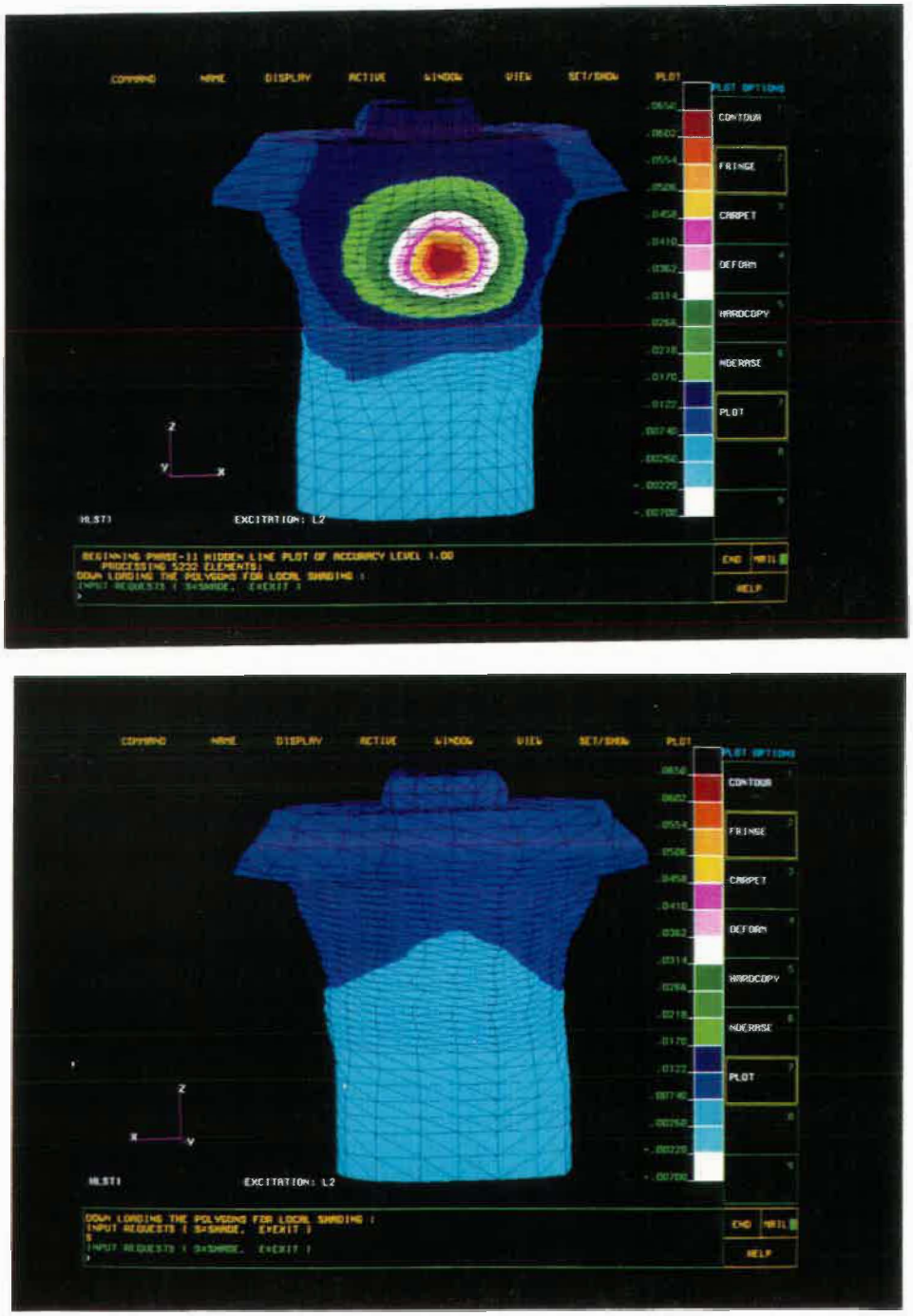

Figure 3.10: Computed body surface fringe maps as in Figure 3.7 for the $HLST_1$ model the activation at location L_2.

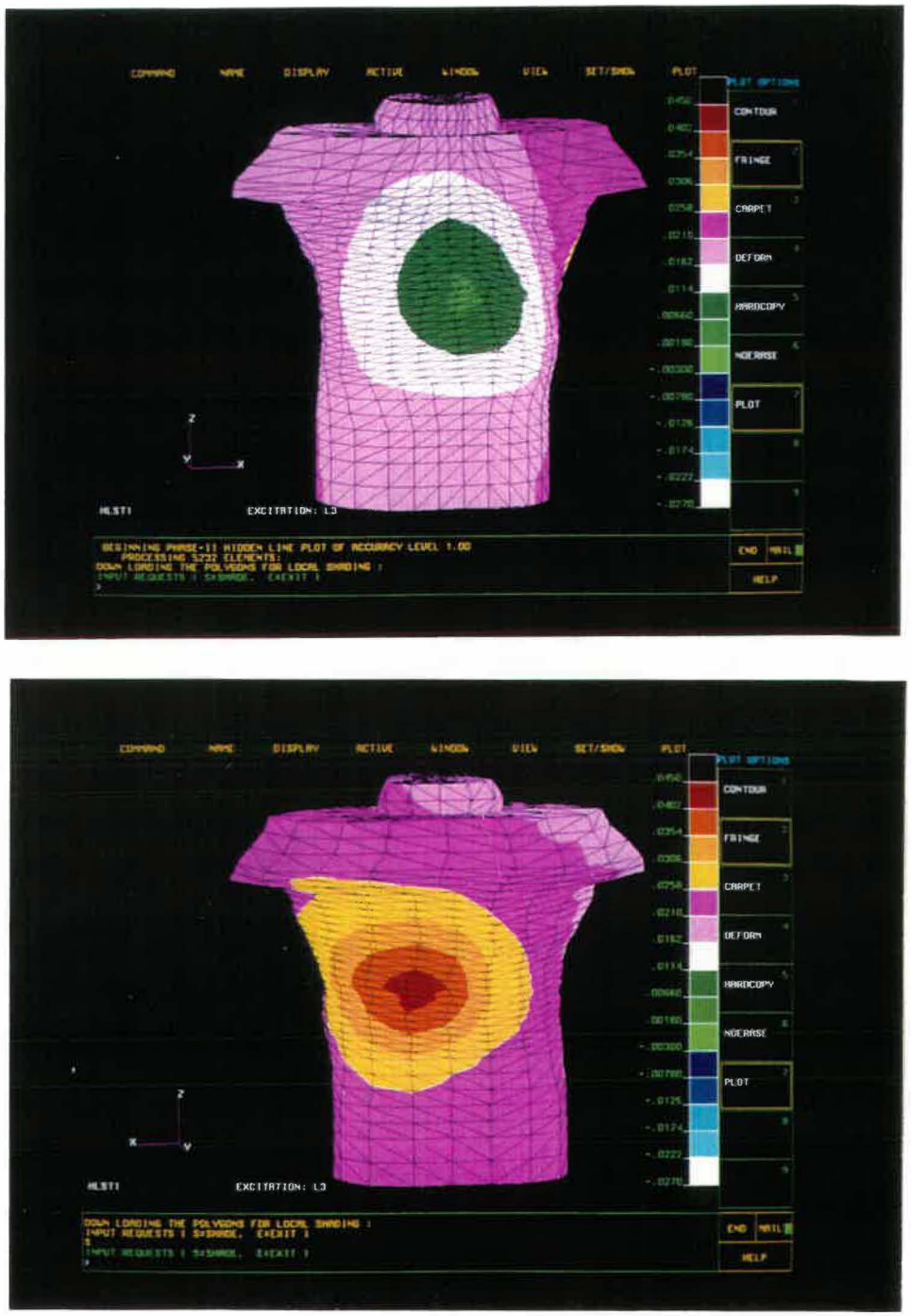

Figure 3.11: Computed body surface fringe maps as in Figure 3.7 for the $HLST_1$ model and the activation at location L_3.

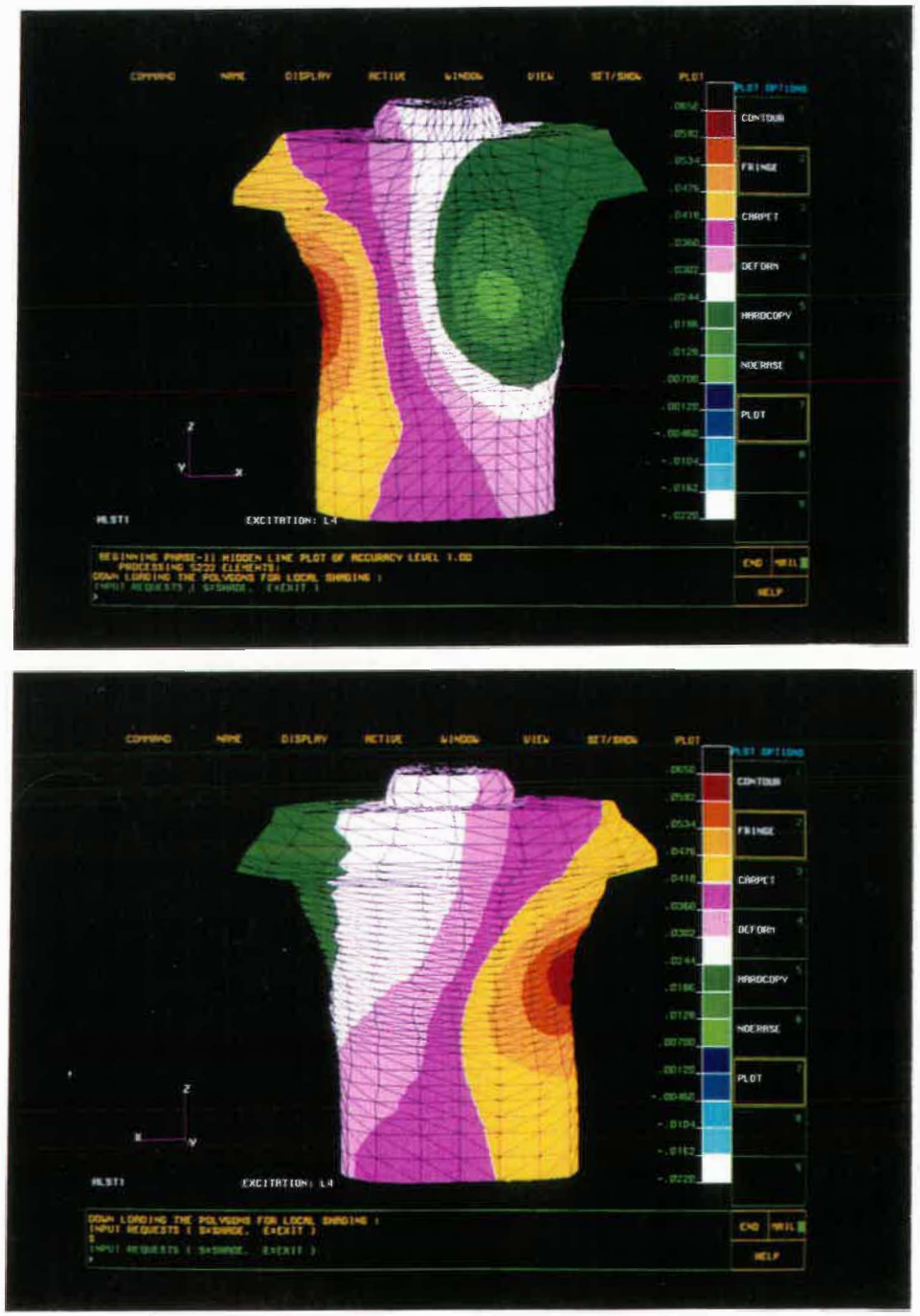

Figure 3.12: Computed body surface fringe maps as in Figure 3.7 for the $HLST_1$ model and the activation at location L_4.

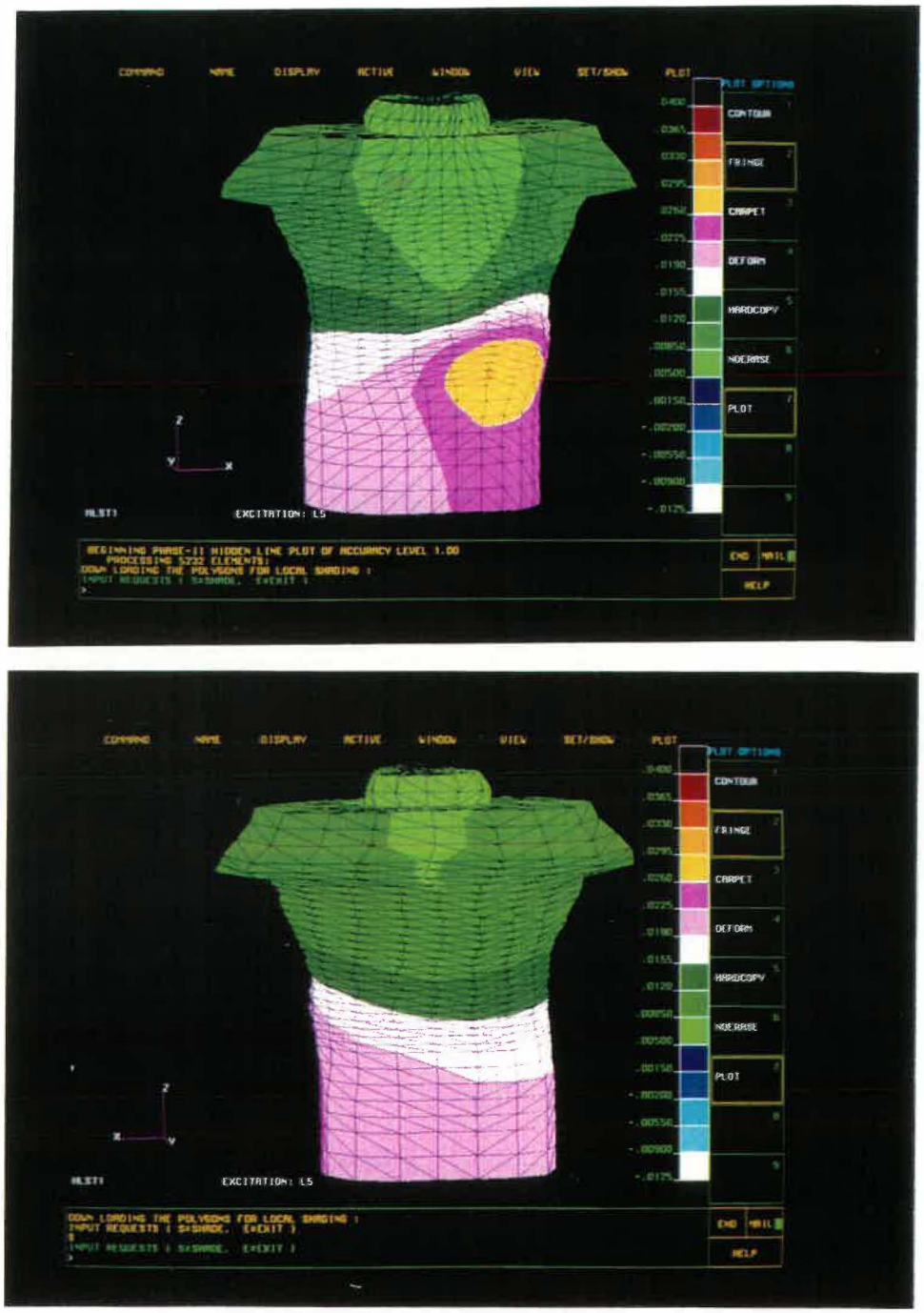

Figure 3.13: Computed body surface fringe maps as in Figure 3.7 for the $HLST_1$ model and the activation at location L_5.

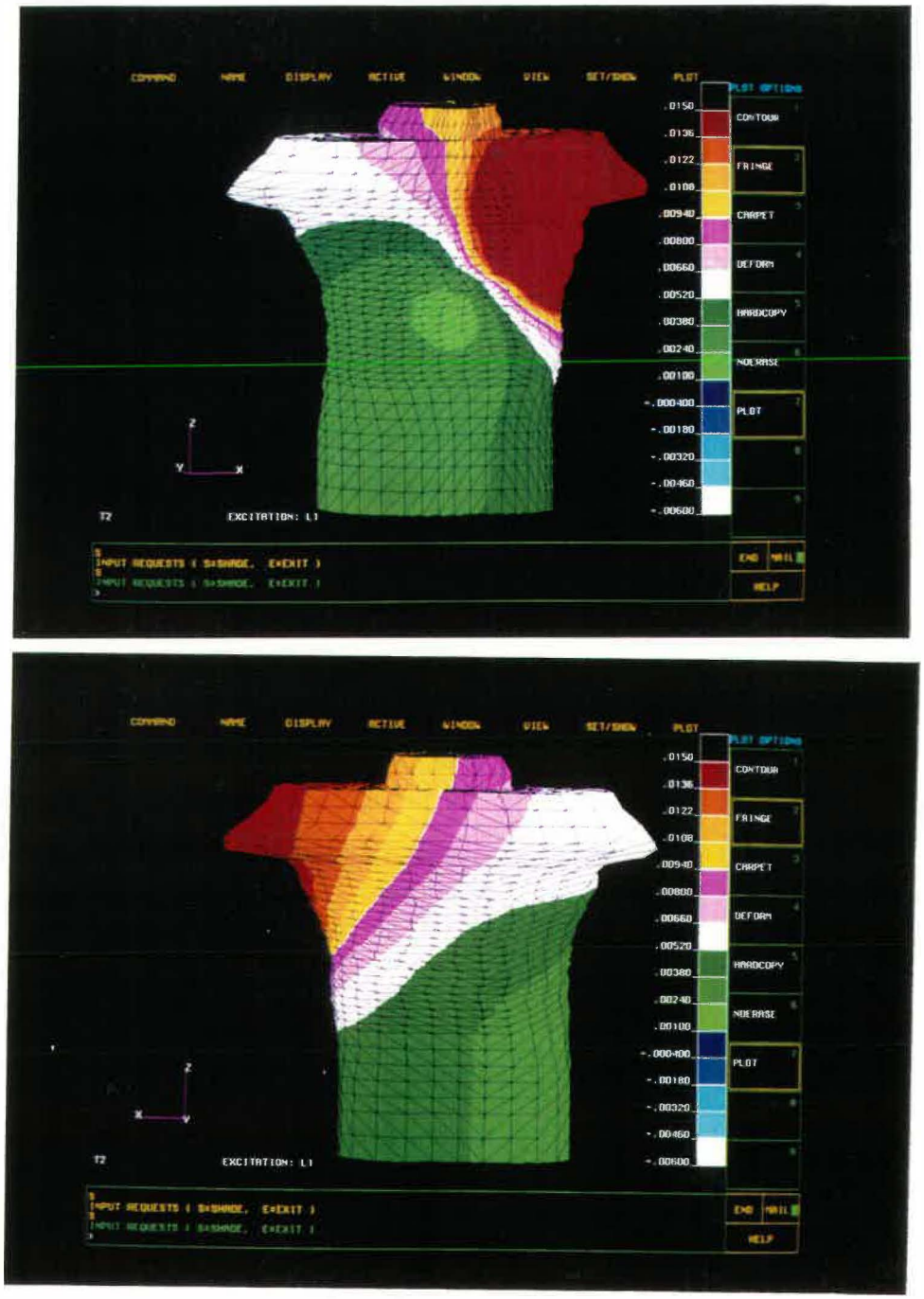

Figure 3.14: Computed body surface fringe maps as in Figure 3.7 for the T_2 model and the activation at location L_1.

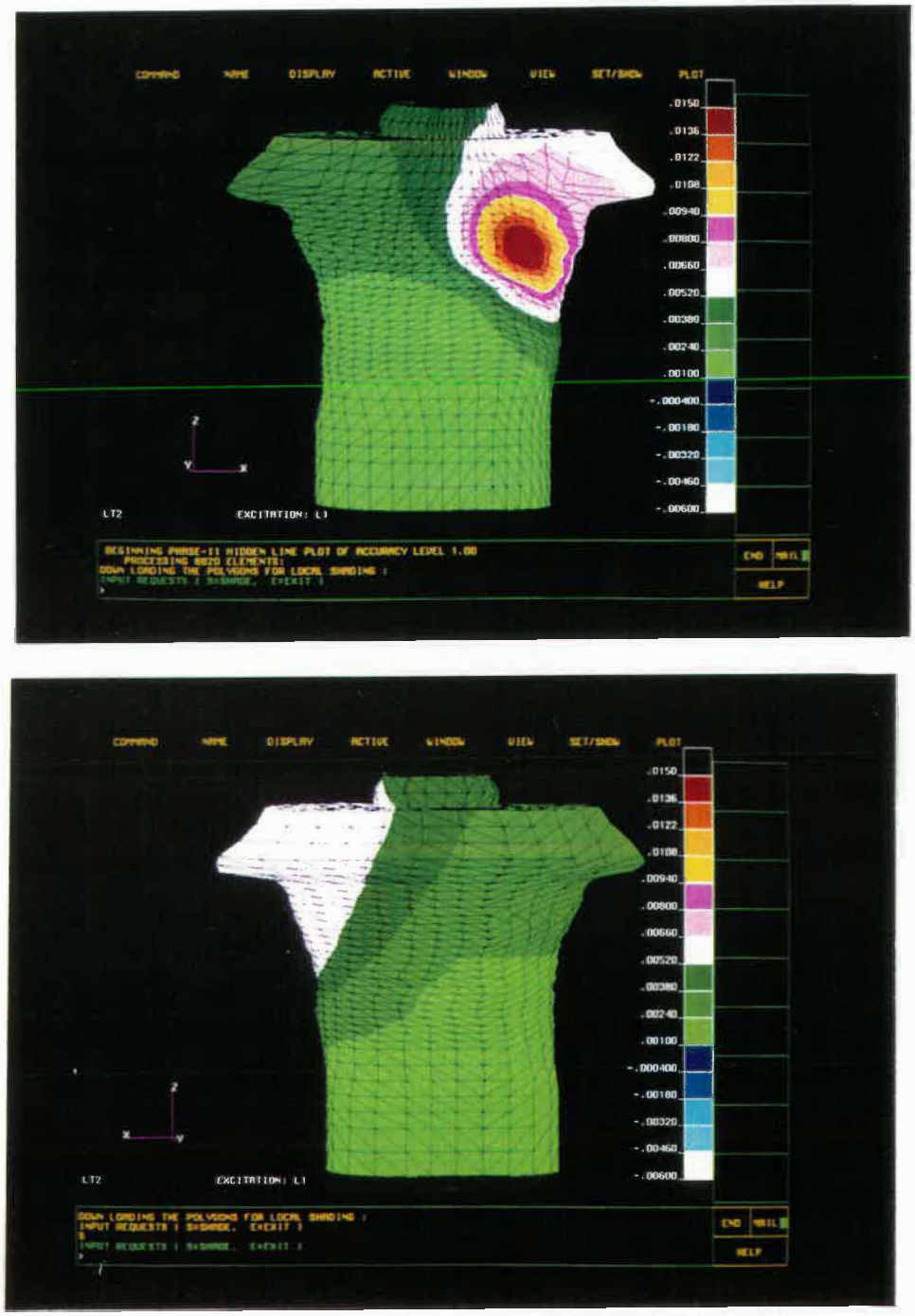

Figure 3.15: Computed body surface fringe maps as in Figure 3.7 for the LT_2 model and the activation at location L_1.

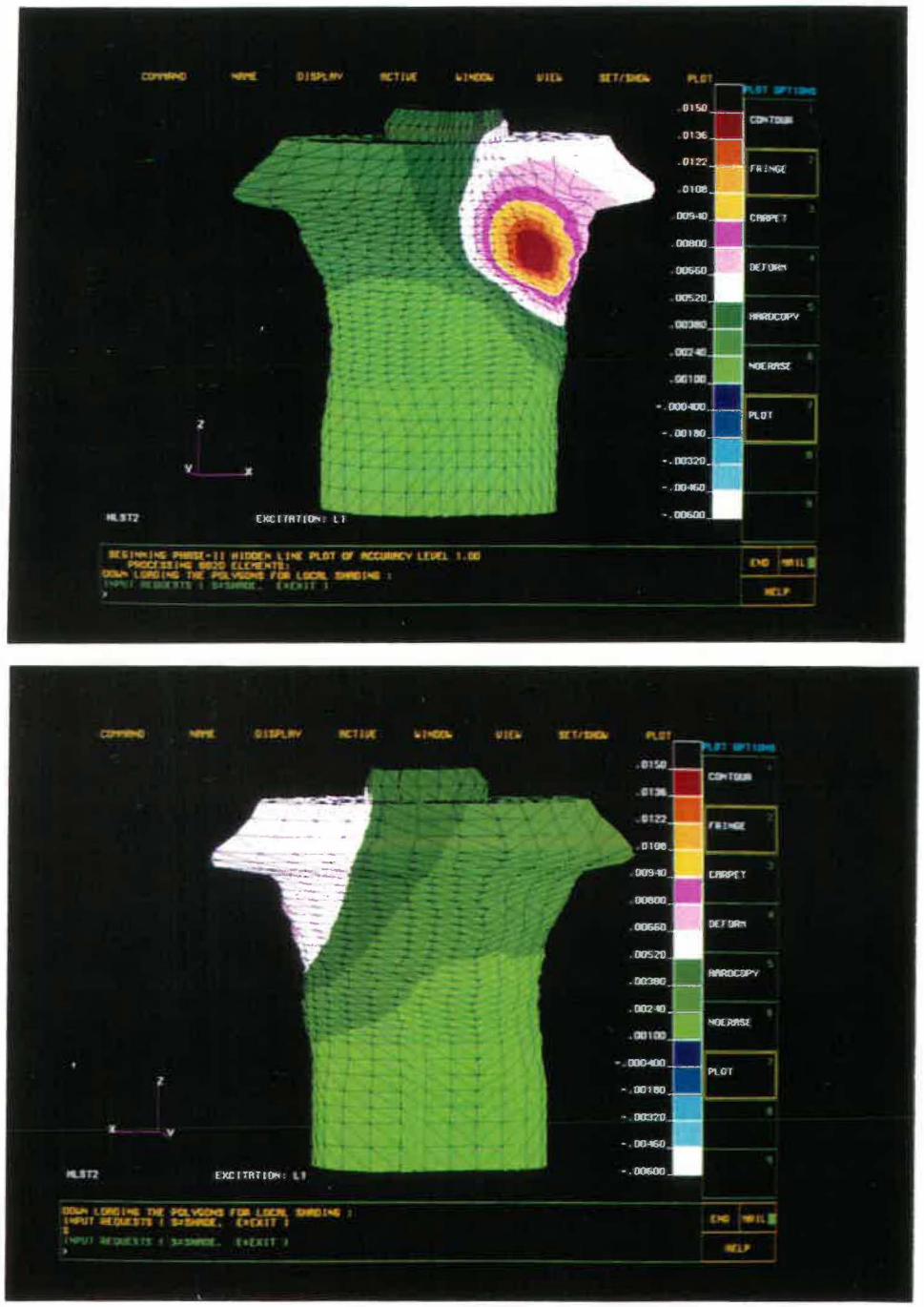

Figure 3.16: Computed body surface fringe maps as in Figure 3.7 for the $HLST_2$ model and the activation of heart surface at location L_1.

and the different torso models are presented in Appendix D. The simulated maps generally reproduced the main features of the measured maps, but some of the observed discrepancies may be attributed to a rotation of the epicardial electrode array.

3.2.2 Electric field maps

Electric field components have also been computed for all the forward simulations [59]. Fig. 3.19 shows the magnitude of the electric field over the torso model. Field calculation also allows us to deduce the current density distribution in the thorax volume. Further, current density distribution can be useful in studies for boundary characterization.

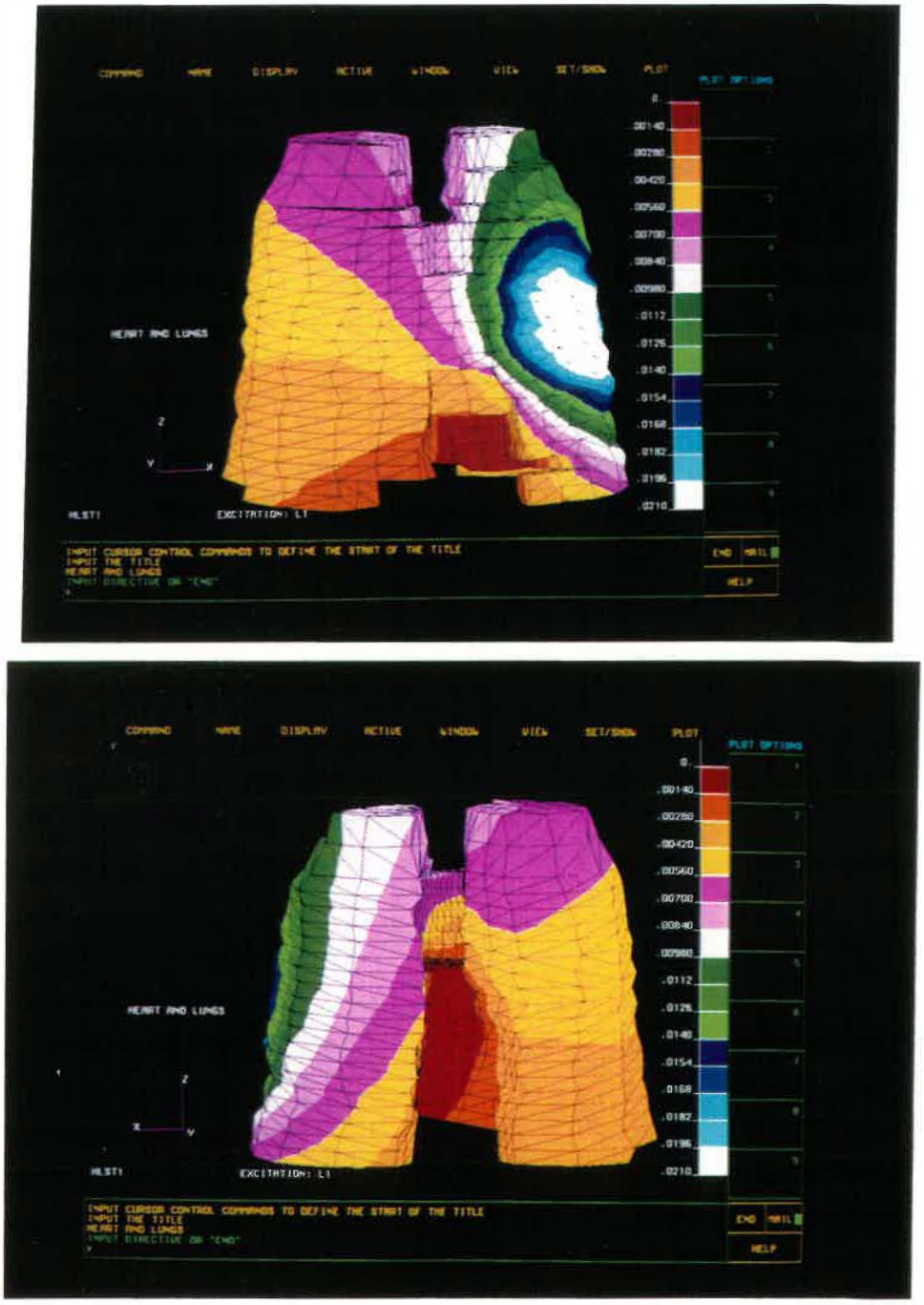

Figure 3.17: Isopotential fringes displayed on the heart and lungs calculated with FEM as in Figure 3.7 for the $HLST_1$ model and the activation of heart surface at location L_1.

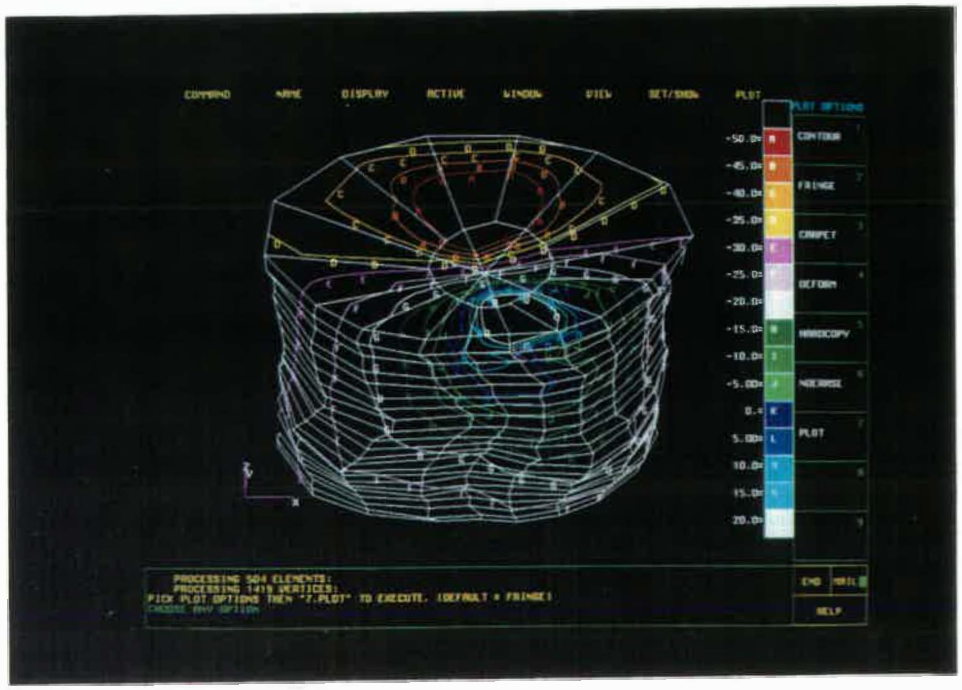

Figure 3.18: Calculated isopotential contours displayed on the frontal surface of the thorax and on a cross-section cut at about $1cm$ above the base of the heart.

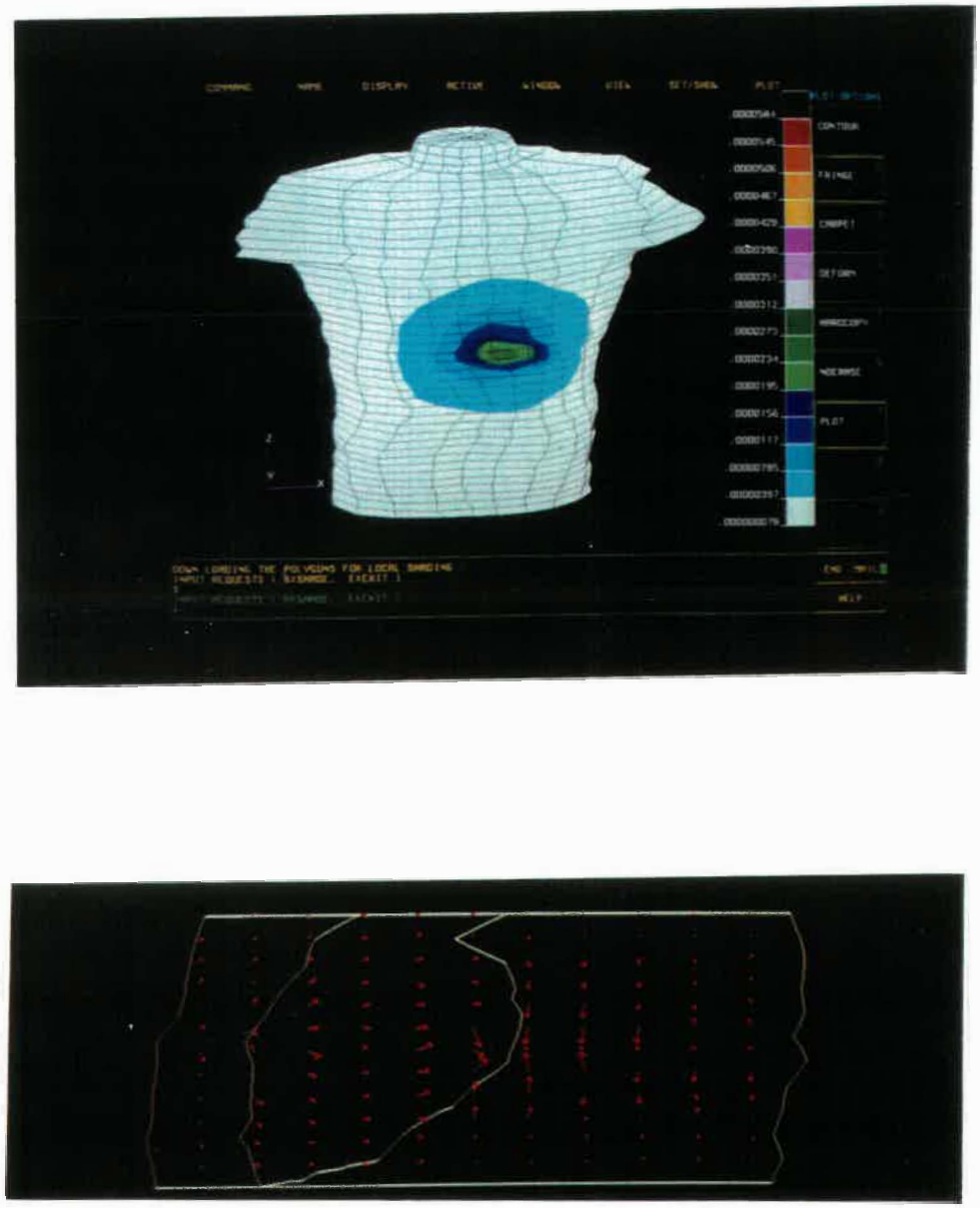

Figure 3.19: Top: anterior view of the T_1 model. Computed isofield map of electric field intensity due to the activation shown in Fig. 3.18. Bottom: side view showing the vector field across the heart boundary.

Chapter 4

The inverse problem: theory and methods

4.1 Mathematical description of the problem

Statement of the problem. Define $\phi(\xi)$ as the potential at any point ξ in region Ω which is bounded by the epicardial surface Γ_h and the body surface Γ_b (closed at the neck, shoulders and abdomen). One possible formulation of the inverse problem of electrocardiography consists in the evalution of the epicardial potential distribution, $\phi(\xi)$ on Γ_h, from the potential distribution on the thorax, $\Sigma \subset \Gamma_b$ (i.e., Σ is an open subset of Γ_b). It requires solving the Cauchy problem

$$\begin{cases} \nabla \cdot \sigma(\xi) \nabla \phi(\xi) = 0 & \text{in } \Omega \\ \frac{\partial \phi(\xi)}{\partial n} = 0 & \text{on } \Gamma_b \\ \phi(\xi) = \phi_b(\xi) & \text{on } \Sigma \subset \Gamma_b \end{cases} \tag{4.1}$$

which is related to a second order elliptic operator. In this problem, both the potentials and the normal current density are specified on the same boundary surface (i.e., body surface).

Relation between the source and the data function. The present biophysical problem, describing the field distribution in the volume conductor Ω,

requires the solution of the following Fredholm integral equation of the first kind,

$$\int_{\Gamma_h} h(\xi,\zeta)f(\zeta)d\zeta = g(\xi) \quad for \;\; \zeta \in \Gamma_h \;\; and \;\; \xi \in \Gamma_b \tag{4.2}$$

where $g(\xi)$ denotes the data function (the body surface potentials), $f(\zeta)$ denotes the source function (the epicardial potentials) and $h(\xi,\zeta)$ is a kernel that relates $f(\zeta)$ to $g(\xi)$. The kernel $h(\xi,\zeta)$ is the forward transfer function and it includes the influence of the complete volume conductor properties, including topological and material properties, as shown in chapter 3. The kernel also describes the continuous interaction between the source function and the data function. Here, we are dealing with a convolution of the first type: the relation between the source and the data function is linear, a process in which a source function is smeared by the response properties of the *medium* and the *recording instruments* into what we call the measured data. The mapping $X \ni f \rightarrow g \in Y$, defined by equation (4.2), can be described in terms of a linear operator $\mathcal{H} \;:\; X \rightarrow Y$, which transforms a function in X into a function of Y in the Hilbert space, according to an ill-posed operator,

$$\mathcal{H}f = g \tag{4.3}$$

where $\mathcal{H}$ is associated with the kernel h and the relevant limits. A mapping $\mathcal{H}^+ \;:\; Y \rightarrow X$ is then defined by the relation

$$\mathcal{H}^+ g = f \tag{4.4}$$

where the operator $\mathcal{H}^+$ is called the generalized inverse of $\mathcal{H}$.

Solution types. Depending upon the problem, either $\mathcal{H}$ or f may be defined as the system operator. In a system identification problem, the goal is to determine the system operator $\mathcal{H}$, given the response to a specific input. On the other hand,

the objective might be to solve for the excitation source, given the distributed field g. In this case, the excitation source would be denoted by f and the system operator would be denoted by $\mathcal{H}$. Given $\mathcal{H}$ and f, the forward problem (solving for the output g) is relatively straightforward. However, the inverse problem which consists of solving for f, given $\mathcal{H}$ and g, is much more difficult. If the function g belongs to the range of the operator $\mathcal{H}$, $R(\mathcal{H})$, then there is a possibility for an exact solution. Otherwise, which is the case in the present applied problem, it is required to find appropriate techniques for the resolution of the problem [47].

Ill-posedness. Hadamard [30] introduced the notion of a well-posed (or correctly-posed or properly posed) problem in the early 1900's during his studies of the Cauchy problem. A problem is said to be well-posed if the following conditions are satisfied:

(i) the solution $f(\zeta)$ exists for each element $g(\xi)$ in the data space Y;

(ii) the solution $f(\zeta)$ is unique in the solution space X;

(iii) the inverse mapping $g \rightarrow f$ is continuous (i.e., small perturbations in the data function $g(\xi)$ result in small perturbations in the solution $f(\zeta)$ without the requirement of imposing additional constraints).

If any of the above conditions is violated, then the problem is said to be ill-posed.

Existence, uniqueness and stabilities. In general, the solution of an elliptic equation becomes unstable and very sensitive to small changes in conditions when Cauchy conditions are specified over an open boundary and it becomes over-specified for a closed boundary [44]. The analysis of any inverse problem involves

mathematical questions about the existence, uniqueness and stability of the solution. In the inverse problem of electrocardiography, the existence of the epicardial potentials corresponding to a given body surface potential map is evident. A theoretical proof of the uniqueness for the inverse problem of electrocardiography was reported for a homogeneous volume conductor and an expansion of the electric field in a multipolar series [42]; another report considered epicardial surface with a more general geometry and conductivity configuration and used Green's theorem [71]. On the other hand, the stability issue has not been addressed adequately as yet.

4.2 Stability analysis and limitations

Discrete relation between the source and the data vector. In practical electrocardiographic applications, the inversion problem has to be tackled numerically since an exact analytical solution cannot be found. Hence, discrete representation of the integral equation (4.3) by a finite set of linear algebraic equations is required, i.e.,

$$\mathbf{Hf} = \mathbf{g} \tag{4.5}$$

so that the operator $\mathcal{H}$ is approximated by a matrix $\mathbf{H}$. Also, the source and data functions are represented by finite sets of approximate values, the unknown characteristic samples f_i and the experimental data g_i, and they are viewed as components of the source and data vectors, $\mathbf{f}$ and $\mathbf{g}$, which are linear functionals of $f(\zeta)$ and $g(\xi)$ respectively. The reduction of the integral equation to the matrix system degrades the conditioning of the linear system.

The following analysis is an attempt to quantify the numerical instability using

singular functions and matrix-vector norm analysis.

4.2.1 Singular function expansion

It is possible to develop an expansion of the source function in terms of the singular functions of the kernel. Approximations of the singular functions of the kernel must be obtained by using appropriate numerical techniques. Representing the singular functions by finite dimensional vectors leads to the singular value decomposition (SVD) of the kernel matrix $\mathbf{H}$. The SVD generalizes the more traditional eigensystem decomposition and provides a discrete analogue of the singular function analysis.

Let $\lambda_1^2, ..., \lambda_p^2$ be the positive eigenvalues of the symmetric matix $\mathbf{H}^T\mathbf{H}$, and let $\mathbf{v}_1, ..., \mathbf{v}_p$ be the corresponding orthonormal eigenvectors, i.e.,

$$\mathbf{H}^T\mathbf{H}\mathbf{v}_k = \lambda_k^2\mathbf{v}_k \quad ,(\mathbf{v}_k, \mathbf{v}_l) = \delta_{kl} \tag{4.6}$$

and let $\mathbf{u}_k = \lambda_k^{-1}\mathbf{H}\mathbf{v}_k$, then it follows readily that

$$\mathbf{H}\mathbf{H}^T\mathbf{u}_k = \lambda_k^2\mathbf{u}_k \quad ,(\mathbf{u}_k, \mathbf{u}_l) = \delta_{kl} \tag{4.7}$$

where the singular vectors $\mathbf{v}$ and $\mathbf{u}$ are eigenvectors of the symmetric matrices $\mathbf{H}^T\mathbf{H}$ and $\mathbf{H}\mathbf{H}^T$, hence they can be organized to form orthonormal bases of dimension m and n, respectively, with $\lambda_k \geq 0 \; \forall \; k$. From this, the SVD of the $m \times n$ matrix $\mathbf{H}$ with $m \geq n$ can be deduced; in matrix notation,

$$\mathbf{H} = \mathbf{U}\Lambda\mathbf{V}^T \tag{4.8}$$

where $\mathbf{U}$ and $\mathbf{V}$ are orthonormal matrices whose columns comprise the singular vectors $\mathbf{u}_i$ and $\mathbf{v}_j$, respectively, and Λ is a rectangular $m \times n$ matrix whose only

non-zero elements are the singular values $\lambda_1, ..., \lambda_n$ along the diagonal. More explicitly,

$$\begin{aligned}
\Lambda &\equiv diag(\lambda_1, \quad \lambda_2, ..., \lambda_n), \quad \lambda_j = j-th \ singular \ value \ of \ \mathbf{H}, \\
\mathbf{U} &\equiv eigenspace \ of \ \mathbf{H}\mathbf{H}^T, \\
\mathbf{V} &\equiv eigenspace \ of \ \mathbf{H}^T\mathbf{H}.
\end{aligned}$$

Then, each $\mathbf{Hf}$ in $R(\mathbf{H})$ admits an expansion in terms of the $\mathbf{u}_1, ..., \mathbf{u}_p$,

$$\mathbf{Hf} = \sum_{k=1}^{p} \lambda_k(\mathbf{f}, \mathbf{v}_k)\mathbf{u}_k, \tag{4.9}$$

where $(.,.)$ denotes the inner product of two vectors. The SVD provides a stable process for determining the rank of a matrix and for constructing least squares solutions to a linear system [39].

Matrix-vector norms. There exist numerous definitions of norms to quantify the instability of the system and the performance of the solutions. This subsection introduces the norms and their notations. Consider a function $f(\zeta)$, matrices $\mathbf{A}$ and $\mathbf{B}$, and a vector $\mathbf{v}$. The continuous function norms can be constructed for $f(\zeta)$, which is continuous over a given closed interval $[a, b]$, as follows:

$$\|f(\zeta)\| = (\int_a^b |f(\zeta)|^2 d\zeta)^{1/2} \tag{4.10}$$

$$\|f(\zeta)\|_\infty = \max_{a \le \zeta \le b} |f(\zeta)| \tag{4.11}$$

By analogy with the above equations, the length of a vector, $\mathbf{v} \in \Re^n$, satisfies the p-norm $(1 \le p \le \infty)$,

$$\|\mathbf{v}\|_p = (\sum_{i=1}^{n} |v_i|^p)^{1/p}, \tag{4.12}$$

the Euclidean norm (i.e., $p = 2$),

$$\|\mathbf{v}\|_2 = (\sum_{i=1}^{n} |v_i|^2)^{1/2} \equiv \|\mathbf{v}\|, \tag{4.13}$$

and the ∞-norm,

$$\|\mathbf{v}\|_\infty = \max_{1\leq i\leq n} |v_i|. \tag{4.14}$$

Also for any matrix norm,

$$\|\mathbf{AB}\| \leq \|\mathbf{A}\|\|\mathbf{B}\| \tag{4.15}$$

where $\mathbf{A}$ and $\mathbf{B}$ are square matrices, and matrix-vector norms,

$$\|\mathbf{Av}\| \leq \|\mathbf{A}\|\|\mathbf{v}\| \tag{4.16}$$

are also defined.

The matrix operator norm is defined as,

$$\|\mathbf{A}\| = \max_{\mathbf{v}\neq 0} \frac{\|\mathbf{Av}\|_p}{\|\mathbf{v}\|_p} \tag{4.17}$$

then, the matrix norm associated with the Euclidean norm is:

$$\|\mathbf{A}\| = (\max \lambda^2 : \mathbf{A}^T\mathbf{Av} = \lambda^2\mathbf{v})^{1/2} \tag{4.18}$$

or,

$$\|\mathbf{A}\| = \lambda_{\mathbf{max}} \tag{4.19}$$

where $\lambda_{\mathbf{max}}$ is the maximum singular value of $\mathbf{A}$. Finally, the matrix ∞-norm is defined as:

$$\|\mathbf{A}\|_\infty = \max_i \sum_{j=1}^{n} |\mathbf{A}_{ij}|. \tag{4.20}$$

4.2.2 Perturbations

A perturbation analysis gives insight into the stability and the perturbation bounds of equation (4.5) [25, 50]. Before computing any numerical solution, a stability

analysis of the linear system to perturbation in the data vector $\mathbf{g}$ and the kernel $\mathbf{H}$ is advisable. The major errors concerning the solution of the inverse problem of electrocardiography can be categorized into:

(i) measurements (e.g., epicardial and torso potentials, heart-torso geometry and torso conductivity);

(ii) discretization (e.g., number of electrodes and mesh generation); and

(iii) computation (e.g., round-off and truncation errors).

Perturbations in the data vector. A difficulty which arises in Fredholm equations of the first kind is the instability of the solution $\mathbf{f}$ with respect to the data vector $\mathbf{g}$ [67]. Perturbations may occur in the measured data due to discretization effects (number and location of thoracic electrodes) and noise contamination.

Consider the reduction of the equation (4.2) by specifying the data function only at discrete points, say ξ_i. Then it yields,

$$\int_{\Gamma_h} h(\xi_i, \zeta) f(\zeta) d\zeta = g(\xi_i) \quad i = 1, 2, ..., m. \tag{4.21}$$

Although no experimental noise error is involved in this discretization, it is clear that many functions $f(\zeta)$ can satisfy equation (4.21) without being solutions of equation (4.2). This reflects the fact that the discretized data points can never uniquely represent the data function, for example, any polynomial of degree $(m-1)$ or greater can pass through the node points of $\mathbf{g}$. Thus, information loss is introduced into the functional problem by discretization over the ξ variable.

Small changes in the data vector $\delta\mathbf{g}$ produce a change $\delta\mathbf{f}$ in the solution vector of equation (4.5) as,

$$\delta\mathbf{f} = \mathbf{H}^{-1}\delta\mathbf{g} \tag{4.22}$$

and the question is: how large may $\delta\mathbf{f}$ become relative to the solution? This requires norm analysis of the system equation so as to derive bounds for the solution error. Using equations (4.16) and (4.22), it follows that,

$$\|\delta\mathbf{f}\| \leq \|\mathbf{H}^{-1}\|\|\delta\mathbf{g}\|, \tag{4.23}$$

also

$$\|\mathbf{g}\| \leq \|\mathbf{H}\|\|\mathbf{f}\|. \tag{4.24}$$

Therefore, equations (4.23) and (4.24), give the following relation,

$$\frac{\|\delta\mathbf{f}\|}{\|\mathbf{f}\|} \leq C_H \frac{\|\delta\mathbf{g}\|}{\|\mathbf{g}\|} \tag{4.25}$$

where,

$$\begin{aligned} C_H &= \|\mathbf{H}\|\|\mathbf{H}^{-1}\| \\ &= \frac{\lambda_{max}}{\lambda_{min}} \end{aligned} \tag{4.26}$$

C_H is the condition number of the system, λ_{max} and λ_{min} are the maximum and minimum singular values of matrix $\mathbf{H}$. This clearly shows that small relative errors in the data can be quite magnified if the condition number $C_H \gg 1$.

Perturbations in the transfer matrix. Let $\delta\mathbf{H}$ be a perturbation in the transfer matrix due to an inaccurate modeling of the kernel function, such as variation in torso conductivity, position uncertainty of the leads or heart deformation during the cardiac cycle, i.e., $(\mathbf{H} + \delta\mathbf{H})(\mathbf{f} + \delta\mathbf{f}) = \mathbf{g}$. Then the relation,

$$\mathbf{H}\delta\mathbf{f} = -\delta\mathbf{H}(\mathbf{f} + \delta\mathbf{f}) \tag{4.27}$$

implies,

$$\frac{\|\delta\mathbf{f}\|}{\|\mathbf{f} + \delta\mathbf{f}\|} \leq C_H \frac{\|\delta\mathbf{H}\|}{\|\mathbf{H}\|}. \tag{4.28}$$

Again, the condition number becomes a magnification factor for perturbations in the linear system.

Combining the above two perturbations and applying them to the linear system (4.5) with $m \geq n$, then the errors of $\mathbf{g}$ and $\mathbf{H}$ entering into the solution $\mathbf{f}$ are modified by a factor which is essentially a function of C_H,

$$\frac{\|\delta\mathbf{f}\|}{\|\mathbf{f}\|} \leq \frac{\sqrt{2}+1}{\sqrt{2}-1}\frac{C_H}{1-\theta}\left[\frac{\|\delta\mathbf{H}\|}{\|\mathbf{H}\|}+\frac{\|\delta\mathbf{g}\|}{\|\mathbf{g}\|}\right]\left[1+\left(\frac{C_H}{2}\frac{\|\mathbf{g}-\mathbf{H}\mathbf{f}\|}{\|\mathbf{H}\mathbf{f}\|}\right)^2\right]^{1/2}. \tag{4.29}$$

It can be concluded that error in $\mathbf{f}$ is C_H times the errors of $\mathbf{H}$ and $\mathbf{g}$, provided that

$$\theta = \frac{\sqrt{2}+1}{\sqrt{2}-1}\frac{\|\delta\mathbf{H}\|}{\|\mathbf{H}\|}C_H < 1, \tag{4.30}$$

which implies that $C_H\,\|\mathbf{g}-\mathbf{H}\mathbf{f}\|/\|\mathbf{g}\|$ is not too large [48]. This is a perturbation analysis when applied to generalized overdetermined systems, see also [39].

4.2.3 Spectral analysis of the signal matrix

Only a finite amount of information about the source can be derived from the data. This amount depends upon the resolution limit set by the measured data, which is related to the number of linearly independent variables existing in the signal matrix $\mathbf{G}$. Applying SVD to the measured body surface potentials leads to a principal component analysis for both time and space. This spectral analysis provides useful knowledge about the data matrix, such as the degree of linear independence among the vectors in the data matrix. This is important, since the data matrix is directly involved in the inverse computation.

Define the potential signal matrix:

$$\mathbf{G}_{N_p \times N_t} = (\mathbf{g}_1, \mathbf{g}_2, ..., \mathbf{g}_{N_t}), \tag{4.31}$$

where,

$$\mathbf{g}_i = (g_{1,i}, g_{2,i}, ..., g_{N_p,i})^T \quad i = 1, 2, ..., N_t, \tag{4.32}$$

N_p is the number of electrodes on the body surface and N_t is the number of time instants at which samples were taken. Each row or column of $\mathbf{G}$ represents, respectively, the potential at a position or at a time instant. The SVD of the matrix $\mathbf{G}$ yields,

$$\mathbf{G} = \mathbf{U}_{G_{N_p \times r}} \mathbf{\Lambda}_{G_{r \times r}} \mathbf{V}^T_{G_{r \times N_t}} \tag{4.33}$$

where,

$$\begin{aligned} \mathbf{\Lambda}_G &\equiv diag(\lambda_{G_1}, \quad \lambda_{G_2}, ..., \lambda_{G_r}), \\ r &\equiv rank(\mathbf{G}). \end{aligned}$$

The matrix $\mathbf{U}_G$ can be regarded as position dependent, with its columns $\mathbf{u}_{G_i}$ being interpreted as orthonormal position signals, whereas $\mathbf{V}^T_G$ can be regarded as time dependent, with its columns $\mathbf{v}_{G_i}$ being interpreted as orthonormal time signals with energy $\mathbf{v}^T_{G_i}\mathbf{v}_{G_i} = 1$ since $\mathbf{V}^T_G\mathbf{V}_G = \mathbf{I}_r$ [18]. The vector columns $\mathbf{u}_{G_i}$ of matrix $\mathbf{U}_G$ and the vector columns $\mathbf{v}_{G_i}$ of matrix $\mathbf{V}^T_G$ are said to be the normalized principal components in *space* and *time*, respectively. The singular values λ_{G_i} are a measure of the relative importance of the principal components and provide information about the noise level in the signals [56].

4.2.4 Resolution limits

One of the main features of ill-posed problems is the lack of continuous dependence of the solution on the data, even in the absence of noise [47]. From the above perturbation analysis, it follows that the practical inversion problem can never give a solution without some limitations. Each process involved in the practical

inversion of ill-posed problems poses some limitations on the inverse resolution. These limitations are related to two conflicting objectives: the accuracy and the numerical stability.

At the modeling level, the closer the mathematical model describes the system, the larger the condition number of the associated computational problem becomes [47]. In modeling, it is desirable to minimize discretization errors by taking j (number of nodes) as large as possible. But this must be balanced by taking into account the worsening stability of the problem as j increases due to the increasing linear dependence of the adjacent rows and columns of $\mathbf{H}$. This feature of ill-posed problems,

$$C_H = \| \mathbf{H} \| \| \mathbf{H}^{-1} \| \rightarrow \infty \quad as \;\; j \rightarrow \infty \tag{4.34}$$

renders the inversion unstable. The above condition is directly related to the spread of the singular values of $\mathbf{H}$. As the transfer matrix becomes a closer approximation of the integral operator $\mathcal{H}$, the actual singular values will approach the zero limit (i.e., $\| \mathbf{H}^{-1} \| = 1/\lambda_{min} \rightarrow \infty$ since $\lambda_{min} \rightarrow 0$). The conditioning deteriorates to the level where impossible demands are made on the accuracy of the computations, even for uncontaminated data vectors. The rate of decrease of the singular values governs the degree of severity of the instability encountered in practice. This counterbalancing effect also occurs during the numerical inversion process where an optimization factor is involved. This optimization must be carried out so as to reach a compromise between accuracy and stability.

The stability analysis presented above, suggests that in practical inversion problems, the requirements for accuracy are less critical than those for stability. To tackle successfully an inversion problem, the following points should be considered:

(i) it is advisable to select a numerical method which is well suited to the inverse problem considered, since the error bounds are related to the method used;

(ii) there is an upper limit to the spatial or temporal frequencies that can be recovered in the source function, which is affected by the smoothing characteristic of the kernel and the properties of the data noise;

(iii) there is a limit on the temporal and spatial uniformity (accuracy and continuaty) of the recovered information;

(iv) computational errors (such as round-off and truncation errors) impose some limitations on the *a priori* computations (e.g., finding the SVD) and during numerical inversion.

4.3 Methodologies of solution

The numerical procedures used to solve the inverse problem of electrocardiography involve two stages;

(i) determination of the transfer matrix, i.e., computing an approximation of the transformation operator between the epicardial and body surface potentials (see section 4.3.4); and,

(ii) solution of the inverse problem proper, which is described in this section.

Definitions of physically acceptable or meaningful solutions are not completely included into the ill-posed operator equation and thus, classical solution methods are inadequate. Resolving the inverse potential problem involves different processes. The accuracy and rate of convergence of the numerical solution depends on:

(i) the modeling approach used to represent the problem domain, (e.g., the type and order of the elements used for constructing the model);

(ii) the numerical technique employed to stabilize the solution;

(iii) the strength of the constraint structure imposed to obtain physically realizable solutions; and

(iv) the profile of the source function so that it be sufficiently smooth that the recovery of information beyond the fundamental frequency limit set by the kernel is not required.

Regularizations. Regularization is a method for choosing the most physically realizable solution of an ill-posed problem, taking into account the external error on the data $\mathbf{g}$. Various schemes are available for modifying an ill-posed problem into an associated problem which is well-posed. Various aspects, functional analysis, optimization and numerical analysis, of these approaches can be found in Tikhonov and Arsenin [67], Payne [50] and Nashed [46]. The regularization may be categorized as follows [67, 46]:

(i) modifying the problem statement;

(ii) introducing a regularizing operator into the problem statement;

(iii) introducing probabilistic concepts into the problem statement in order to extend the problem to a stochastic one;

(iv) revising the space of the solution to which the acceptable solution belongs; and

(v) redefining what is meant by an acceptable solution so as to obtain a reasonable solution.

To solve the integral equations encountered in the inverse problem of electrocardiography, it is necessary to assure in some way the stability of the solutions. This can be achieved by using various regularization methods. This is particularly required for the numerical analysis of an ill-posed problem which involves solutions of finite-dimensional problems in order to obtain numerical approximations. This often consists of a two-stage algorithm that can be developed along two routes [47]:

(i) For the first route, some method of solution, such as regularization, is first applied to the ill-posed problem P in the function spaces, and then, numerical methods are used to approximate the solution of a well-posed problem (i.e., $P \rightarrow P^{\gamma} \rightarrow P^{\gamma,n}$).

(ii) For the second route, the ill-posed problem is first discretized, so as to become a finite-dimensional problem, and then numerical instabilities of the corresponding ill-conditioned system are solved by means of methods which are suitable for discrete ill-posed problems, (i.e., $P \rightarrow P^{n} \rightarrow P^{n,\gamma}$).

The stability of the inverse problem of electrocardiography can be restored by means of two classes of inverse solution methods, namely, the Tikhonov regularization (*TikReg*) and the control of dimensionality (*DimCon*); for detailed references see [67, 46].

4.3.1 Tikhonov regularization

The problem 4.5 is modified by the following variational approach: find the function f which minimizes,

$$\Upsilon_\gamma[f] = \| \mathcal{H}f - g \| + \gamma\mathcal{K}[f], \qquad \gamma > 0 \tag{4.35}$$

where,

$$\mathcal{K}[f] = \| \mathcal{L}f \|, \tag{4.36}$$

$\| \cdot \|$ in 4.35 and 4.36 are the Euclidean norms in $\Re^m$ and $\Re^n$, respectively, γ is the regularization parameter, $\mathcal{K}$ is the regularization operator and $\mathcal{L}$ denotes a linear operator. In the classical method, only the norm $\| \mathcal{H}f - g \|$ is involved. In the Tikhonov regularization method, a regularizer term ($\mathcal{K}[f]$) is introduced, which stabilizes the inversion by way of a *smoothness condition* on the source function. The regularizer provides a family of approximate solutions to a well-posed problem. The objective is to minimize the functional $\Upsilon_\gamma[f]$. This leads to the following Euler equation,

$$(\mathcal{H}^*\mathcal{H} + \gamma\mathcal{L}^*\mathcal{L})f = \mathcal{H}^*f \tag{4.37}$$

where $\mathcal{H}^*$ is the adjoint operator of $\mathcal{H} : \mathbf{X} \rightarrow \mathbf{Y}$. Equation (4.37) always has a stable solution with respect to f. Applying the zero-order Tikhonov regularization, i.e.,

$$\mathcal{K}[f] = \| f \| \tag{4.38}$$

then the solution to this problem in matrix form is,

$$\mathbf{f}_\epsilon^\gamma = (\mathbf{H}^T\mathbf{H} + \gamma\mathbf{I})^{-1}\mathbf{H}^T\mathbf{g}_\epsilon, \tag{4.39}$$

where $\mathbf{g}_\epsilon$ is the vector comprising the noisy torso potentials and $\mathbf{f}_\epsilon^\gamma$ is the vector comprising the epicardial potentials recovered from the noisy torso potentials using a regularization level γ. In the limit $\gamma \to 0$, the classical least squares solution is obtained, causing unstability. Then, the recovered epicardial potentials become too *irregular* (too large or too oscillatory). By increasing γ, the solution will be progressively stabilized. But it will depend on the value of the regularization parameter.

Also, the dimension of the solution subspace can be fixed to n, but the regularization parameter, γ, is then considered to be optimized. Let f, f^γ, $f^{\gamma,n}$ denote the approximate solutions of the problems P, P^γ and $P^{\gamma,n}$ in the absence of noise contamination in the data, and let f_ϵ^γ and $f_\epsilon^{\gamma,n}$ denote the resulting solutions in the presence of contamination in the data, where g is replaced by g_ϵ with $\| g - g_\epsilon \| \leq \epsilon$ for some noise $\epsilon > 0$. This leads to the three following levels of errors involved [47],

$$\begin{aligned} \| f_\epsilon^{\gamma,n} - f \| &\leq \| f_\epsilon^{\gamma,n} - f_\epsilon^\gamma \| + \| f_\epsilon^\gamma - f^\gamma \| + \| f^\gamma - f \| \\ &\leq e_1(\gamma, n, \epsilon) + e_2(\gamma, \epsilon) + e_3(\gamma) \end{aligned} \tag{4.40}$$

where e_1 is an error estimate related to the rate of convergence of the solution technique for the well-posed problem P^γ and for a given fixed γ; e_2 is an error estimate for noise contamination; and e_3 is a regularization error. Here, it is assumed that regularization provides the convergent solution, i.e., $f^\gamma \to f$ and $f^{\gamma,n} \to f^n$ as $\gamma \to 0$ for each fixed dimension n in the absence of contamination error. In equation (4.40), the third term (regularization error) tends to zero as $\gamma \to 0$, while the second term (magnification of contamination error) tends simultaneously to infinity. If we know an error estimate for the third term and a growth estimate for

second term, a suitable γ can be determined. Such estimates can be obtained for a particular regularization operator using additional information about the solution $\mathbf{H}_\gamma^+\mathbf{g}$, e.g. smoothness ($\mathbf{H}_\gamma^+\mathbf{g} \rightarrow \mathbf{H}_\gamma^{-1}\mathbf{g}$ in the absence of noise contamination in $\mathbf{g}$).

4.3.2 Resolution by control of dimensionality

The lack of stability in the inverse problem can also be remedied by the control of the dimensionality. As shown in section 5.2.1, equation (4.37) can be expressed in terms of the singular system of the operator $\mathcal{H} : X \rightarrow Y$, which is defined as the set of the triples $\{\lambda_j, u_j, v_j\}_{j=1}^n$.

For the case of zero-order regularization,

$$\mathcal{L}f = \mathcal{I}f = f \tag{4.41}$$

This leads to the problem:

$$\begin{pmatrix} \mathbf{\Lambda}_{n\times n} \\ \mathbf{0}_{(m-n)\times n} \\ \gamma\mathbf{I}_n \end{pmatrix} \mathbf{Vf} \cong \begin{pmatrix} \mathbf{U}^T\mathbf{g} \\ \mathbf{0}_n \end{pmatrix}_{m+n} \tag{4.42}$$

Then, the solution to the problem (4.42) is [39],

$$\mathbf{f} = \mathbf{VP} \tag{4.43}$$

where the components of the vector $\mathbf{P}$ in terms of the singular functions of the kernel after truncating, say k terms, are given for $\gamma = 0$ by:

$$p_j = \begin{cases} \frac{1}{\lambda_j}\, g_j & j = 1, ..., k \\ 0 & j = k+1, ..., n \end{cases} \tag{4.44}$$

which is the least square solution, and for $\gamma > 0$, by:

$$p_j = \begin{cases} \frac{\lambda_j}{\lambda_j^2+\gamma^2}\, g_j & j = 1, ..., k \\ 0 & j = k+1, ..., n \end{cases} \tag{4.45}$$

where the g_j's are the components of the vector

$$\tilde{\mathbf{g}} = \mathbf{U}^T\mathbf{g}. \tag{4.46}$$

Therefore, the algorithm for determining $\mathbf{f}$ requires computing the components of $\mathbf{g}$ with respect to the basis $\{\mathbf{u}_j\}_{j=1}^n$, and multiplying these components by the corresponding window coefficient: $w_j = \lambda_j^2/\lambda_j^2 + \gamma^2$. The components of $\mathbf{f}$ with respect to the basis $\{\mathbf{v}_j\}_{j=1}^n$ are then obtained. The values of the window coefficients depend on the parameter γ and satisfy the following properties:

(i) $0 \leq w_j \leq 1$ for any $\gamma > 0$, and

(ii) $w_j = 1$ when $\lim \gamma \to 0$.

Analytically, matrix $\mathbf{H}$ can be considered either singular or not. However, in a numerical context, some of the singular values are not zero but are rather very small, causing the matrix $\mathbf{H}$ to be ill-conditioned. In that case, the direct solution methods may give a formal solution, but the solution vector may have oscillatory and/or wildly large components. In such cases, the solution vector $\mathbf{f}$ obtained by *zeroing* the small λ's and then using equation (4.43) will improve the condition of the system. The residual $|\mathbf{Hf} - \mathbf{g}|$ being smaller than both the direct method and the SVD solution where the small λ's are left nonzero. Unlike the previous method described in section 5.3.1, the truncation level is not fixed but it is adjusted according to a prescribed constraint for a given regularization parameter.

Consider the case where the data vector is noise free, comparing the regularized solution (4.45) with the unregularized solution (4.44) shows that the expansion

coefficients have the form,

$$\frac{g_j}{\lambda_j} \rightarrow \frac{\lambda_j}{\lambda_j^2 + \gamma^2} g_j = \frac{g_j}{\lambda_j} \left(\frac{\lambda_j^2}{\lambda_j^2 + \gamma^2} \right). \tag{4.47}$$

The expression inside the brackets represents the effect of filtering out the singular functions associated with the small singular values, i.e. eliminating the high frequency components. For the case $\lambda_j^2 \gg \gamma$ the filter factor becomes closer to unity and there is no significant distortion in the recovered source vector, but as γ increases beyond λ^2, a high frequency cut-off appears in the solution.

When noise contamination is present in the data, an extra error term is introduced in equation (4.45), i.e., $\mathbf{g}_\epsilon = \mathbf{g} + \delta\mathbf{g}$. The noise term can be isolated to give:

$$p_j = \begin{cases} w_j g_j + w_j \delta g_j & j = 1, ..., k \\ 0 & j = k+1, ..., n \end{cases} \tag{4.48}$$

The effect of reducing the dimensionality on the error in the second term is clear, when using an arbitrary large value of γ, but it counterbalances the distortion induced in the first term by introducing more high frequency cut-off in equation (4.48).

4.3.3 Estimators and the discrepancy principle

Each method of solution, considering both the accuracy and the stability of the inverse solution, involves a critical parameter whose optimal value is crucial to the numerical implementation of the method. For the Tikhonov regularization it is the regularization parameter, γ, or the choice of the regularization operator. For the truncation method, it is the number of terms to be included. This section presents the principles that guide the choice of these parameters, the type of the

estimates and *a priori* information that is needed to arrive at an optimal value for these parameters.

Let $\hat{\mathbf{f}}$ denote the computed inverse solution obtained after optimizing either the regularization parameter γ (i.e., $\hat{\mathbf{f}} \equiv \hat{\mathbf{f}}_\epsilon^{\gamma,n}$) or the truncation level k (i.e., $\hat{\mathbf{f}} \equiv \hat{\mathbf{f}}_\epsilon^{k,\gamma}$).

Discrepancy criterion. If an estimate of the rms value of the measurement noise, ϵ^2, is known, then the guiding principle for the choice of the regularization parameter and the truncation level can be based on the discrepancy criterion given by [26],

$$find \begin{cases} \gamma > 0 \\ or \\ 1 \leq k \leq n \end{cases} : \quad \| \mathbf{H}\hat{\mathbf{f}} - \mathbf{g}_\epsilon \| / N_p = \epsilon^2. \tag{4.49}$$

This approach for obtaining quasi-optimal values is not feasible in the present application, since a reliable estimate of ϵ^2 is not available [13].

Bounded norm constraint. Another approach can be to seek solutions such that,

$$find \begin{cases} \gamma > 0 \\ or \\ 1 \leq k \leq n \end{cases} : \quad \| \hat{\mathbf{f}} \| \leq BNC \tag{4.50}$$

in which the norm of the recovered solution is bounded by a given value (BNC). The BNC in the present case can be set by the norm of the measured epicardial potentials, $\mathbf{\Phi}_h$. This constraint prevents an excessive norm value for $\hat{\mathbf{f}}$ that renders a solution unacceptable. It can be related to the minimum energy distribution since $\| \hat{\mathbf{f}} \|$ is proportional to the ohmic losses. But this technique does not give control on how close $\hat{\mathbf{g}}_\epsilon \in \mathbf{Y} = \mathbf{HX}$ is to $\mathbf{g}_\epsilon$.

Optimal estimate. When the measured epicardial potential vector, $\mathbf{\Phi}_h$, is known experimentally (which is the present case), the guiding principle for choice

of parameters can be given by,

$$find \begin{cases} \gamma > 0 \\ or \\ 1 \leq k \leq n \end{cases} : \quad min \quad \| \hat{\mathbf{f}} - \mathbf{\Phi}_k \| \tag{4.51}$$

in which the recovered solution is referred to as the optimal estimate (OPT).

CRESO estimate. The Composite REsidual and Smooth Operator ($CRESO$) is an *a posteriori* technique which uses only the measured data and the geometry without requiring information about the type of errors or upper error bound of the measurements. This estimator determines a quasi-optimal regularization parameter value which is equal to the smallest positive value of the parameter γ which maximizes the difference $B(\gamma)$ between: i) the fit of the observations that recovered solution realizes, $\| \mathbf{H}\hat{\mathbf{f}} - \mathbf{g}_\epsilon \|^2$, and ii) the derivative of the smoothing term, $\gamma \| \mathbf{L}\hat{\mathbf{f}} \|^2$,

$$B(\gamma) = \gamma \| \mathbf{L}\hat{\mathbf{f}} \|^2 - \frac{1}{m} \| \mathbf{H}\hat{\mathbf{f}} - \mathbf{g}_\epsilon \|^2 \tag{4.52}$$

then the CRESO estimator is followed by finding the smallest positive γ among the relative maximizers of the function $C(\gamma)$ [13],

$$C(\gamma) = \frac{d}{d\gamma} B(\gamma) = \| \mathbf{L}\hat{\mathbf{f}} \|^2 + 2\gamma \frac{d}{d\gamma} \| \mathbf{L}\hat{\mathbf{f}} \|^2 \tag{4.53}$$

where $\mathbf{L} = \mathbf{I}$ for zero-order Tikhonov regularization.

Akaike information criterion. For ill-posed problems, a solution can be obtained with reasonable accuracy and stability by omitting some singular values with small amplitude [63]. But the question is to find the optimal truncation level k. To do this, the Akaike Information Criterion (AIC) can be used, which is defined as,

$$\det_{1 \leq k \leq n} : \quad min \quad [m \log(\mathbf{H}\mathbf{H}_k^+ \mathbf{g}_\epsilon - \mathbf{g}_\epsilon)^2 + 2k], \tag{4.54}$$

which depends only on the body surface potential data [1]. This estimator is based on the maximum likelihood estimates and finds the rank k so as to minimize the AIC expression.

4.3.4 Search schema

Numerical solutions using the inverse methods described above require search techniques to find the optimal value of γ for TikReg method or n for DimCon method. The following steps summarize the algorithm used here to obtain the optimal value of γ or n for each selected estimator.

TikReg.

(i) Choose an initial value of γ ($\gamma = 10^{-11}$), the total number of steps along with a number of logarithmic steps N, for $10^{1/N}$ ($N = 20$).

(ii) For each γ, compute the inverse solution $\hat{\Phi}_h$ using TikReg.

(iii) Determine the optimum γ according to one of the estimators BNC, OPT or CRESO.

DimCon.

(i) Fix γ.

(ii) For each value of n ($1 \leq n \leq 63$) compute the inverse solution using DimCon method. (iii) Determine the optimum n according to one of the estimators, BNC, OPT or AIC.

4.3.5 Determination of the transfer matrix

As shown in chapter 3, the finite element method reduces to the problem of solving a system of linear equations. Partitioning the global matrix into the submatrices $\mathbf{S}_{fh}$, $\mathbf{S}_{ff}$, $\mathbf{S}_{fb}$, $\mathbf{S}_{bh}$, $\mathbf{S}_{bf}$, $\mathbf{S}_{bb}$ which combine the transfer coefficients between the

free nodes and the epicardial nodes, the free nodes alone, the free nodes and the torso nodes, the torso nodes and epicardial nodes, the torso nodes and the free nodes, and the torso nodes alone, respectively, and $\mathbf{I}$ (an identity matrix) and setting $I_s = 0$, yields:

$$\begin{pmatrix} \mathbf{I} & 0 & 0 \\ \mathbf{S}_{fh} & \mathbf{S}_{ff} & \mathbf{S}_{fb} \\ \mathbf{S}_{bh} & \mathbf{S}_{bf} & \mathbf{S}_{bb} \end{pmatrix} \begin{pmatrix} \phi_h \\ \phi_f \\ \phi_b \end{pmatrix} = \begin{pmatrix} \phi_{h,i} \\ 0 \\ 0 \end{pmatrix} \tag{4.55}$$

where ϕ_h, ϕ_f and ϕ_b are the epicardial, free nodes and body surface potential vectors, respectively, and the $\phi_{h,i}$ are the prescribed potentials on the epicardial surface. Relating epicardial potentials to the body potentials by eliminating the free-node variables, yields

$$\mathbf{H}\phi_h = \phi_b, \tag{4.56}$$

where,

$$\mathbf{H} \equiv (\mathbf{S}_{bf}\mathbf{S}_{ff}^{-1}\mathbf{S}_{fb} - \mathbf{S}_{bb})^{-1}(\mathbf{S}_{bh} - \mathbf{S}_{bf}\mathbf{S}_{ff}^{-1}\mathbf{S}_{fh}). \tag{4.57}$$

Transfer coëfficients

One approach for finding the transfer-coefficient matrix is by extracting the sub-matrices from the global matrix, as shown above. Another approach was used and it consists of directly computing the forward model as follows. Discretization of the problem region forms a set of nodes located at $\xi_{h,i}$ on the epicardial surface, and another set located at $\xi_{b,j}$ on the body surface. Denoting the basis functions by h_{ij}, equation (4.56) can be written as

$$\phi_b(\xi_{b,j}) = \sum_{i=1}^{N_h} h_{ij}\phi_h(\xi_{h,i}) \qquad , j = 1, 2, ..., N_b. \tag{4.58}$$

As a basis for the Dirichlet condition on Γ_h, we define a set which takes the value one on node i and zero in all the others, i.e.,

$$\phi_h(\xi_{h,i}) = (u_k(\xi_1), u_k(\xi_2), ..., u_k(\xi_{N_h}))^T \tag{4.59}$$

$$u_k(\xi_{h,i}) = \begin{cases} 1, & \text{if } i = k; \\ 0, & \text{otherwise.} \end{cases} \quad k = 1, 2, ..., N_h \tag{4.60}$$

Computing the torso potentials using the FEM, then produces,

$$\phi_{b,k} = (h_{1k}, h_{2k}, ..., h_{N_b k})^T, \tag{4.61}$$

for an epicardial node k. Solving for all k then yields the transfer coefficient matrix,

$$\mathbf{H} = \{\phi_{b,1}, \phi_{b,2}, ..., \phi_{b,N_h}\}. \tag{4.62}$$

The second approach was chosen because it does not require extraction and computation of the submatrices and because it uses the forward computation which has already been validated.

Chapter 5

The inverse problem: computational analysis

5.1 Performance criteria

Let us denote by $\{t_i; i = 1, 2, ..., N_t\}$ the sequence of time instants during the QRS complex, and by $\{\xi_j; j = 1, 2, ..., N_h(or N_b)\}$ the location of the electrodes on the surface of the heart or of the thorax at which the potential values are considered. We define the following notations for space-time distributions:

$\phi_h(t_i, \xi_j); 1 \leq i \leq N_t, 1 \leq j \leq N_h$: the measured epicardial potentials;

$\hat{\phi}_h(t_i, \xi_j); 1 \leq i \leq N_t, 1 \leq j \leq N_h$: the recovered epicardial potentials;

$\phi_b(t_i, \xi_j); 1 \leq i \leq N_t, 1 \leq j \leq N_b$: the measured body surface potentials;

$\hat{\phi}_b(t_i, \xi_j); 1 \leq i \leq N_t, 1 \leq j \leq N_b$: the simulated body surface potentials.

If the time t is fixed, then the spatial vector $\{\phi(t, \xi_j); j = 1, 2, ..., N\}$ is referred to as a potential map at time t. If the location ξ is fixed, then the temporal vector $\{\phi(t_i, \xi); i = 1, 2, ..., N\}$ is referred to as an epicardial electrogram for the epicardial potentials or as an electrocardiogram for the body surface potentials.

5.1.1 Accuracy criteria

Consider the space-time vector potentials $\Phi(.)$ and $\hat{\Phi}(.)$ as the measured and computed distributions, respectively. The comparison between these two distributions are calculated by means of the following accuracy criteria:

The spatial correlation coefficient at time instant t:

$$CC(\xi) \equiv \frac{((\hat{\Phi}(\xi) - \underline{\hat{\Phi}}(\xi)), (\Phi(\xi) - \underline{\Phi}(\xi)))}{\|\hat{\Phi}(\xi) - \underline{\hat{\Phi}}(\xi)\|.\|\Phi(\xi) - \underline{\Phi}(\xi)\|}, \tag{5.1}$$

where $\underline{\Phi(\xi)}$ is a vector whose components have all the same value as $\sum_{j=1}^{N} \Phi(\xi_j)/N_p$, and similarly for $\underline{\hat{\Phi}(\xi)}$;

The temporal correlation coefficient at a fixed position ξ:

$$CC(t) \equiv \frac{((\hat{\Phi}(t) - \underline{\hat{\Phi}}(t)), (\Phi(t) - \underline{\Phi}(t)))}{\|\hat{\Phi}(t) - \underline{\hat{\Phi}}(t)\|.\|\Phi(t) - \underline{\Phi}(t)\|}, \tag{5.2}$$

where $\underline{\Phi(t)}$ is a vector whose components have all the same value as $\sum_{i=1}^{N} \Phi(t_i)/N_t$, and similarly for $\underline{\hat{\Phi}(t)}$;

Root mean square difference at a time instant t:

$$RMSD(\xi) \equiv \frac{1}{\sqrt{N_p}}\|\hat{\Phi}(\xi) - \Phi(\xi)\| \; ; \tag{5.3}$$

Root mean square difference at a fixed position ξ:

$$RMSD(t) \equiv \frac{1}{\sqrt{N_t}}\|\hat{\Phi}(t) - \Phi(t)\|; \tag{5.4}$$

Spatial relative error at a given time instant t:

$$RE(\xi) \equiv \frac{\|\hat{\Phi}(\xi) - \Phi(\xi)\|}{\|\Phi(\xi)\|}; \tag{5.5}$$

Temporal relative error at a fixed position ξ:

$$RE(t) \equiv \frac{\|\hat{\Phi}(t) - \Phi(t)\|}{\|\Phi(t)\|}. \tag{5.6}$$

The following notations are also used :

$\|\mathbf{\Phi}_h(\xi)\|$ and $\|\mathbf{\Phi}_h(t)\|$ are the magnitudes of the measured epicardial potential map at a time instant t and the measured epicardial electrogram at a location ξ, respectively; $\|\hat{\mathbf{\Phi}}_h(\xi)\|$ and $\|\hat{\mathbf{\Phi}}_h(t)\|$ are the magnitude of the recovered epicardial potential map at a time instant t and the recovered epicardial electrogram at a location ξ, respectively; $\|\mathbf{\Phi}_b(\xi)\|$ and $\|\mathbf{\Phi}_b(t)\|$ are the magnitude of the measured body surface potential map at a time instant t and the measured body ECG at a location ξ, respectively; $\|\hat{\mathbf{\Phi}}_b(\xi)\|$ and $\|\hat{\mathbf{\Phi}}_b(t)\|$ are the magnitude of the simulated body surface potential map at a time instant t and the simulated body ECG at a location ξ, respectively.

The following notations are defined for the accuracy criteria $RMSD$, RE and CC:

$$RE_{d3,d4}^{d1,d2}(d5) \tag{5.7}$$

where $d1$ and $d2$ define the type of solution methods used:

$$d1, d2 \equiv \begin{cases} \gamma & \text{zero-order Tikhonov regularization (TikReg)} , \\ n, \gamma & \text{dimensionality control (DimCon)}, \end{cases} \tag{5.8}$$

where, γ is the regularization parameter and n is the truncation level; $d3$ defines the related surface:

$$d3 \equiv \begin{cases} h & \text{on the heart}, \\ b & \text{on the torso}; \end{cases} \tag{5.9}$$

$d4$ defines the type of estimator technique used:

$$d4 \equiv \begin{cases} OPT & , \\ CRESO & , \\ BNC & , \\ AIC & ; \end{cases} \tag{5.10}$$

and $d5$ represents space or time as:

$$d5 \equiv \begin{cases} \xi & , \\ t & . \end{cases} \tag{5.11}$$

For example, $RE^{\gamma}_{h,CRESO}$ is the relative error obtained using the Tikhonov regularization (TikReg) method with application of the CRESO estimator. These notations and abreviations are applied similarly for CC and $RMSD$.

5.1.2 Performance indices

Let us define the following efficiency indices that are used to compare different methods of solution:

$$IRMSD \equiv \frac{RMSD^{(1)}}{RMSD^{(2)}} \; Efficiency\ in\ terms\ of\ RMSD\ , \tag{5.12}$$

$$IRE \equiv \frac{RE^{(1)}}{RE^{(2)}} \; Efficiency\ in\ terms\ of\ RE\ , \tag{5.13}$$

$$ICC \equiv \frac{CC^{(1)}}{CC^{(2)}} \; Efficiency\ in\ terms\ of\ CC\ . \tag{5.14}$$

5.2 The measured potential data

In this study, the epicardial and the body surface potentials were recorded from a patient whose thoracic CAT scans were available. This patient had the Woff-Parkinson-White (WPW) syndrome and the epicardial data were recorded during antiarrhythmic surgery. The following describe briefly the measurement procedures which were carried out at the Sacré-Coeur Hospital, Montréal.

Epicardial potentials. The epicardial potentials were recorded with a technique previously developed to study the mechanisms of ventricular tachycardia in animal preparations [9]. The epicardial electrograms were measured during normal sinus rhythm with a sock electrode array comprising 63 unipolar leads positioned over both ventricles. A particular row of electrodes, as a reference,

overlies the left anterior descending coronary artery (LAD). The surgeon identifies the electrodes which overlay the major coronary arteries so as to provide anatomical landmarks.

The data acquisition was performed using a $PDP - 11/23^{+}$ computer which controlled an electrophysiological data interface consisting of 64 channels filtered with a bandpass of .05 to $200Hz$, sampled at $500Hz$ with a resolution of 10 bits, and stored on a magnetic disk [8].

Torso potentials. The body surface potentials were measured during an electrophysiological investigation performed before the surgery. The potentials were also recorded during normal sinus rhythm. A mapping system developed at the Institut de Génie Biomédical (CORDIC) was used. The recorded signals were amplified with a bandpass of 0.05 to $200Hz$, sampled at $500Hz$, and digitized with a 10 bit resolution. The beats were averaged for a period of 52 seconds.

Preprocessing of the epicardial and thoracic signals consisted of the following steps. The signals were corrected for baseline drift by a linear interpolation using isoelectric segments which were manually chosen during TP intervals. Any faulty or noisy lead was replaced by interpolating from the neighboring leads. The epicardial signals with their corresponding measured thoracic signals, which were recorded on different days for the same activation sequence on the same subject, were time-aligned by finding the maximum cross correlation between the two root-mean-square signals computed from the 63 epicardial and the 63 thoracic signals.

A magnitude plot of time-aligned RMS signals for the 63 epicardial and the 63 body surface leads is shown in Fig. 5.1. As can be seen the time alignment of the epicardial and thoracic signals was performed with a reasonable accuracy.

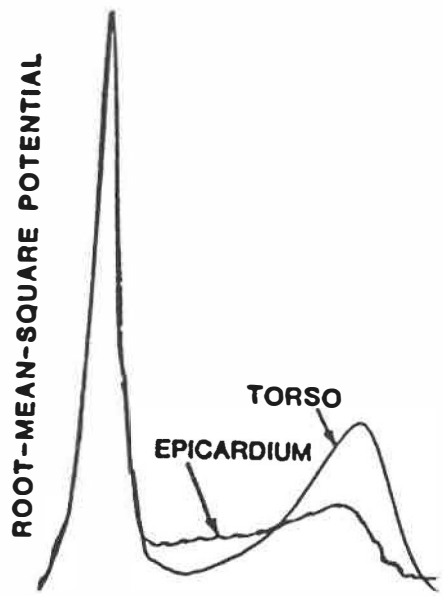

Figure 5.1: Magnitude of time-aligned RMS signals for the 63 epicardial and 63 thoracic leads from the patient who suffered from WPW syndrome; thoracic CAT scans were obtained from the same patient.

5.3 The heart prototype

One of the problems that were encountered was to find the epicardial electrode positions within the computer model. To overcome this difficulty, a heart prototype was built from the CT scan geometrical data. The heart prototype was made from thick cardboard pieces cut so as to correspond to each heart cross-section defined by the CT slices, and these pieces were glued together to form a complete heart. The heart prototype was then covered with the same sock electrode array that was used to perform the epicardial potential measurements. The sock electrode array was aligned according to the LAD reference line. This allowed us to

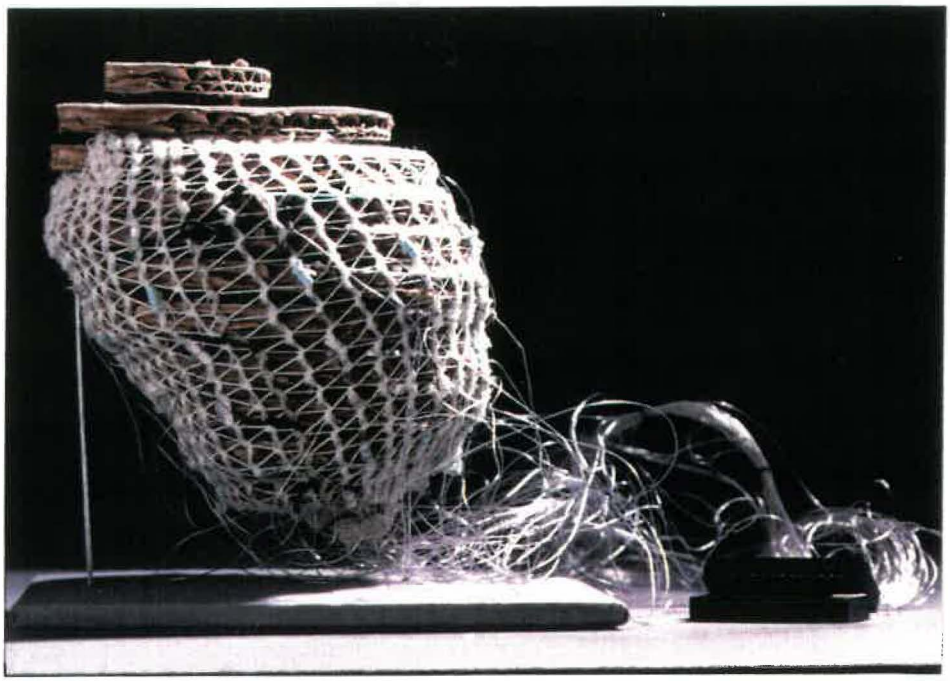

Figure 5.2: The heart prototype and the sock electrode array which was used to measure the epicardial potential distribution.

measure the location of each electrode over the heart prototype and within the computer model. Fig. 5.2 shows the heart prototype as the sock electrode array is positioned over the heart.

5.4 SVD analysis of the heart-torso models

The transfer matrix which relates epicardial potentials to the body surface potentials contains information about the topology and the electromagnetic characteristics of the medium as described in chapter 2. However, these properties are not fully represented in the model and there are some errors in the solution process

as detailed in chapter 4.

The degree of linear dependence among the vectors of the transfer matrix governs the stability of the solution and can be analyzed by finding the singular values of the transfer matrix. This was presented in chapter 4 for the cases where the potential data contain noise or the transfer matrix includes some error.

The SVD was applied to the computed transfer matrix of each of the six torso models (Table 2.3). In Fig. 5.3, the ratio $log(S_i/S_1)$ of the singular values of the transfer matrix for each model are plotted. The singular value curves differ from model to model. Both the inclusion of inhomogeneities and a higher mesh resolution cause some downward shift in the SVD curves. The influence of the spinal-region inhomogeneity has been found to be minimal on the SVD, compared with that of the lungs.

From SVD analysis, it can be deduced that the singular values do not decrease uniformly. Rather, three regions with different slopes can be observed. Fig. 5.4 presents these slope changes. The first part of the curve, with an approximate slope 0.16, provides the maximum projection power and occurs in the region with less than 9 singular values ($i < 9$). The slope of the second part was found to be 0.08 in the middle region, $9 < i < 45$, and finally, the third part had a slope of 0.19 in the last region ($45 < i < 63$). The importance of the contribution of the singular values in these three regions can be expected to be different. While the second region contributes less information content than the first part, the third part may introduce oscillatory components into the system.

The reasons for not having a complete observability in the transfer matrix can be explained as follows: (i) incomplete description and implementation of the material properties in the thorax, (ii) the discretization error involved in rep-

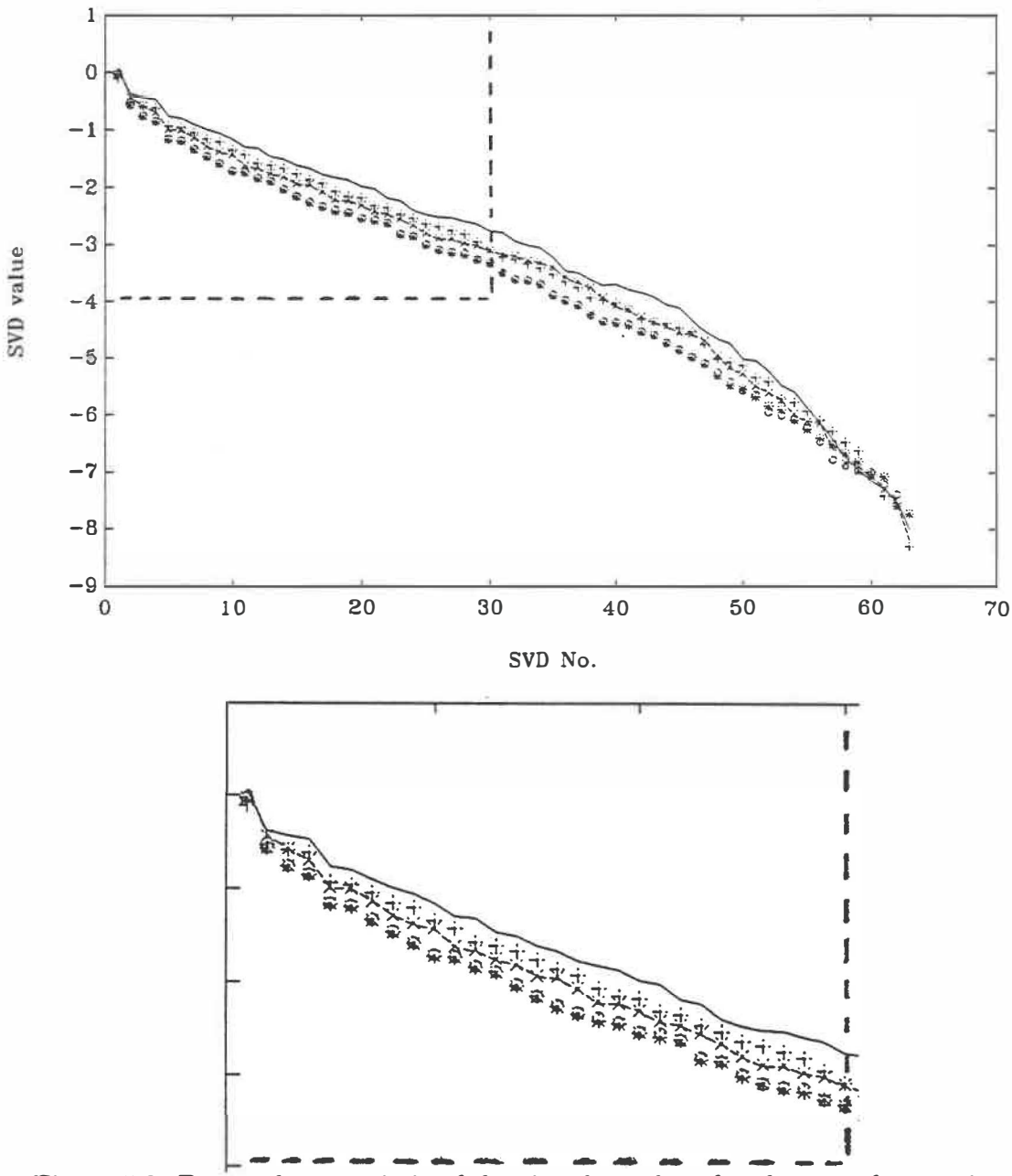

Figure 5.3: Decay characteristic of the singular values for the transfer matrices of the different heart-torso models. The curves are defined as: (–) T_1, (- -) LT_1, (x) $HLST_1$, (+) T_2, (o) LT_2 and (*) $HLST_2$. The inset is shown with a larger scale at the bottom.

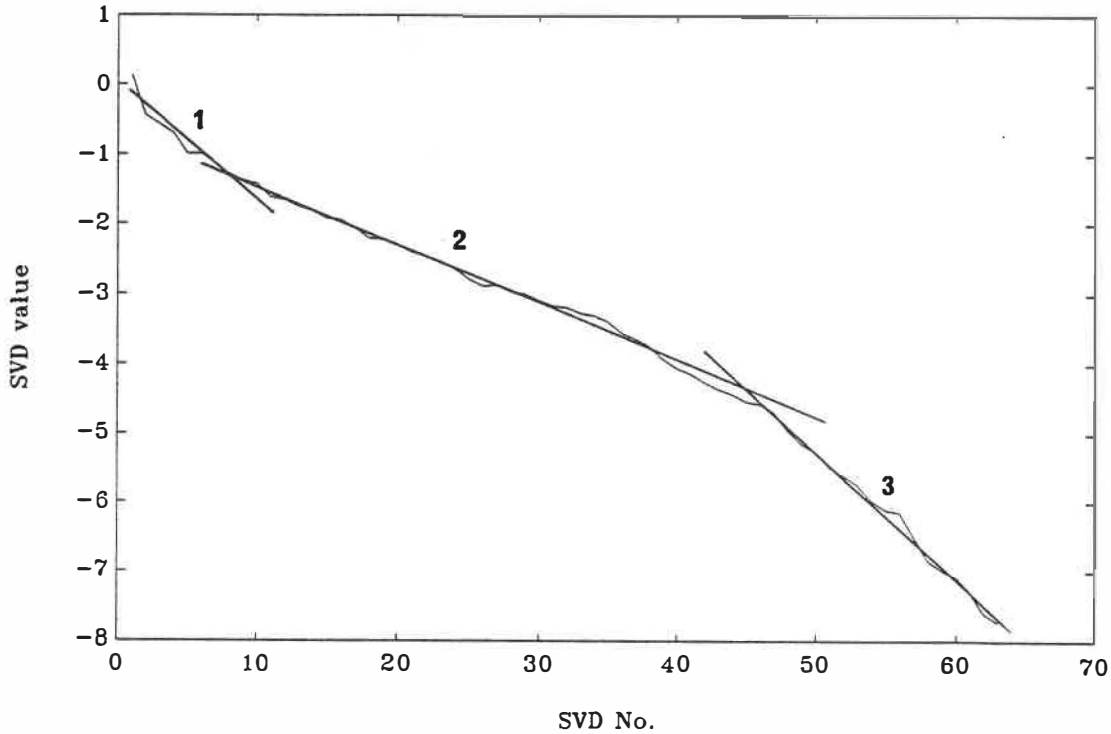

Figure 5.4: Decay of the singular values (logarithmic scale) of the transfer matrix of the $HLST_1$ model showing three regions with distinct rate of change.

resenting an infinite dimension by a finite one; and (iii) errors involved during computations. All these limitation factors impose a maximum bound for observability in the transfer matrix.

5.5 Spectral analysis of signal matrices

The spectral analysis of the potential data was carried out by applying the SVD technique as described in chapter 4. The decay of the singular values is plotted in Fig. 5.5. The singular values represent the relative importance of the principal components for time and space. The initial range decreases rapidly and a notice-

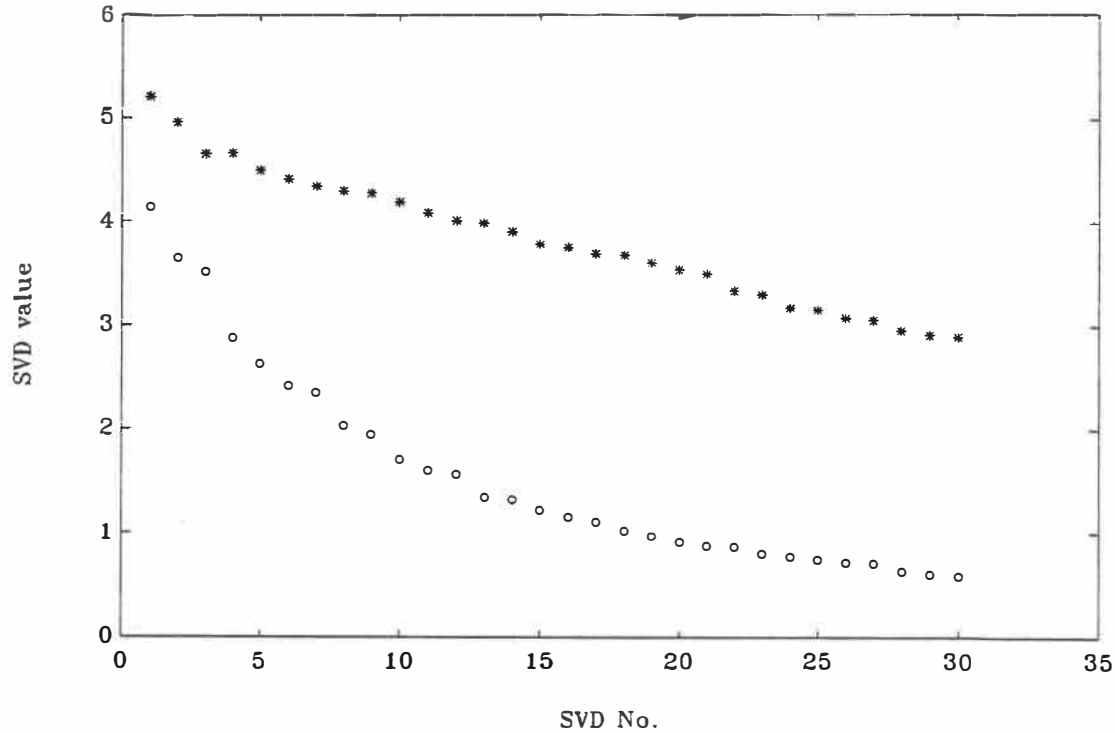

Figure 5.5: Decay of the singular values (logarithmic scale) of the signal matrices for the epicardium (*) and the torso (o).

able difference exists between the singular values of the measured epicardial and thoracic potential sets. This shows that the potentials are much more correlated on the surface of the torso than on the surface of the heart. For example, on the torso, the 7th largest eigenvalue is 100 times smaller than the first, whereas on the epicardium, the 23rd largest eigenvalue is 100 times smaller than the first. In other words, the information content that can be retrieved in the presence of noise is much more limited on the torso than on the heart. This explains very well the ill-posed nature of the inverse problem of electrocardiography and also the truncation approach to the inverse problem. According to the truncation approach, the higher-order orthogonal components, which are of minor influence, contain noise

and can be set to zero. Fig. 5.6 shows the first 8 principal components in time (i.e., the first 8 columns of V) and Fig. 5.7 illustrates the first 8 principal components in space (i.e., the first 8 columns of U). It is noted that as the eigenvector number increases, so do the temporal and spatial frequencies of the components.

The reasons for not having complete observability in the data matrix can be explained as follows: (i) noise in the measuement process, (ii) limitation of number of time and space samples and (iii) quantization error. All these factors impose a maximum bound for the observability in the signal data.

Few remarks can be made here. These spectral analysis results for the potential data are specific to the number and position of the electrodes. Also, this type of analysis can be used to study possible improvements in the number and position of electrodes. The singular values can be tested, if they show higher values when a different number of leads is used, then more observability in the potential data matrix is obtained. Or, considering the spatial distribution, one can increase the observability by increasing the number of electrodes in the regions with a higher curvature of the field.

5.6 Inverse simulations

The main purpose of inverse simulations presented in this section was to test the inverse procedures and their implementation. In addition, under noise free condition, these simulations can be used to compare the inverse procedures and examine the effects of conductivity inhomogeneities and mesh resolution of the torso model on the inverse results.

Two sets of inverse simulations were carried out. The first set is defined as

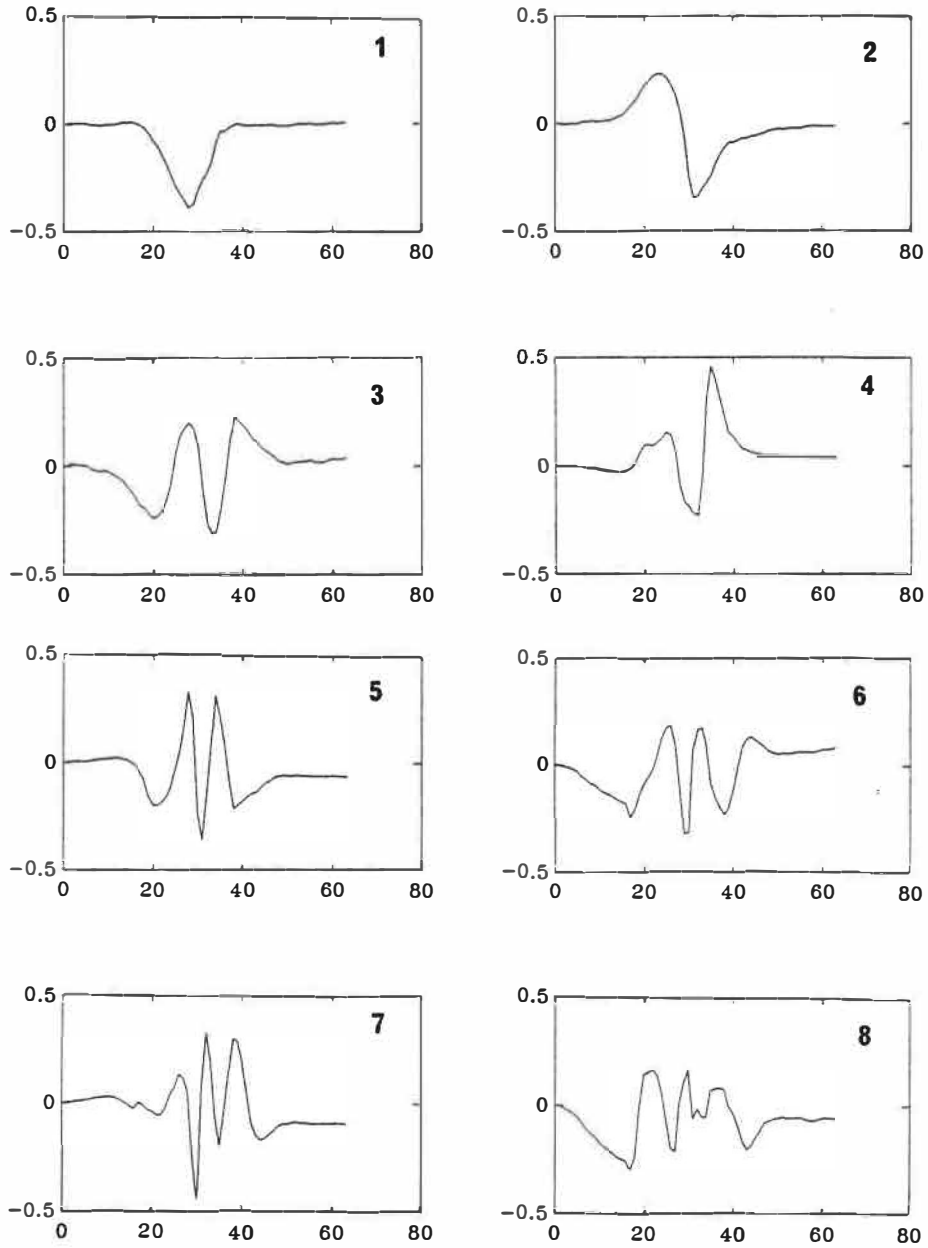

Figure 5.6: First 8 principal components in time, as produced by the SVD analysis of the epicardial potential matrix.

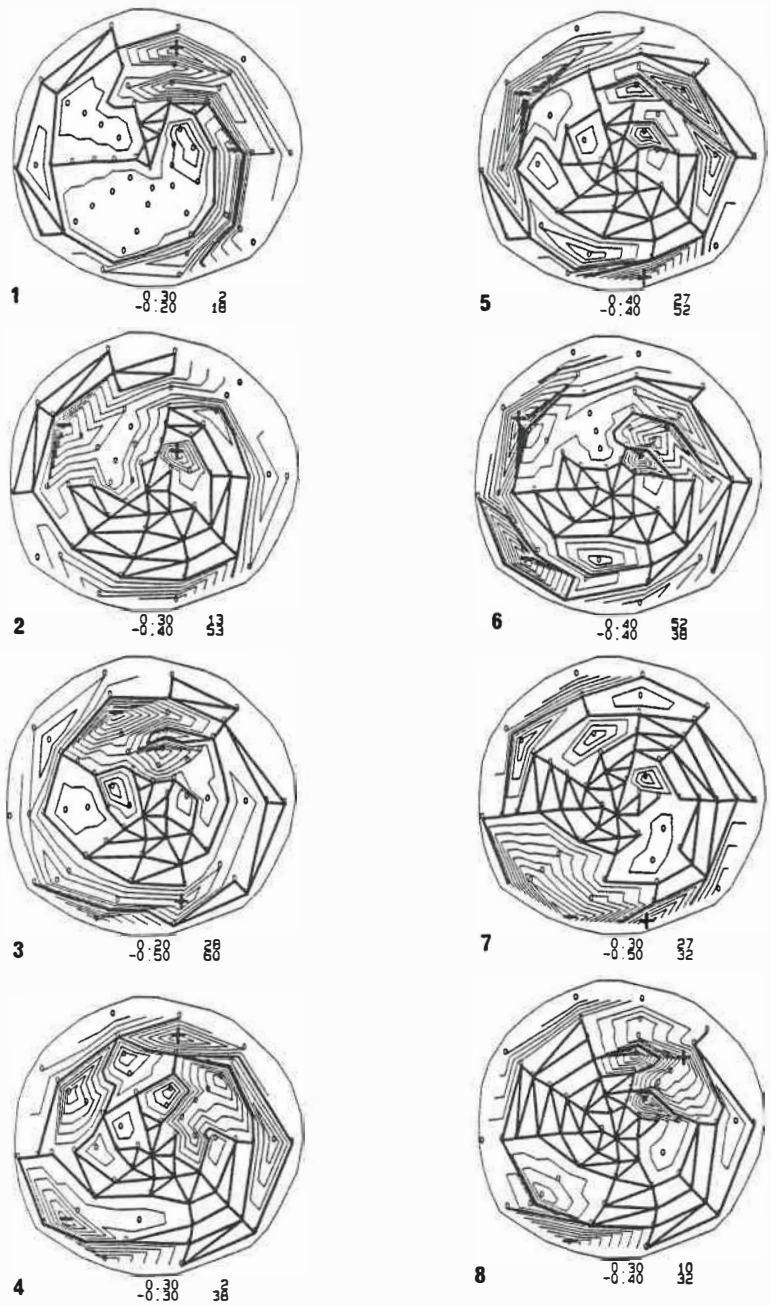

Figure 5.7: First 8 principal components in space, as produced by the SVD analysis of epicardial potential matrix. The maps are represented in a polar format as shown in Fig. 3.6. The thicker lines represent the zero lines.

InvSim-1:

$$\Phi_h(t_i, \xi_j) \xrightarrow{H} \hat{\Phi}_b(t_i, \xi_j) \xrightarrow{H^+} \hat{\Phi}_h(t_i, \xi_j). \tag{5.15}$$

The numerical solution of the forward problem was first performed to obtain the simulated body surface potentials, $\hat{\Phi}_b$, by using the potential values, Φ_h, measured at $\xi_j = 63$ leads located on the epicardium. The inverse epicardial potentials, $\hat{\Phi}_h$, were then computed by using the simulated body surface potentials, $\hat{\Phi}_b$, and then the measured epicardial potentials, Φ_h, were compared with the computed inverse epicardial potentials, $\hat{\Phi}_h$, at 63 leads on the heart surface.

The second set of inverse simulations is defined as *InvSim-2*:

$$\Phi_b(t_i, \xi_j) \xrightarrow{H^+} \hat{\Phi}_h(t_i, \xi_j) \xrightarrow{H} \hat{\Phi}_b(t_i, \xi_j). \tag{5.16}$$

The inverse epicardial potentials, $\hat{\Phi}_h$, were first computed by using the potential values , Φ_b, measured at $\xi_j = 63$ leads located on the torso of the WPW patient. The numerical solution of the forward problem was then performed to obtain the simulated body surface potentials, $\hat{\Phi}_b$, by using the inverse epicardial potentials, $\hat{\Phi}_h$, and then the measured body surface potentials, Φ_b, were compared with the simulated body surface potentials, $\hat{\Phi}_b$, at 63 leads on the thorax surface.

In both sets of inverse simulations, all six models were tested. The potential data comprised 70 time samples at 2 ms intervals after the onset of the QRS complex. Two inverse methods : (i) Tikhonov zero order (TikReg) and (ii) dimensionality control (DimCon), with their corresponding estimators, i.e., bounded norm constraint (BNC), optimal (OPT) and REsidual and Smooth Operator (CRESO) for TikReg method; BNC, OPT and Akaike information criterion (AIC) for DimCon, were involved. Details of the TikReg and DimCon inverse methods and the estimators BNC, OPT, CRESO and AIC are described in chapter 4. It is noted

that InvSim-1 and InvSim-2 do not encounter the errors due to the measurement of the potentials and the geometry of the torso.

Two measures of accuracy, were computed and analyzed and the results obtained are presented in this chapter. One measure is in time, comparing the electrograms, and the other is in space, comparing the surface maps at a given time instant.

5.6.1 Inverse simulation using the epicardial potentials (InvSim-1)

The error encountered between the measured and computed inverse epicardial potentials can be divided into two components,

$$\begin{aligned} \delta_{InvSim-1}(t_i, \xi_j) &= \Phi_h(t_i, \xi_j) - H^+(H\Phi_h(t_i, \xi_j)) \\ &= e^F_{InvSim-1} + e^I_{InvSim-1}, \end{aligned} \tag{5.17}$$

where $e^F_{InvSim-1}$ and $e^I_{InvSim-1}$ denote the errors affecting the epicardial potentials due to the forward simulation and the inverse calculation respectively.

Tables 5.1-5.3 provide a comparison between the performance of the inverse procedures in six different torso models, in terms of several measure of accuracy. In InvSim-1, the optimum value of the regularization parameter for the TikReg inverse method was found in the range from 10^{-8} to 2.4×10^{-8}, and the truncation level, n, for the DimCon method, with setting $\gamma = 10^{-8}$, varied between 54 and 63 for different inverse procedures and torso models.

Before discussing these results, a few examples of electrograms and maps obtained in InvSim-1 will be briefly presented. Fig. 5.8 presents the temporal behavior of the magnitude of the measured and computed inverse epicardial potentials

Table 5.1: Values of the $RMSD(t)$ of the epicardial potentials in InvSim-1 for six torso models and different inverse procedures.

Model	$RMSD^{\gamma}_{h,BNC}$	$RMSD^{\gamma}_{h,OPT}$	$RMSD^{\gamma}_{h,CRESO}$	$RMSD^{n,\gamma}_{h,BNC}$	$RMSD^{n,\gamma}_{h,OPT}$	$RMSD^{n,\gamma}_{h,AIC}$
T_1	643.8	502.7	700.9	842.2	295.2	380.5
LT_1	819.3	699.3	865.9	1227.6	327.7	392.0
$HLST_1$	848.3	677.0	861.7	965.4	272.4	374.9
T_2	866.6	866.6	885.7	198.4	153.0	327.6
LT_2	695.3	290.7	709.0	298.5	153.9	234.8
$HLST_2$	878.0	730.7	895.6	1274.6	225.4	291.4
Mean	791.9	627.8	819.8	801.1	237.9	333.5

Table 5.2: Values of the $RE(t)$ of the epicardial potentials in InvSim-1 for six torso models and different inverse methods.

Model	$RE^{\gamma}_{h,BNC}$	$RE^{\gamma}_{h,OPT}$	$RE^{\gamma}_{h,CRESO}$	$RE^{n,\gamma}_{h,BNC}$	$RE^{n,\gamma}_{h,OPT}$	$RE^{n,\gamma}_{h,AIC}$
T_1	0.279	0.228	0.296	0.393	0.120	0.149
LT_1	0.361	0.290	0.378	0.477	0.128	0.163
$HLST_1$	0.370	0.300	0.376	0.438	0.111	0.153
T_2	0.414	0.414	0.423	0.085	0.066	0.138
LT_2	0.310	0.130	0.317	0.148	0.074	0.119
$HLST_2$	0.420	0.335	0.429	0.522	0.083	0.105
Mean	0.359	0.283	0.370	0.344	0.097	0.138

Table 5.3: Values of the $CC(t)$ of the epicardial potentials in InvSim-1 for six torso models and different inverse methods.

Model	$CC^{\gamma}_{h,BNC}$	$CC^{\gamma}_{h,OPT}$	$CC^{\gamma}_{h,CRESO}$	$CC^{n,\gamma}_{h,BNC}$	$CC^{n,\gamma}_{h,OPT}$	$CC^{n,\gamma}_{h,AIC}$
T_1	0.949	0.965	0.944	0.893	0.990	0.984
LT_1	0.915	0.941	0.909	0.867	0.988	0.981
$HLST_1$	0.913	0.941	0.910	0.884	0.990	0.983
T_2	0.893	0.893	0.888	0.993	0.997	0.987
LT_2	0.938	0.985	0.936	0.978	0.996	0.990
$HLST_2$	0.889	0.924	0.884	0.848	0.995	0.991
Mean	0.916	0.942	0.912	0.911	0.993	0.986

for the $HLST_2$ model using the TikReg inverse method with the OPT estimator, which shows a peak amplitude at about 58 ms. Fig. 5.9 displays the epicardial maps as an instantaneous distribution of isopotential lines on the heart surface for the measured (left-side) and the inverse (right-side) epicardial potentials. Fig. 5.10 illustrates the measured and computed inverse electrograms at four electrode sites for the $HLST_1$ torso model and the DimCon inverse method with the AIC estimator. The locations of these four electrodes (3, 15, 27 and 44) are: right mid-lateral, antero-septal at the base, left-lateral-basal and postero-septal at the base, respectively.

Finally, table 5.4 presents the overall efficiency index of the different inverse procedures used in InvSim-1 for all six torso models. These results served as validation of the software implementation of the inverse methods utilized in this thesis.

In InvSim-1, the DimCon method exhibits better results in terms of $RMSD$, RE and CC, compared with the TikReg method for recovering the epicardial potentials under the condition of no signal noise (Tables 5.1-5.3). The mean values

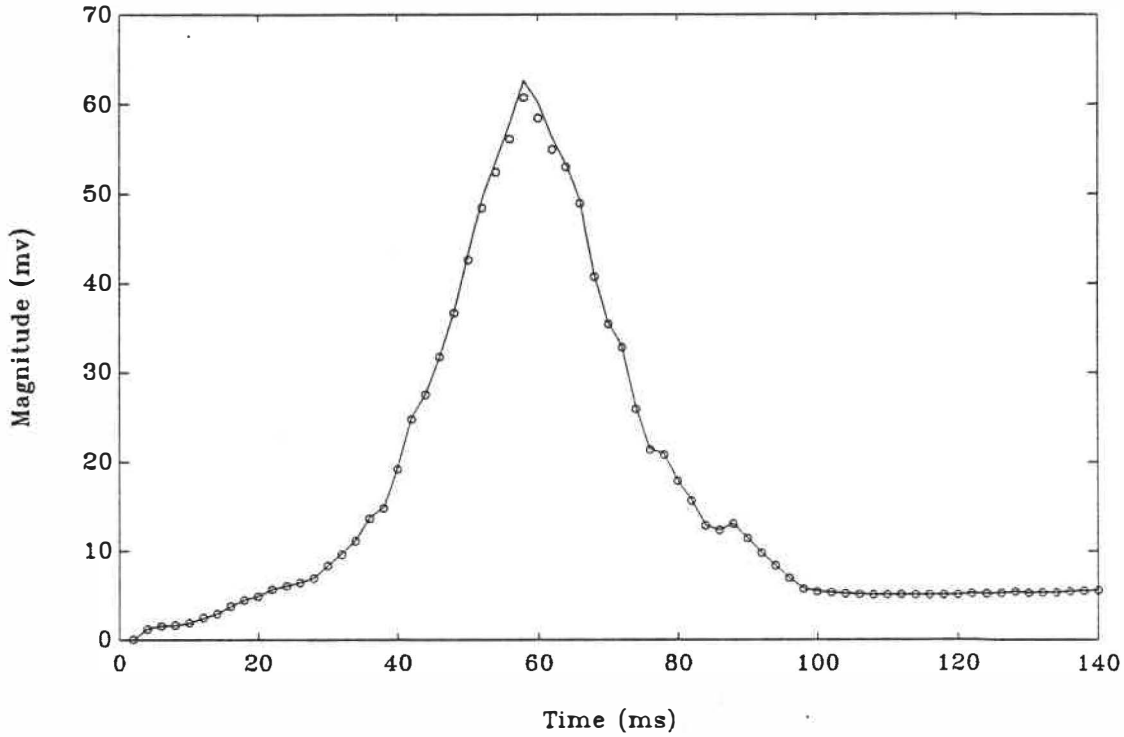

Figure 5.8: Time course of the magnitude for the 63 leads of the measured (–) and recovered (o) epicardial potentials in InvSim-1 for the $HLST_2$ model using the TikReg inverse method with the OPT estimator.

of $RMSD^{n,\gamma}_{h,OPT}$ ($RMSD^{\gamma}_{h,OPT}$), $RE^{n,\gamma}_{h,OPT}$ ($RE^{\gamma}_{h,OPT}$) and $CC^{n,\gamma}_{h,OPT}$ ($CC^{n,\gamma}_{h,OPT}$) obtained in InvSim-1 are 237.9 (627.8), 0.097 (0.283) and 0.993 (0.942), respectively.

Regarding the ability of the different estimators used in each of the two inverse methods, with no signal noise, BNC was found to be the least satisfactory, while the OPT and the $CRESO$ estimators for the TikReg method, and the OPT and AIC estimators for the DimCon method produced comparable results (Table 5.4). As expected, the OPT estimator in both inverse methods provides better results than the $CRESO$ and AIC estimators. The relative error found using the OPT estimator in TikReg method, $RE^{\gamma}_{h,OPT} = 0.283$, and in DimCon method,

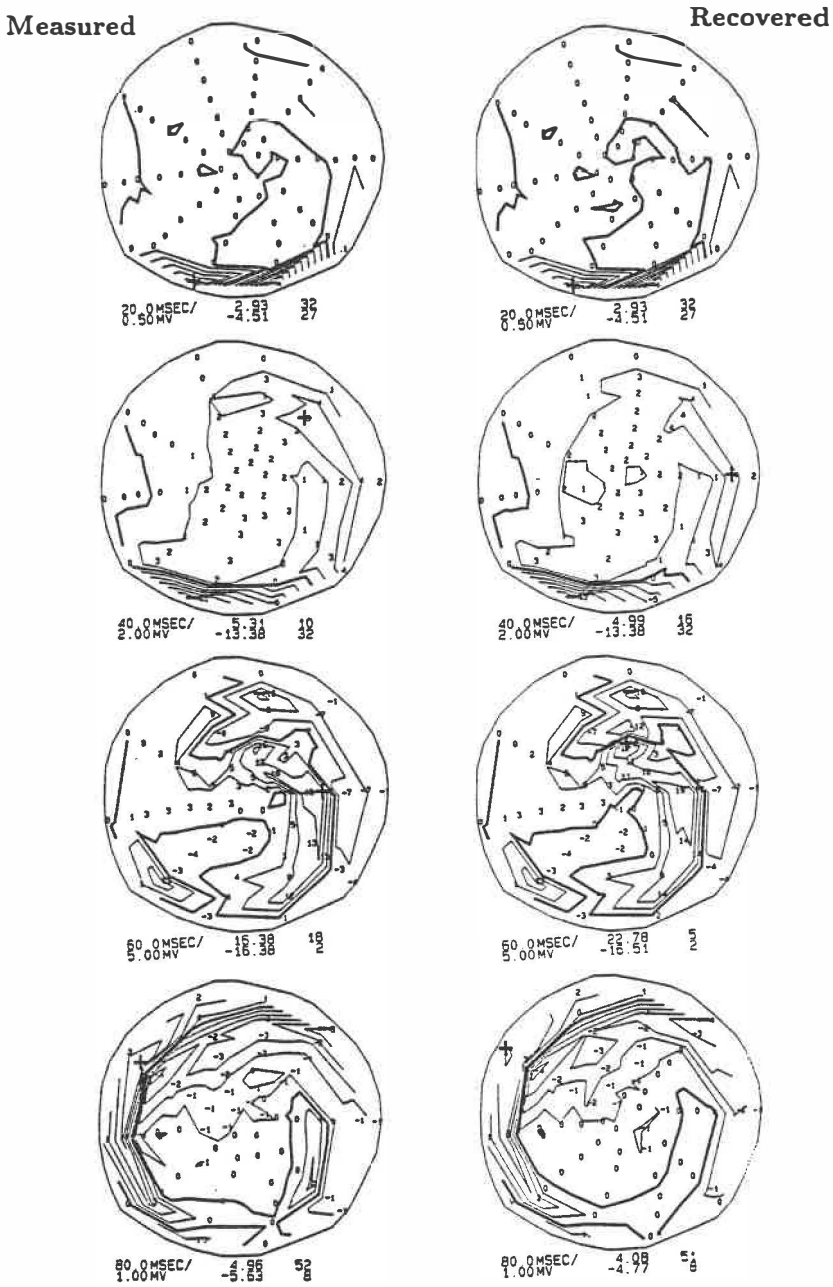

Figure 5.9: Isopotential lines representing the measured epicardial potentials (left-side) and those computed by solving the inverse problem in InvSim-1 (right-side). The maps are represented in a polar format introduced in Fig. 3.6.

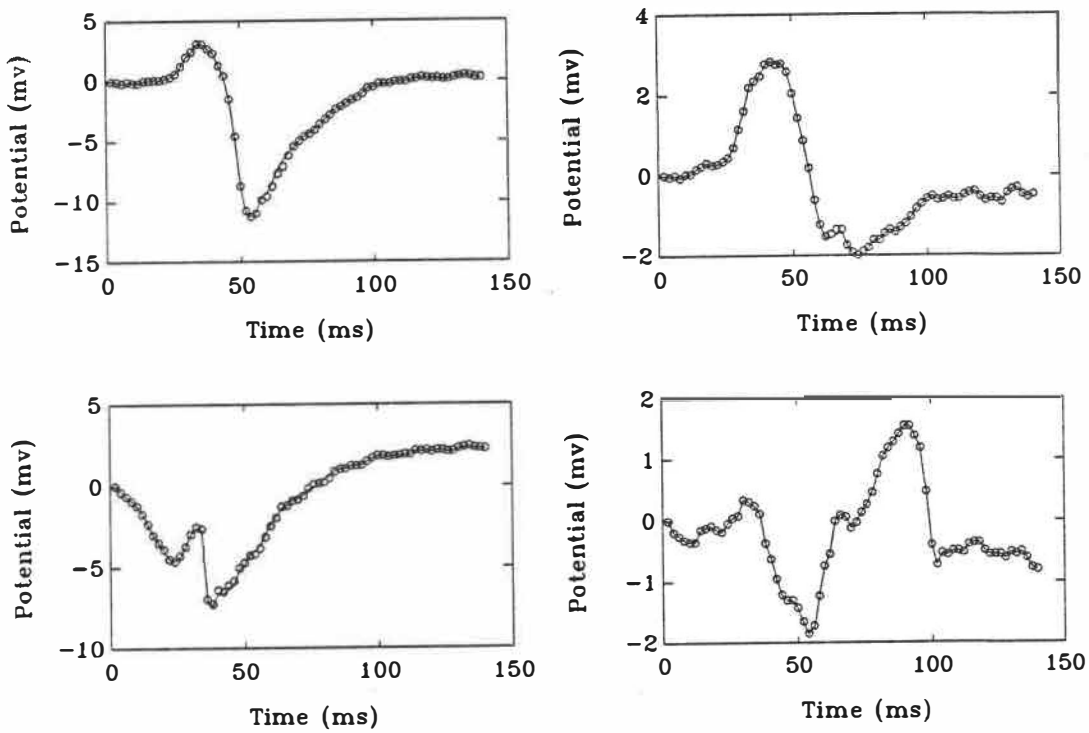

Figure 5.10: Comparison between the measured (–) and computed (o) electrograms at four different lead locations on the epicardium. Inverse simulation-1 was used; electrode sites were: left posterior (top-left); left anterior (top-right); right anterior (bottom-left) sites on the base; and (bottom-right) on the apex of the heart using the $HLST_1$ model with the DimCon inverse method.

Table 5.4: InvSim-1: comparison between the efficiency indices of the different inverse methods applied for the six torso models.

Efficiency Index	*TikReg*			*DimCon*		
	BNC	*OPT*	*CRESO*	*BNC*	*OPT*	*AIC*
IRMSD	1.26	1.00	1.31	1.28	0.38	0.53
IRE	1.27	1.00	1.31	1.22	0.34	0.49
ICC	0.972	1.000	0.968	0.967	1.054	1.047

$RE^{n,\gamma}_{h,OPT} = 0.097$, are lower than $RE^{\gamma}_{h,CRESO} = 0.370$ and $RE^{n,\gamma}_{h,AIC} = 0.138$, respectively.

These simulation results show that the *inclusion of the inhomogeneities in the torso model does not improve the accuracy of the recovered epicardial potentials.* This can be due to the increased sensitivity of the transfer matrix to its inversion process. This argument is supported when we compare the decay characteristics of the SVD values of the homogeneous versus inhomogeneous models, as shown in Fig. 5.3. The decay behavior of the SVD values is faster for the inhomogeneous models. Both the lungs and the spinal region have lower conductivity values than the rest of the thorax (Table 2.3). However, the inclusion of the spinal region does not substantially change the accuracy of the recovered potentials compared with the inclusion of the lungs at both mesh resolutions (Table 5.1-5.3).

Increasing the mesh resolution from 5517 to 12067 nodes in these FEM computer models improved the accuracy of the recovered distributions. For example, the average values of $RE^{n,\gamma}_{h,AIC}$ and $RE^{n,\gamma}_{h,OPT}$ are reduced from 0.155 to 0.121 and from 0.09 to 0.074. Similarly, the correlation coefficients were improved; $CC^{n,\gamma}_{h,AIC}$ and $CC^{n,\gamma}_{h,OPT}$ were increased from 0.983 and 0.989, to 0.989 and 0.995, respectively.

Table 5.5: Values of the $RMSD(t)$ for body surface potentials in InvSim-2 for six torso models.

Model	$RMSD^{\gamma}_{b,BNC}$	$RMSD^{\gamma}_{b,OPT}$	$RMSD^{n,\gamma}_{b,BNC}$	$RMSD^{n,\gamma}_{b,OPT}$	$RMSD^{n,\gamma}_{b,AIC}$
T_1	7.038	0.410	1.966	0.409	0.411
LT_1	9.968	0.509	2.136	0.391	0.391
$HLST_1$	4.456	0.329	0.987	0.329	0.329
T_2	15.558	15.558	1.959	0.463	0.464
LT_2	2.941	0.254	0.543	0.254	0.254
$HLST_2$	7.030	0.064	0.833	0.064	0.064
Mean	7.832	2.854	1.638	0.318	0.319

5.6.2 Inverse simulations using the torso potentials (InvSim-2)

The errors encountered in InvSim-2 between the measured and simulated body surface potentials can be divided into two components

$$\begin{aligned} \delta_{InvSim-2}(t_i, \xi_j) &= \Phi_b(t_i, \xi_j) - H(H^+\Phi_b(t_i, \xi_j)) \\ &= e^I_{InvSim-2} + e^F_{InvSim-2}, \end{aligned} \tag{5.18}$$

where $e^I_{InvSim-2}$ and $e^F_{InvSim-2}$ denote the errors affecting the torso potentials due to the inverse calculation and the forward simulation, respectively.

Tables 5.5, 5.6 and 5.7 report the average accuracy criteria $RMSD(t)$, $RE(t)$ and $CC(t)$, which were obtained by comparing the measured and the simulated torso maps for all time instants. In InvSim-2, the optimum value of the regularization parameter for TikReg inverse method was found in the range $10^{-8} - 1.8 \times 10^{-8}$, and the truncation level, n, for the DimCon method with setting $\gamma = 10^{-8}$ varied between 58 and 63 for the different inverse procedures used for all torso models.

Fig. 5.11 presents the temporal behavior of the magnitude of the measured

Table 5.6: Values of the $RE(t)$ for the body surface potentials in InvSim-2 for six torso models.

Model	$RE^{\gamma}_{b,BNC}$	$RE^{\gamma}_{b,OPT}$	$RE^{n,\gamma}_{b,BNC}$	$RE^{n,\gamma}_{b,OPT}$	$RE^{n,\gamma}_{b,AIC}$
T_1	0.0325	0.0044	0.0096	0.0044	0.0045
LT_1	0.0492	0.0035	0.0107	0.0031	0.0031
$HLST_1$	0.0647	0.0017	0.0136	0.0017	0.0017
T_2	0.1156	0.1156	0.0130	0.0047	0.0047
LT_2	0.0429	0.0015	0.0057	0.0015	0.0015
$HLST_2$	0.0805	0.0046	0.0103	0.0005	0.0005
Mean	0.0642	0.0219	0.0105	0.0027	0.0027

Table 5.7: Values of the $CC(t)$ for the body surface potentials in InvSim-2 for six torso models.

Model	$CC^{\gamma}_{b,BNC}$	$CC^{\gamma}_{b,OPT}$	$CC^{n,\gamma}_{b,BNC}$	$CC^{n,\gamma}_{b,OPT}$	$CC^{n,\gamma}_{b,AIC}$
T_1	0.9988	0.999977	0.999912	0.999977	0.999975
LT_1	0.9969	0.999990	0.999856	0.999992	0.999991
$HLST_1$	0.9949	0.999998	0.999749	0.999998	0.999998
T_2	0.9903	0.990246	0.999852	0.999968	0.999968
LT_2	0.9973	0.999998	0.999620	0.999998	0.999998
$HLST_2$	0.9927	1.000000	0.999841	1.000000	1.000000
Mean	0.9952	0.998368	0.999805	0.999989	0.999989

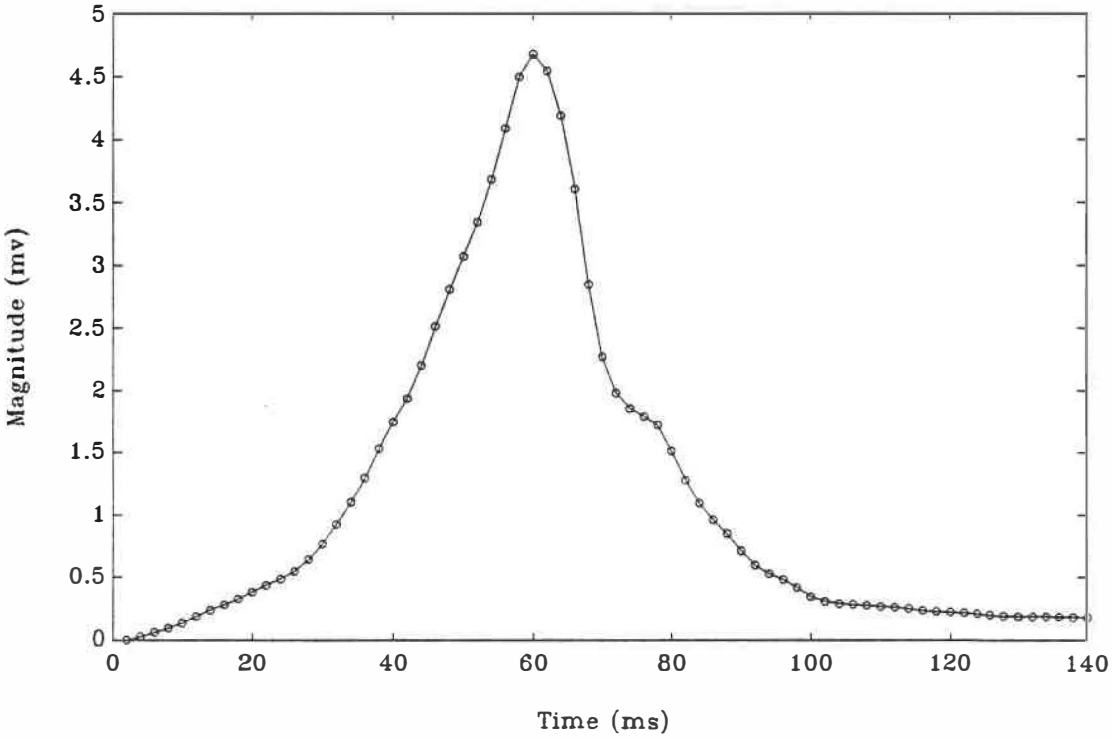

Figure 5.11: Time course of the magnitude of the measured (–) and recovered (o) potentials in inverse simulation-2 for the $HLST_2$ model using the TikReg inverse method with the OPT estimator.

and the simulated body surface potentials, which shows a peak amplitude corresponding to that of the QRS complex. Fig. 5.12 displays the torso maps as an instantaneous distribution of isopotential lines on the torso surface for the measured (left-side) and the simulated (right-side) body surface potentials. Simulated maps were obtained using the computed inverse data, for 70 successive instants at 2 ms intervals during the QRS interval.

Table 5.8 presents the overall efficiency index of the different inverse procedures used in InvSim-2 for all six torso models. The inverse simulation results obtained from InvSim-2 confirm the satisfactory implementation of the procedures. In

Measured **Simulated**

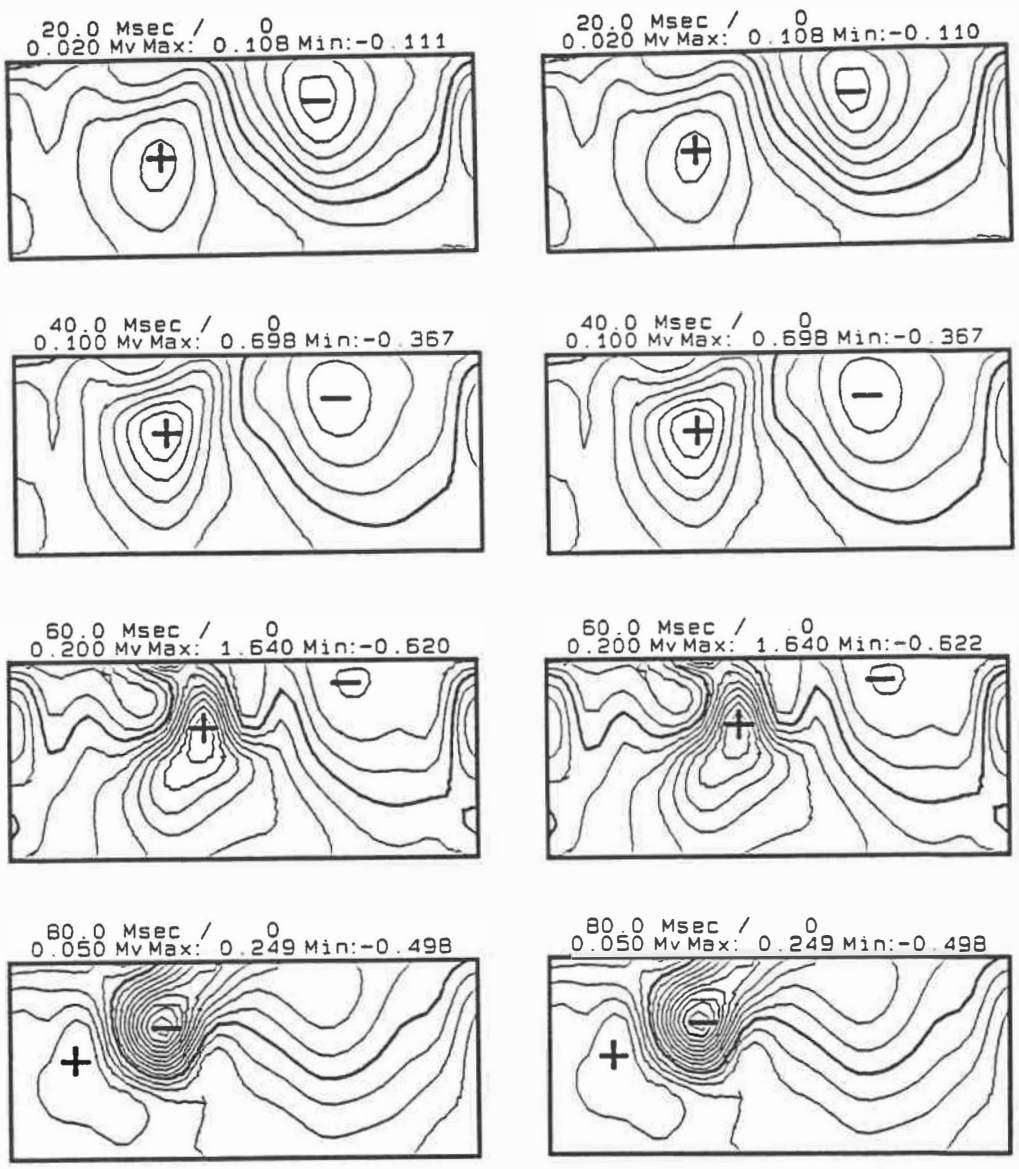

Figure 5.12: Isopotential lines representing the measured thoracic potentials (left-side) and those computed by the inverse simulation-2 procedure (right-side). The maps are represented in a rectangular format with the anterior torso on the left and posterior torso on the right of each map.

Table 5.8: InvSim-2: comparison between the efficiency indices of the different inverse-forward procedures applied in six torso models.

Efficiency Index	*TikReg*		*DimCon*		
	BNC	*OPT*	*BNC*	*OPT*	*AIC*
IRMSD	2.74	1.00	0.57	0.11	0.11
IRE	2.93	1.00	0.48	0.12	0.12
ICC	0.9968	1.0000	1.0014	1.0016	1.0016

InvSim-2, the DimCon method gives slightly better results, in terms of $RMSD$, RE and CC, compared with the TikReg method (Tables 5.5-5.7) under conditions of no signal noise. The mean values of $RMSD^{n,\gamma}_{b,OPT}$ ($RMSD^{\gamma}_{b,OPT}$), $RE^{n,\gamma}_{b,OPT}$ ($RE^{\gamma}_{b,OPT}$) and $CC^{n,\gamma}_{b,OPT}$ ($CC^{\gamma}_{b,OPT}$) obtained in InvSim-1 are 0.318 (2.854), 0.0027 (0.0219) and 0.999989 (0.998368), respectively.

Regarding the ability of the different estimators used in each of the two inverse methods, the BNC estimator was found to be the least satisfactory, while the OPT estimator for the TikReg method, the OPT and AIC estimators for the DimCon method, produced comparable results (Table 5.8). The OPT and AIC estimators used in the DimCon inverse method produced identical results, while the OPT estimator shows superiority over the BNC estimator used in the TikReg method (Table 5.5-5.8). The relative error found using the OPT estimator in the TikReg method, $RE^{\gamma}_{b,OPT} = 0.0219$, is higher than $RE^{n,\gamma}_{b,OPT} = 0.0027$ and $RE^{n,\gamma}_{b,AIC} = 0.0027$ in the DimCon method. The results suggest that the overall constraint imposed by the OPT and AIC estimators in the DimCon method gives identical potential recovery as the BNC estimator.

These results show that the error encountered in InvSim-1 was not the same as in InvSim-2; the accuracy of the recovered potential distributions in InvSim-2 was

higher than in InvSim-1, i.e., $\delta_{InvSim-1} > \delta_{InvSim-2}$. This is evidenced by higher $RMSD$, higher RE and lower CC in InvSim-1 compared with $RMSD$, RE and CC obtained in InvSim-2, (Tables 5.1-5.3 and 5.5-5.7). Further, the differences between InvSim-1 and InvSim-2 are also demonstrated in Figs. 5.8 and 5.11. The recovered magnitude in InvSim-1 (Fig. 5.8) is underestimated compared with that of the InvSim-2 (Fig. 5.11).

The range of the optimum regularization parameter required in the inverse procedures was lower in the InvSim-2 compared with InvSim-1. The range of the truncation level involved in InvSim-2 was also lower than the truncation level required in InvSim-1. These results suggest that the amount of regularization or truncation required in InvSim-1 is higher than needed in InvSim-2.

In InvSim-1, while the first operation is the forward simulation, $\Phi_h(t_i, \xi_j) \xrightarrow{H} \hat{\Phi}_b(t_i, \xi_j)$, the second operation is the inverse solution, $\hat{\Phi}_b(t_i, \xi_j) \xrightarrow{H^+} \hat{\Phi}_h(t_i, \xi_j)$. The latter operation magnifies any perturbation which may have occurred in the simulated body surface potentials by the matrix condition number (presently is 10^8. On the other hand, in the InvSim-2 the first operation is the inverse recovery, $\Phi_b(t_i, \xi_j) \xrightarrow{H^+} \hat{\Phi}_h(t_i, \xi_j)$, and unlike InvSim-1, the body surface potentials do not contain any errors. This may account for the difference between the two types of inverse simulations.

In summary, the operations involved in InvSim-1 and InvSim-2 are not reversible. However, the results of either simulation validate the software implementation of the different inverse procedures.

Chapter 6

The inverse problem: validation with measured epicardial potentials

In this chapter, inverse solution results are presented and analyzed. The following points are covered: (i) quantitative error analysis of the recovered epicardial potentials in terms of relative errors and correlation coefficients, (ii) qualitative error analysis in terms of epicardial maps and electrograms which are visually compared with the measured ones, (iii) evaluation of the performances of the TikReg and DimCon inverse methods, (iv) comparison of the estimators used in each inverse method, (v) evaluation of the effects of torso inhomogeneities, (vi) evaluation of the effects of mesh resolution on the recovered potential distributions, and (vii) comparative performance analysis of spatial and temporal inverse solutions. All computations were performed in double precision on an IRIS 4D/280S (Power Series system with 8 parallel processors).

6.1 Spatial inverse solutions

Inverse epicardial distributions were calculated from the measured body surface maps using six inverse procedures, at all 70 time instants, during the QRS complex. Two inverse methods, TikReg and DimCon, along with different techniques to find the optimal value of the regularization parameter, $\gamma^{TikReg}(t_i)$, or the truncation level with a given regularization value, $n^{DimCon}(t_i)$, were applied.

6.1.1 Regularization

A survey of the spatial inverse solutions based on TikReg method is summarized in Table 6.1. Column 1 shows the volume conductor model; column 2 specifies the estimator; columns 3-6 give the values of corresponding accuracy criteria in terms of RE_h, CC_h, $\| \hat{\Phi}_b \| / \| \Phi_b \|$ and $RMSD_b$ which were averaged for all time instants; column 7 presents the average optimal value of the regularization parameter for the TikReg method.

6.1.2 Control of dimensionality

A survey of the spatial inverse solutions based on the DimCon method is summarized in Table 6.2. Columns 1 through 6 show the same information as Table 6.1, and column 7 presents the average optimal value of the truncation level for the DimCon method for a given $\gamma^{DimCon} = 10^{-3}$.

Table 6.3 summerizes the average values of the truncation level and the accuracy criteria obtained with the DimCon method for different time intervals during the QRS complex. The first interval ($0 - 40ms$) represents the ventricular pre-excitation, which is characterized by a small and well-localized wavefront (*delta wave*). The second interval ($40 - 100ms$) is characterized by a more complex ac-

Table 6.1: Quantitative results obtained with the TikReg method. Average values for all time instants of the optimal regularization parameter and the accuracy criteria of the recovered epicardial maps obtained by applying the TikReg method using the BNC, OPT and CRESO estimators for all six torso models.

Model	*Estimator*	RE_h	CC_h	$\| \hat{\Phi}_b \| / \| \Phi_b \|$	$RMSD_b$	$\gamma^{TikReg}(10^{-3})$
T_1	BNC	1.305	0.261	0.976	23.4	0.042
LT_1		1.314	0.195	0.945	48.5	0.178
$HLST_1$		1.309	0.202	0.950	49.7	0.177
T_2		1.289	0.127	0.935	52.3	0.237
LT_2		1.282	0.191	0.970	40.0	0.316
$HLST_2$		1.285	0.135	0.930	52.6	0.316
T_1	OPT	0.982	0.210	0.809	78.7	23.71
LT_1		0.985	0.177	0.721	101.5	42.17
$HLST_1$		0.984	0.176	0.729	99.9	42.17
T_2		0.977	0.182	0.673	112.6	42.16
LT_2		0.975	0.201	0.729	96.8	31.62
$HLST_2$		0.974	0.189	0.668	113.4	42.17
T_1	CRESO	1.626	0.252	0.950	42.2	0.18
LT_1		1.227	0.220	0.889	60.8	0.04
$HLST_1$		1.723	0.212	0.884	62.3	0.10
T_2		1.489	0.184	0.884	63.1	0.24
LT_2		1.172	0.184	0.980	27.4	0.01
$HLST_2$		1.660	0.192	0.879	64.2	0.24

tivity with multiple wavefronts resulting from the *fusion* between the pre-excition and the normally conducted activity.

6.1.3 Recovered maps

Fig. 6.1 shows the sequence of epicardial potential distributions at $10ms$ intervals during the QRS complex. Two distinct phases can be observed in these maps: the pre-excitation phase which occurs between $10 - 40ms$ and the fusion phase

Table 6.2: Quantitative results obtained with the DimCon method. Average values for all time instants of the optimal truncation level and the accuracy criteria of the recovered epicardial maps obtained by applying the DimCon method using the BNC, OPT and AIC estimators for all six torso models.

Model	*Estimator*	RE_h	CC_h	$\parallel \hat{\Phi}_b \parallel / \parallel \Phi_b \parallel$	$RMSD_b$	n^{DimCon}
T_1	BNC	1.039	0.211	0.940	48.6	63
LT_1		1.069	0.130	0.905	61.9	63
$HLST_1$		1.066	0.133	0.904	62.6	63
T_2		1.089	0.150	0.879	66.4	63
LT_2		1.047	0.152	0.920	52.7	63
$HLST_2$		1.092	0.159	0.874	67.0	63
T_1	OPT	0.970	0.287	0.814	101.2	9
LT_1		0.972	0.209	0.749	122.7	3
$HLST_1$		0.972	0.214	0.754	121.8	3
T_2		0.967	0.223	0.734	127.4	2
LT_2		0.965	0.303	0.769	114.9	5
$HLST_2$		0.965	0.230	0.731	128.0	2
T_1	AIC	1.041	0.169	0.935	55.5	13
LT_1		1.061	0.127	0.905	67.9	9
$HLST_1$		1.060	0.128	0.901	68.7	9
T_2		1.090	0.156	0.877	69.8	8
LT_2		1.040	0.129	0.915	58.6	10
$HLST_2$		1.091	0.166	0.873	70.3	8

which occurs between $50 - 100ms$. The pre-excitation phase is characterized by a well-localized left-lateral minimum which reflects the ventricular insertion point of the atrio-ventricular accessory pathway, whereas the fusion phase presents more complex patterns with multiple wavefronts. The location of the pre-excitation was confirmed by the surgon who made the ablation disappeared. Two time instants, one at $20ms$ and the other at $50ms$ are considered as test problems for the evaluation of the recovered epicardial potential maps by the different models

Table 6.3: Average values of the optimal truncation level and the accuracy criteria obtained by applying the DimCon method and the $HLST_2$ model for the recovered epicardial maps in the time intervals $0 - 40ms$ and $40 - 100ms$.

Time (ms)	*Estimator*	RE_h	CC_h	$\| \hat{\Phi}_b \| / \| \Phi_b \|$	$RMSD_b$	n^{DimCon}
$0 - 40$	BNC	1.092	0.156	0.871	28.6	63
$40 - 100$		1.087	0.168	0.872	93.2	63
$0 - 40$	OPT	0.977	0.123	0.738	53.1	3
$40 - 100$		0.955	0.308	0.732	177.9	2
$0 - 40$	AIC	1.080	0.149	0.865	29.9	8
$40 - 100$		1.093	0.183	0.872	97.7	9

and different inverse methods. The recovered maps from the DimCon method presented in this subsection are obtained with $\gamma^{DimCon} = 10^{-6}$.

Fig. 6.2 shows the recovered epicardial maps, using the T_1 model and the measured map at $20ms$. Similarly, Figs. 6.3 and 6.4 show the recovered epicardial potential distributions obtained using the $HLST_1$ and $HLST_2$ models, respectively, at $20ms$. Figs. 6.5-6.7 compare the recovered maps with the measured map at $50ms$ for the T_1, $HLST_1$ and $HLST_2$ models, respectively. The format of these figures is the same as in Fig. 6.2.

6.1.4 Evaluation of the results

Tables 6.1-6.3 reveal that errors are large for all inverse methods. In such a circumstance, it is difficult to compare the relative merits of the different inverse methods; most likely, there are systematic sources of error in the measured epicardial potential distributions. Two possible sources of errors can be identified. The first one is the possible mismatch between the location of the actual epicardial measurement electrodes and the lead locations of the computer model, since the

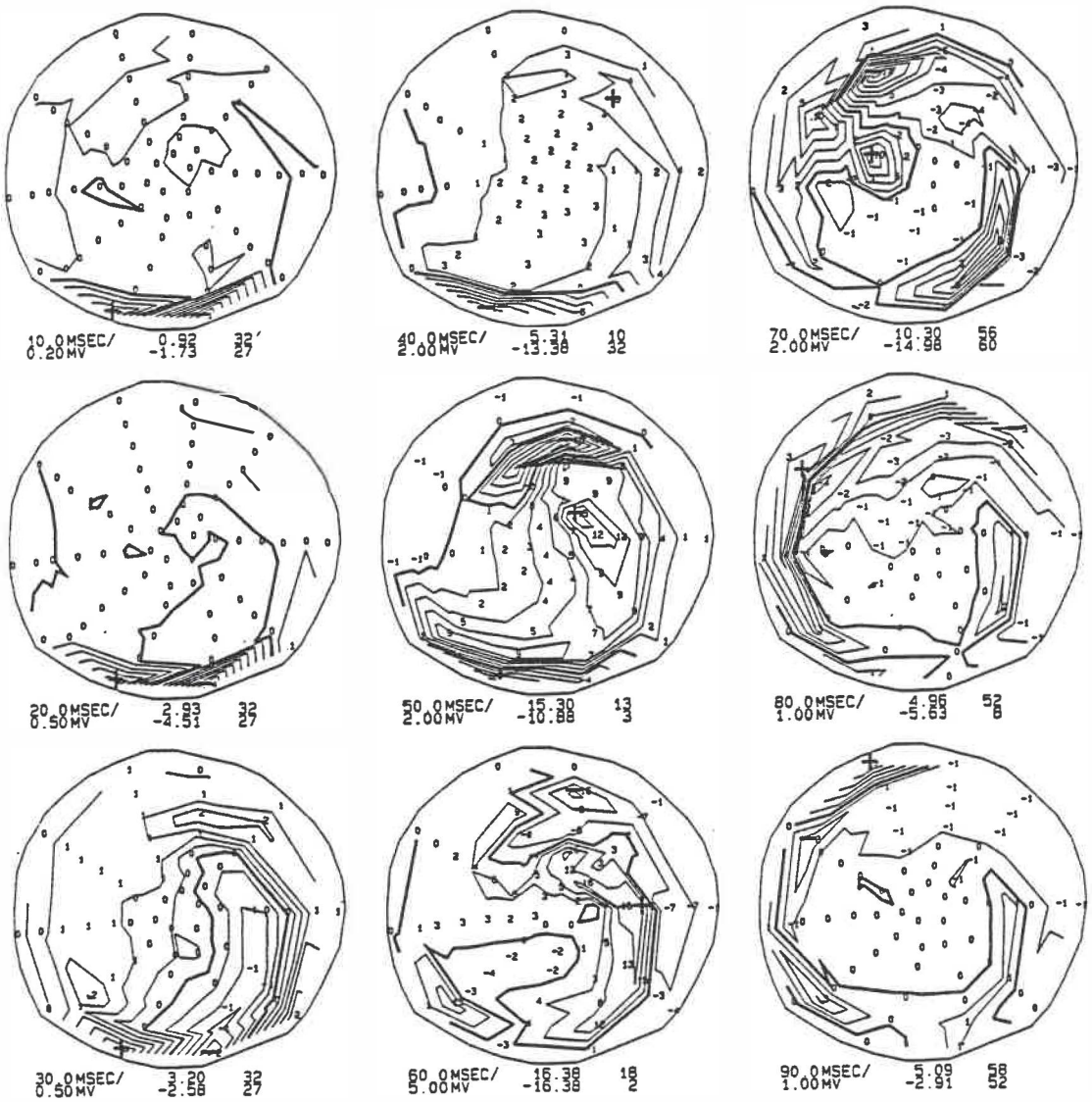

Figure 6.1: Epicardial maps drawn at every $10ms$ during the QRS complex for the patient with WPW syndrome. Maps are drawn in a polar format, with the apex at the center and the base on the circumference. The right ventricle (RV) corresponds to the upper half of the maps and the left ventricle (LV) to the lower half. The interval between isopotential lines is indicated in the lower left corner of each map. The values of the maximum and minimum are indicated under each map (in mv).

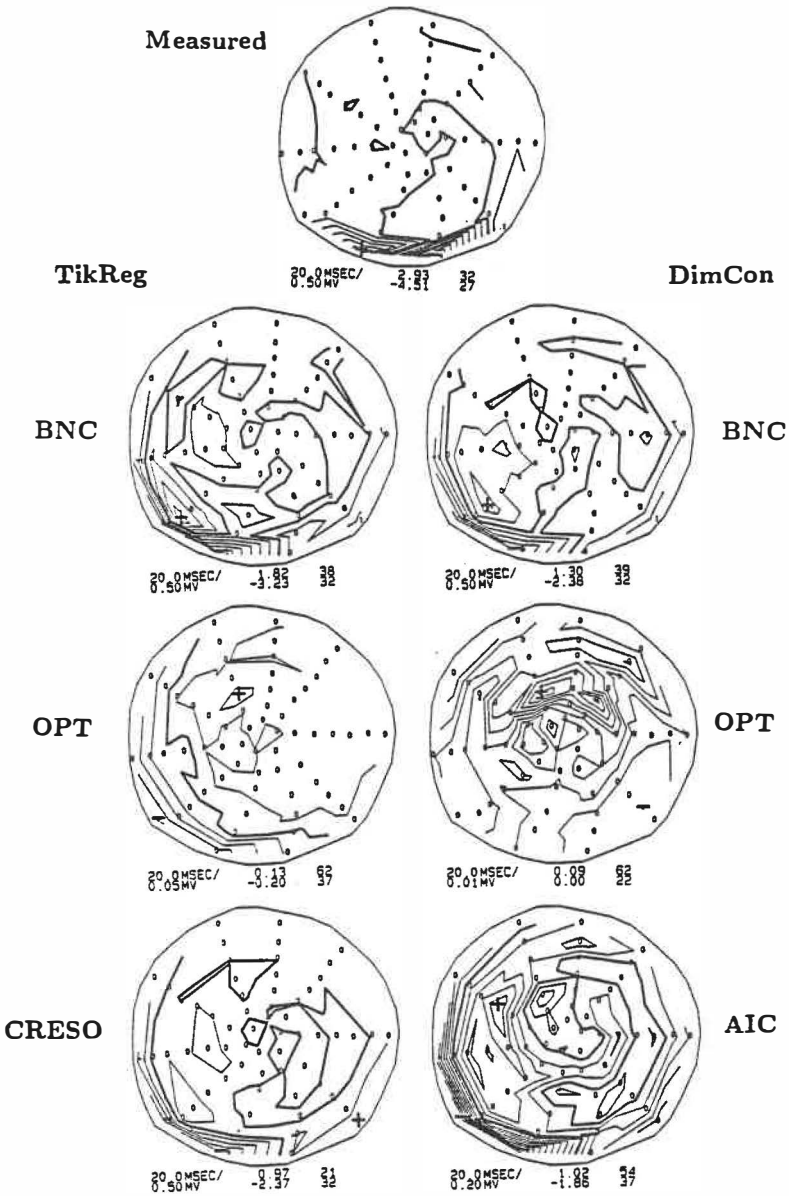

Figure 6.2: Comparison between the measured (top) and inverse epicardial maps at $20ms$ (left- and right-side). The computed maps were recovered using the T_1 model. The map on the top is the measured one, the maps on the left are those obtained using the TikReg inverse method and the maps on the right are those obtained using DimCon with their corresponding estimators.

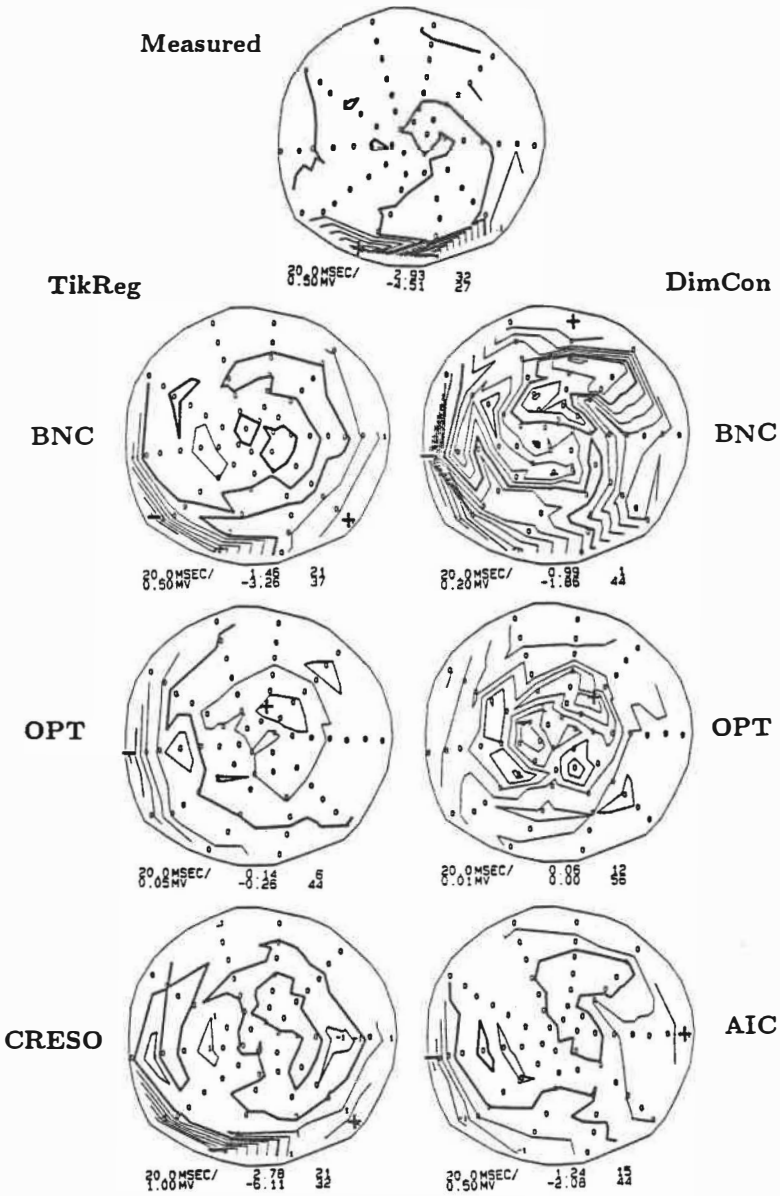

Figure 6.3: Comparison between the measured (top) and inverse epicardial maps at $20ms$ (left- and right-side). The computed maps were recovered using the $HLST_1$ model.

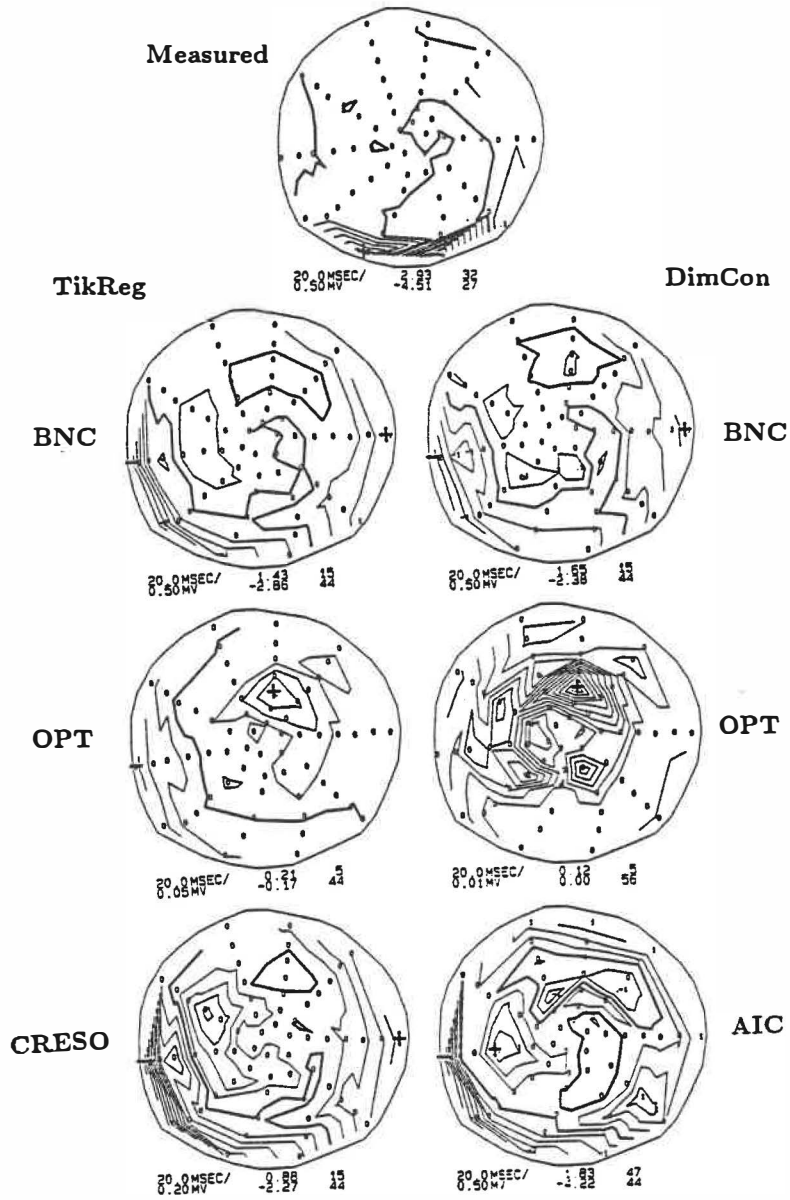

Figure 6.4: Comparison between the measured (top) and inverse epicardial maps at $20ms$ (left- and right-side). The computed maps were recovered using the $HLST_2$ model.

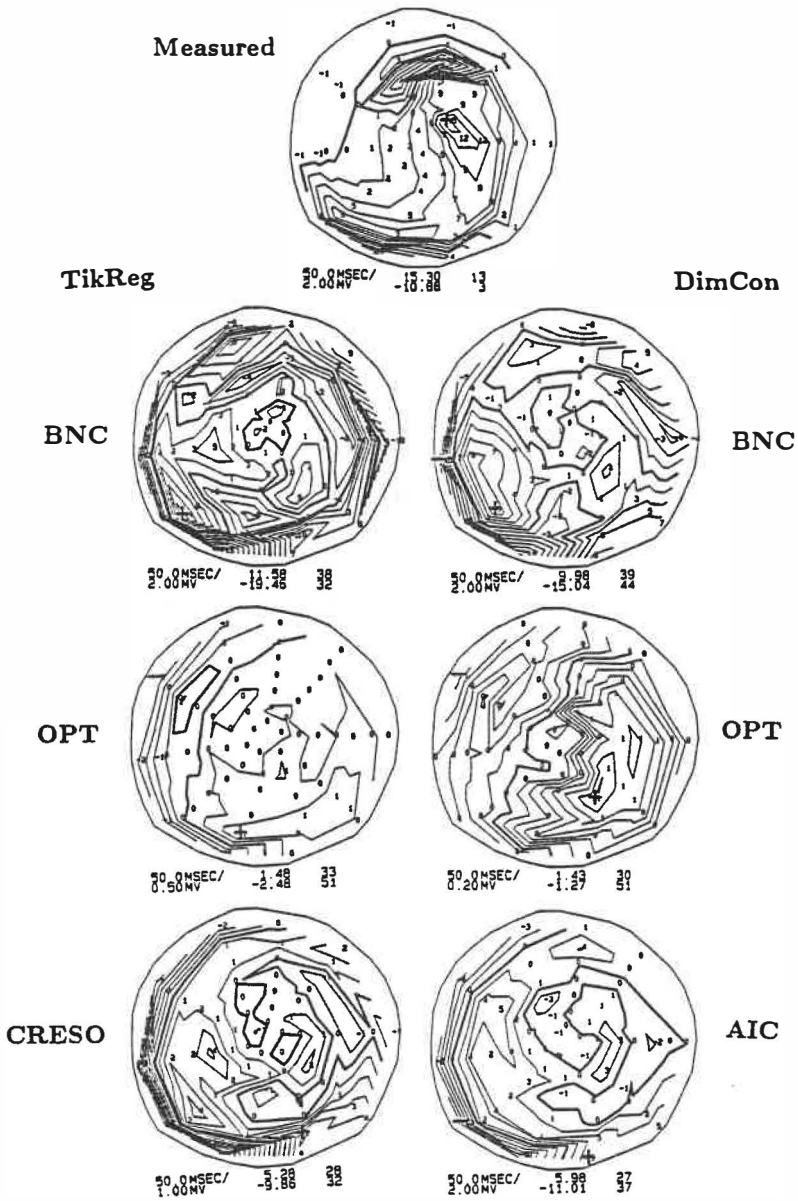

Figure 6.5: Comparison between the measured (top) and inverse epicardial maps at $50ms$ (left- and right-side). The computed maps were recovered using the T_1 model.

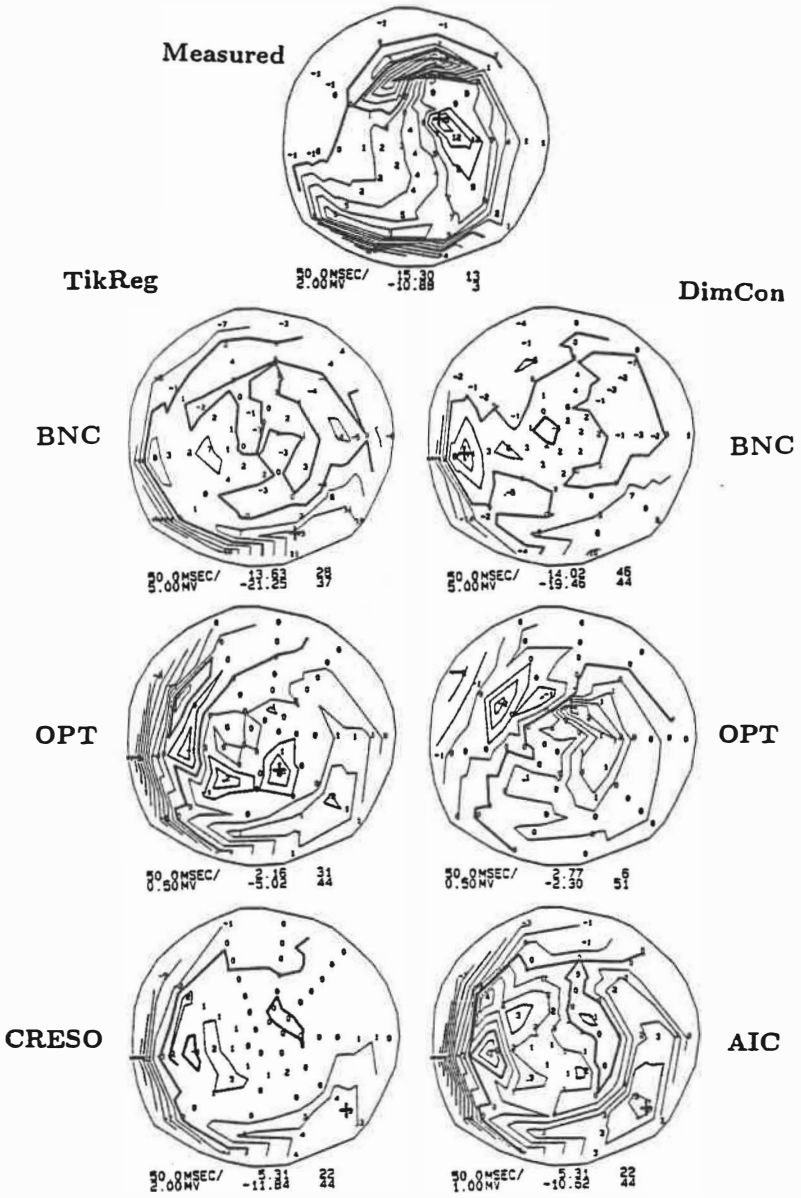

Figure 6.6: Comparison between the measured (top) and inverse epicardial maps at $50ms$ (left- and right-side). The computed maps were recovered using the $HLST_1$ model.

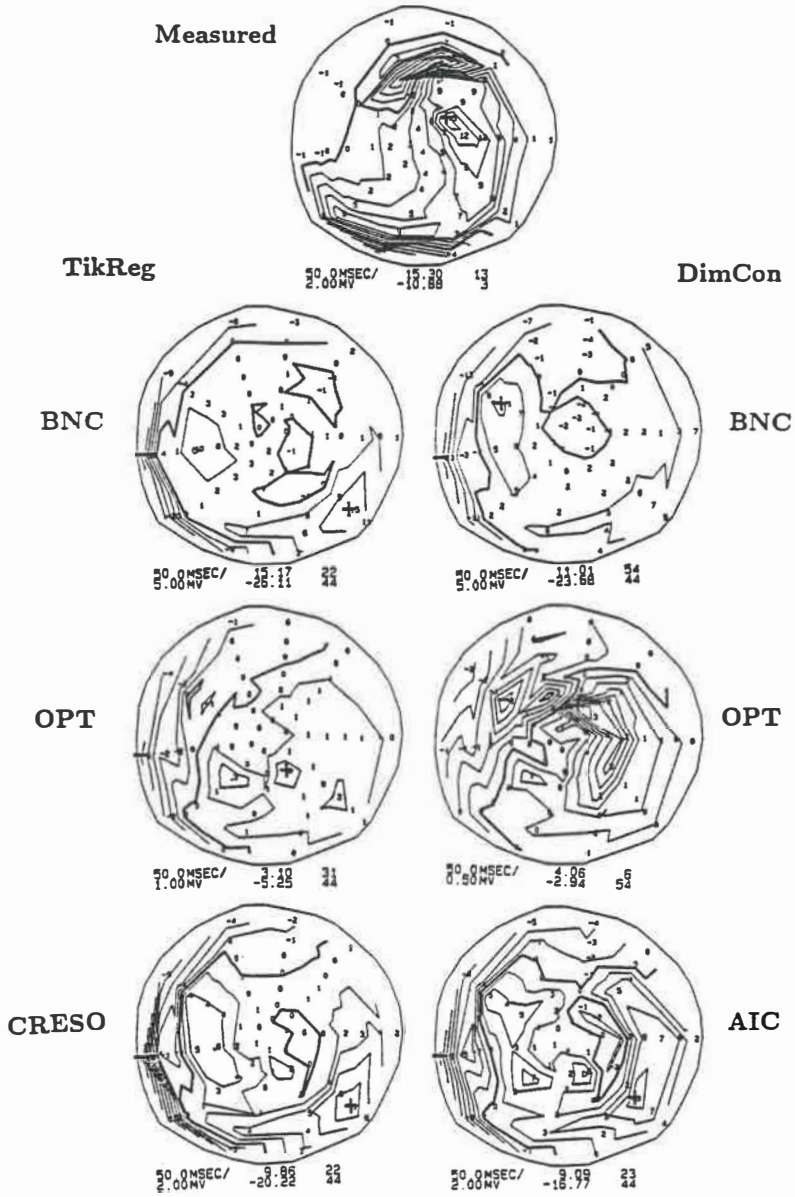

Figure 6.7: Comparison between the measured (top) and inverse epicardial maps at $50ms$ (left- and right-side). The computed maps were recovered using the $HLST_2$ model.

lead locations were measured only indirectly by placing the sock electrode array over a cardboard model of the heart. A rotation of the electrode array seems to have been introduced during this measurement, since most of the inverse epicardial maps (BNC and CRESO on Fig. 6.2) show the typical pre-excitation pattern, but with a clock-wise rotation with respect to the measured epicardial maps. The forward simulation results presented in Appendix D confirm this interpretation. These inverse maps reproduce quite well the overall pattern of the measured map with close extrema near the base of the lateral wall of the left ventricle; however, they produce large relative errors and low correlation coefficients because the minimum on the inverse maps corresponds to the maximum on the measured map. The other source of error is related to the epicardial potential measurements at electrode sites that are exposed to air during open heart surgery. Electrodes exposed to air give higher potential values than in the closed chest, because of the altered extracardiac volume-conductor properties. However, the activation sequence is not changed by the exposure to air and the distribution of positive and negative potentials remains the same; this still allows visual comparison between the inverse and measured isopotential maps. Therefore, the quantitative criteria presented in Tables 6.1-6.3 tend to give a more pessimistic picture of the performance of the different inverse methods than what the real performance seems to be.

Visual interpretation of inverse maps was thus used as an alternative approach for the evaluation of the results. As seen in Fig. 6.2, the pre-excitation can be localized with the BNC and CRESO estimators with reasonable accuracy. The locations of the extrema obtained with these estimators are shifted by one inner-electrode distance (about 2 cm) compared with those of the measured ones. Thus,

clinical information can be gained from these results. Another observation that can be made from the inverse maps is the smearing of the extrema.

It is clear from Fig. 6.2 that the choice of the estimator has a more pronounced effect on the inverse solution than the choice of the inverse method. This is because the final criteria for any inverse method depend on the bound set by the estimator. The narrower the imposed bound set on the solution space, the more underestimation can occur in the inverse solution. A good example is the OPT estimator. It provides the best quantitative results (Tables 6.1-6.3), as expected, but it also gives the worse recovered maps (Fig. 6.2). The maps recovered with the OPT estimator are the smoothest compared with the other estimators (regularization levels were the highest) and they do not provide any clinically useful information. Finally, the best results were obtained with the BNC or CRESO estimators. The AIC estimator gave moderately good results.

By visual inspection, the inverse maps obtained with the inhomogeneous $HLST_1$ model (Fig. 6.3) are worse than those obtained with the homogeneous T_1 (Fig. 6.2), with the exception of the maps obtained with the CRESO estimator. For example, the extrema on the maps obtained with the BNC estimator are further apart than those observed on Fig. 6.2, and these maps give erroneous clinical information. This suggests that the conductivity values might have been wrongly chosen.

As the mesh resolution increases, the inverse maps obtained with the higher resolution $HLST_2$ model (Fig. 6.4) deteriorate compared with those obtained with the lower resolution $HLST_1$ (Fig. 6.3). For example, the extrema on the maps obtained with the BNC or CRESO estimators are further apart than those shown on Fig. 6.3. It was theoretically predicted (chapter 4) and computationally

verified (chapter 5) that the condition number is larger for the $HLST_2$ model than for the $HLST_1$ model. Thus, the larger errors obtained with the $HLST_2$ model might be due to the increased ill-posedness of the inverse problem.

Finally, inverse maps at $50ms$ (Figs. 6.5-6.7) show that none of the inverse methods were able to recover the complex fusion patterns and to give clinically useful information. For example, the pre-excitation can be localized by the BNC estimator, but not the normal breakthrough on the right ventricle. At this time instant, the source is more complex because of the presence of two distinct breakthroughs. The recovery of such complex distribution under normal noise level constitutes a difficult task for the different inverse methods utilized here.

The magnitude of the recovered epicardial potentials was underestimated as a result of regularization compared with the measured potentials, except for those obtained with the BNC. Examples of these results are shown in Fig. 6.8.

The time behavior of the RMSD between the measured body surface potentials and those computed from the recovered epicardial potentials for the T_1 model using the TikReg and DimCon inverse methods with all estimators is shown in Fig. 6.9. The $RMSD_b$ for both TikReg and DimCon methods reach its peak value at about 60 ms. The maximum value of $RMSD_b$ is about 300 μv. Among all the $RMSD_b$ curves, the one obtained using the BNC estimator shows the lowest values compared with the OPT, CRESO and AIC estimators for both inverse methods. The second lowest $RMSD_b$ distribution is obtained with the AIC estimator using the DimCon method.

The time courses of the correlation coefficient of the epicardial maps for the T_1 model obtained with the different inverse methods are shown in Fig. 6.10. The distribution of the $CC(t)$ is not uniform with respect to time and the higher CC

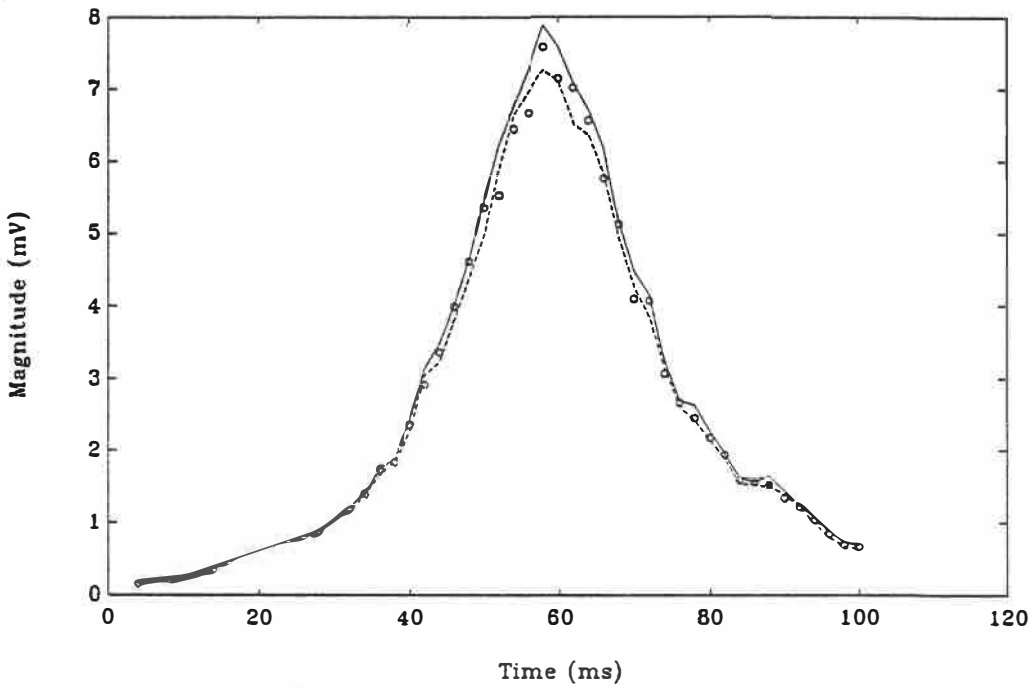

Figure 6.8: Time course of the magnitude of the measured (–) and recovered epicardial potential using the T_1 (o) and $HLST_1$ (- -) models with the TikReg inverse method and the BNC estimator.

values for both inverse procedures occur at around 50 ms. The comparison of the $CC(t)$ obtained with the different methods reveals that the DimCon with OPT estimator provides the best results. The highest $CC(t)$ value obtained with the TikReg and DimCon methods using the OPT estimator was about 0.4 and 0.6, respectively. The temporal behavior of $RE(t)$ for the T_1 model using the different inverse methods is shown in Fig. 6.11. The minimum RE is obtained with the OPT estimator, as expected. Further, the lowest RE and highest CC occur at about 50ms, where the visual evaluation of the recovered maps predicts the worst results. Thus, these quatitative criteria are not easily applicable in this situation

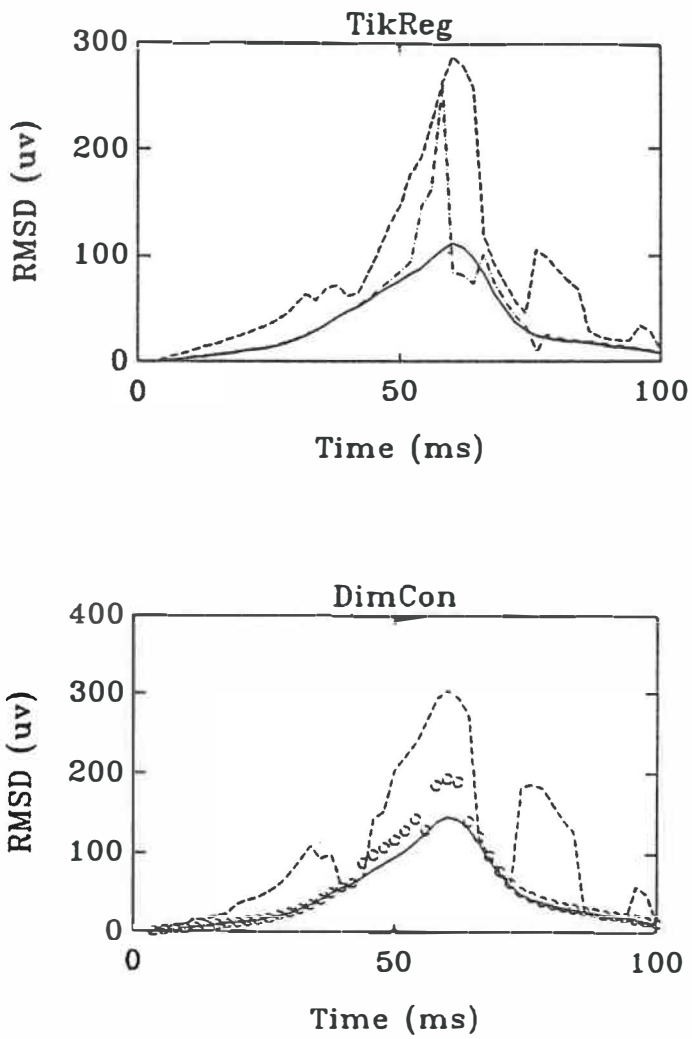

Figure 6.9: Temporal behavior of the RMSD between the measured body surface maps and those computed from recovered epicardial potentials for the T_1 model using TikReg and DimCon inverse methods with BNC (–), OPT (- -), CRESO (-.-) and AIC (o) estimators.

when the error is extremely high.

The variations of the optimum value of the regularization parameter are presented in Fig. 6.12. The values of the regularization parameter are not uniformly distributed in time, and this may be related to the SNR. The values of γ^{TikReg} varied between 10^{-6} and 10^{-1}. Also, the results obtained for each analysis model exhibit different distributions. The mean values of γ^{TikReg} found during the early period of the QRS complex are 10^{-4} for the T_1 and $HLST_1$ models, and 10^{-3} for the T_2 and $HLST_2$ models. The temporal variations of the regularization parameter for the BNC estimator are less than those obtained using the OPT or CRESO estimators. The OPT estimator produced a higher level of regularization than the other estimators.

Fig. 6.13 shows the temporal behavior of the optimum truncation level obtained with the DimCon method using the BNC, OPT or AIC estimators with the T_1 model. It can be observed that the optimum dimension is highest with the BNC estimator than with the OPT or AIC estimators. The distribution of the optimal truncation levels obtained with the AIC estimator exhibits more uniformity than that obtained with the OPT estimator. It is recalled that unlike the OPT estimator, the AIC estimator does not require the use of measured electrograms during the optimization process. The average truncation level set by the OPT and AIC estimators using the T_1 model were 9 and 13, respectively, these were higher than with any of the other five torso models.

6.2 Temporal inverse solutions

The inverse solutions were also calculated as epicardial electrograms for every lead location using the six inverse procedures. The accuracy criteria and the estimators

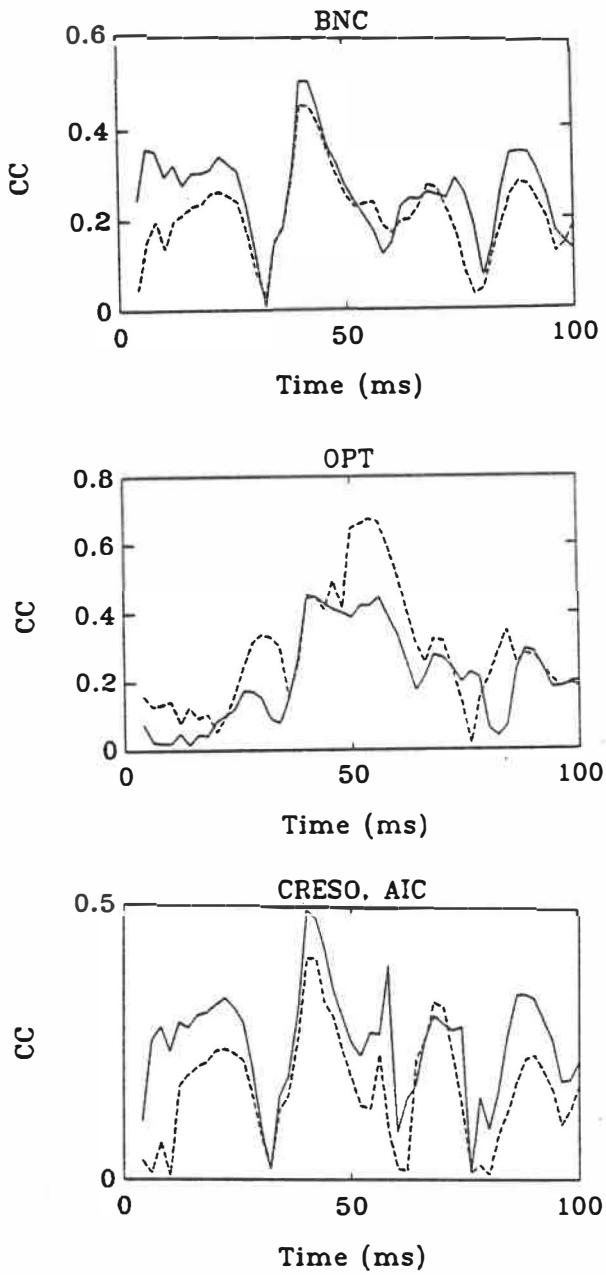

Figure 6.10: Time course of the correlation coefficient of the epicardial maps using the T_1 model with the TikReg (–) and DimCon (- -) inverse methods with the BNC, OPT, CRESO and AIC estimators.

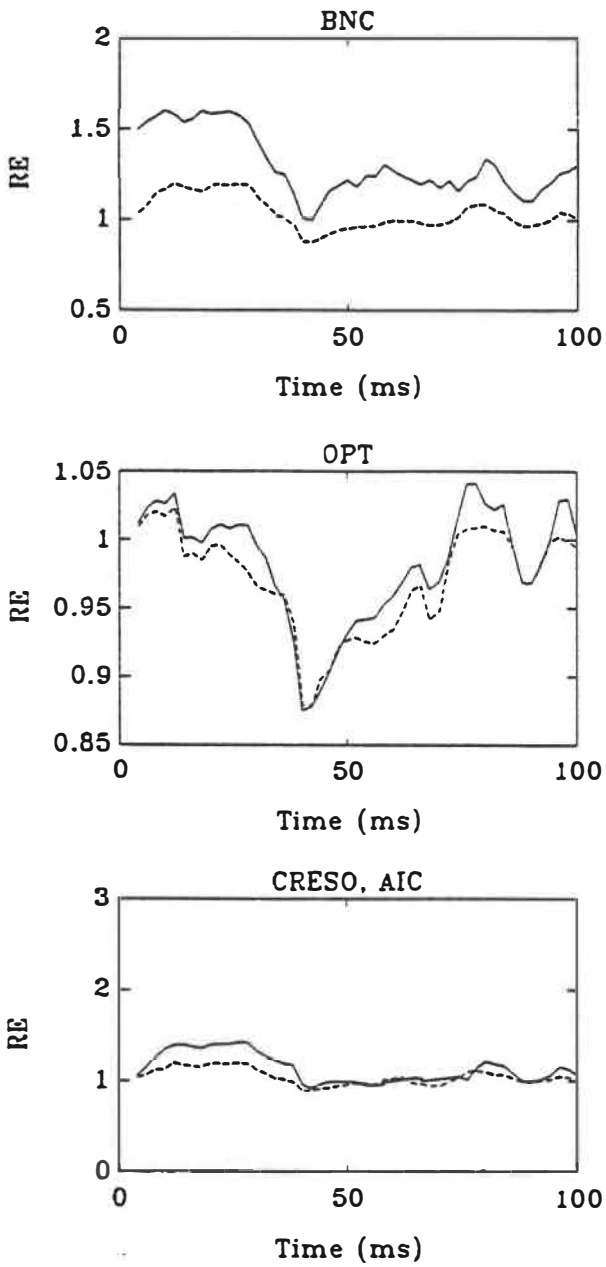

Figure 6.11: Temporal behavior of the relative error of the epicardial maps using the T_1 model with the TikReg (–) and DimCon (- -) inverse methods with the BNC, OPT, CRESO and AIC estimators.

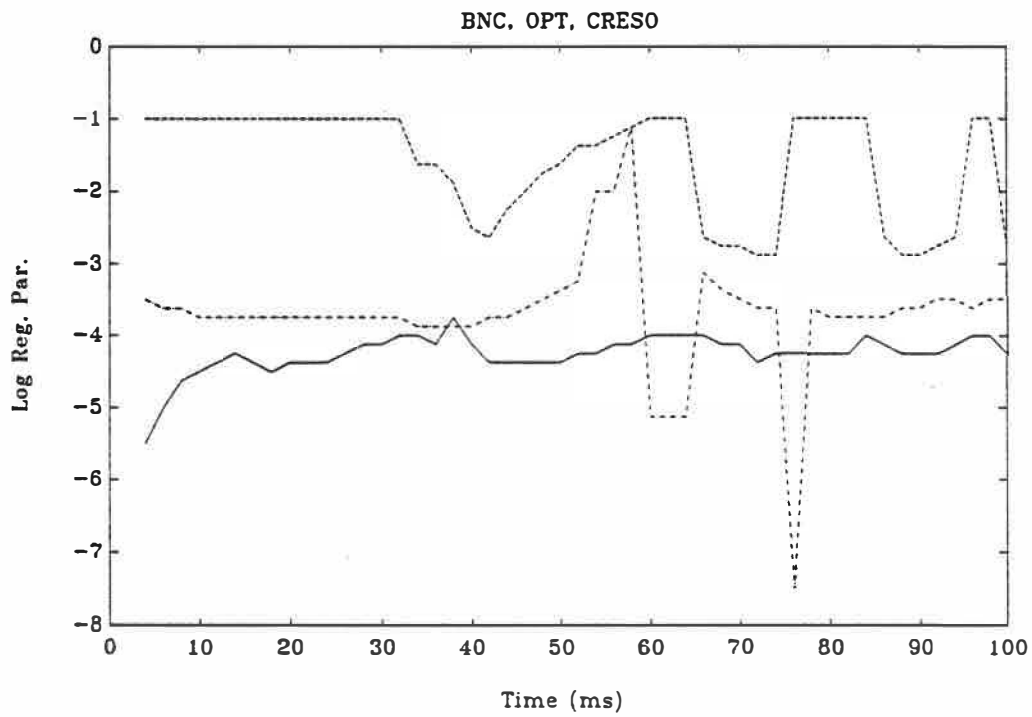

Figure 6.12: Temporal behavior of logarithm of the regularization parameter (γ) as obtained using the TikReg inverse method with the BNC (–), OPT (- -), and CRESO (-.-) estimators using the T_1 model.

were computed for these electrograms, instead of the epicardial maps as presented in section 6.1.

6.2.1 Regularization

A survey of the temporal inverse solutions based on the TikReg method is summarized in Table 6.4. Column 1 shows the volume conductor model; column 2 specifies the estimator; columns 3-6 give the values of the corresponding accuracy criteria obtained as a function of position; and column 7 presents the optimal value of the regularization parameter for the TikReg method.

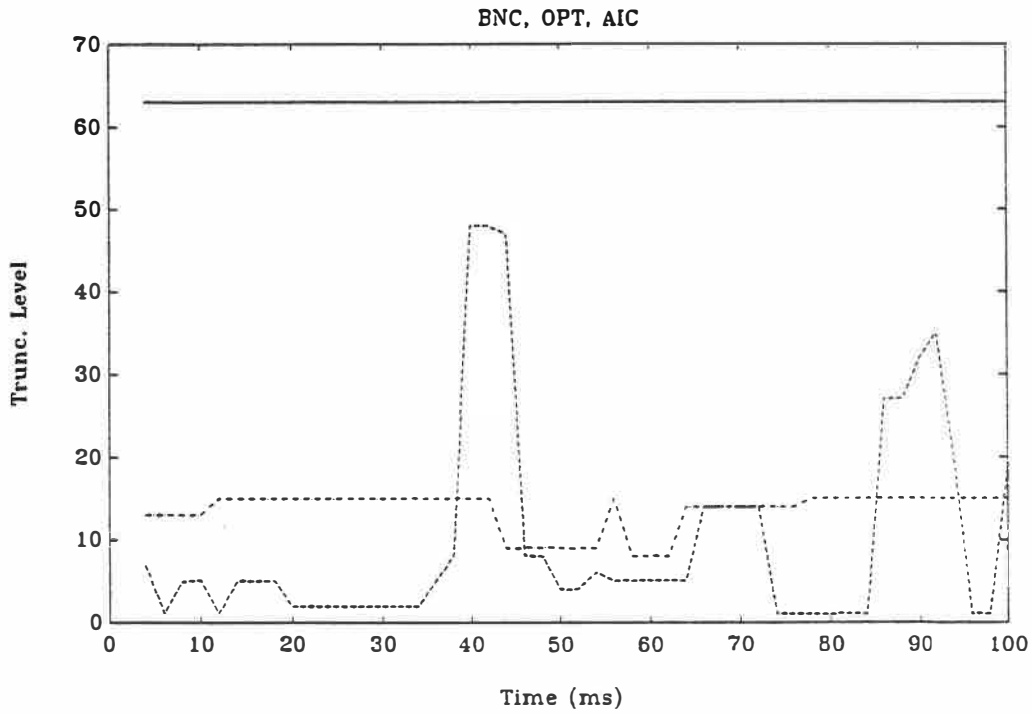

Figure 6.13: Time course of the optimum dimension level as obtained using the DimCon inverse method with the BNC (–), OPT (- -), and AIC (-.-) estimators using the T_1 model.

6.2.2 Control of dimensionality

A survey of the temporal inverse solutions based on the DimCon method is summarized in Table 6.5. Columns 1 through 6 show the same information as Table 6.4, and column 7 presents the optimal value of the dimension for the DimCon method.

6.2.3 Recovered electrograms

The recovered electrograms were also plotted so as to examine visually the time behavior of the inverse solutions. Fig. 6.14 illustrates two neighboring leads (27

Table 6.4: Quantitative results obtained with the TikReg method. Average values of the optimal regularization parameter and accuracy criteria of the recovered epicardial electrograms obtained by applying the TikReg method using the BNC, OPT and AIC estimators for all 6 torso models.

Model	*Estimator*	RE_h	CC_h	$\| \hat{\Phi}_b \| / \| \Phi_b \|$	$RMSD_b$	$\gamma^{TikReg}(10^{-4})$
T_1	BNC	1.189	0.523	0.948	33.8	0.18
LT_1		1.170	0.530	0.917	41.8	0.18
$HLST_1$		1.189	0.522	0.921	41.7	0.18
T_2		1.157	0.524	0.887	49.4	0.18
LT_2		1.191	0.557	0.935	38.4	0.13
$HLST_2$		1.146	0.522	0.891	48.5	0.13
T_1	OPT	0.776	0.651	0.857	55.6	2.37
LT_1		0.790	0.643	0.830	64.4	4.22
$HLST_1$		0.786	0.644	0.835	65.1	4.22
T_2		0.773	0.614	0.796	73.9	4.22
LT_2		0.772	0.647	0.826	59.5	4.22
$HLST_2$		0.770	0.614	0.817	69.5	3.16
T_1	CRESO	2.716	0.528	0.961	31.8	0.08
LT_1		3.559	0.558	0.926	38.3	0.04
$HLST_1$		3.619	0.577	0.935	36.9	0.03
T_2		3.448	0.503	0.938	39.9	0.03
LT_2		2.981	0.520	0.948	32.5	0.03
$HLST_2$		3.751	0.519	0.948	37.4	0.03

and 32) located in the pre-excitation region. The location of these leads is shown at the top of the figure, on the isopotential map measured at $20ms$. Fig. 6.15 shows two other leads (3 and 15), located respectively over the normal breakthrough region on the right ventricle, and over the base, antero-septally.

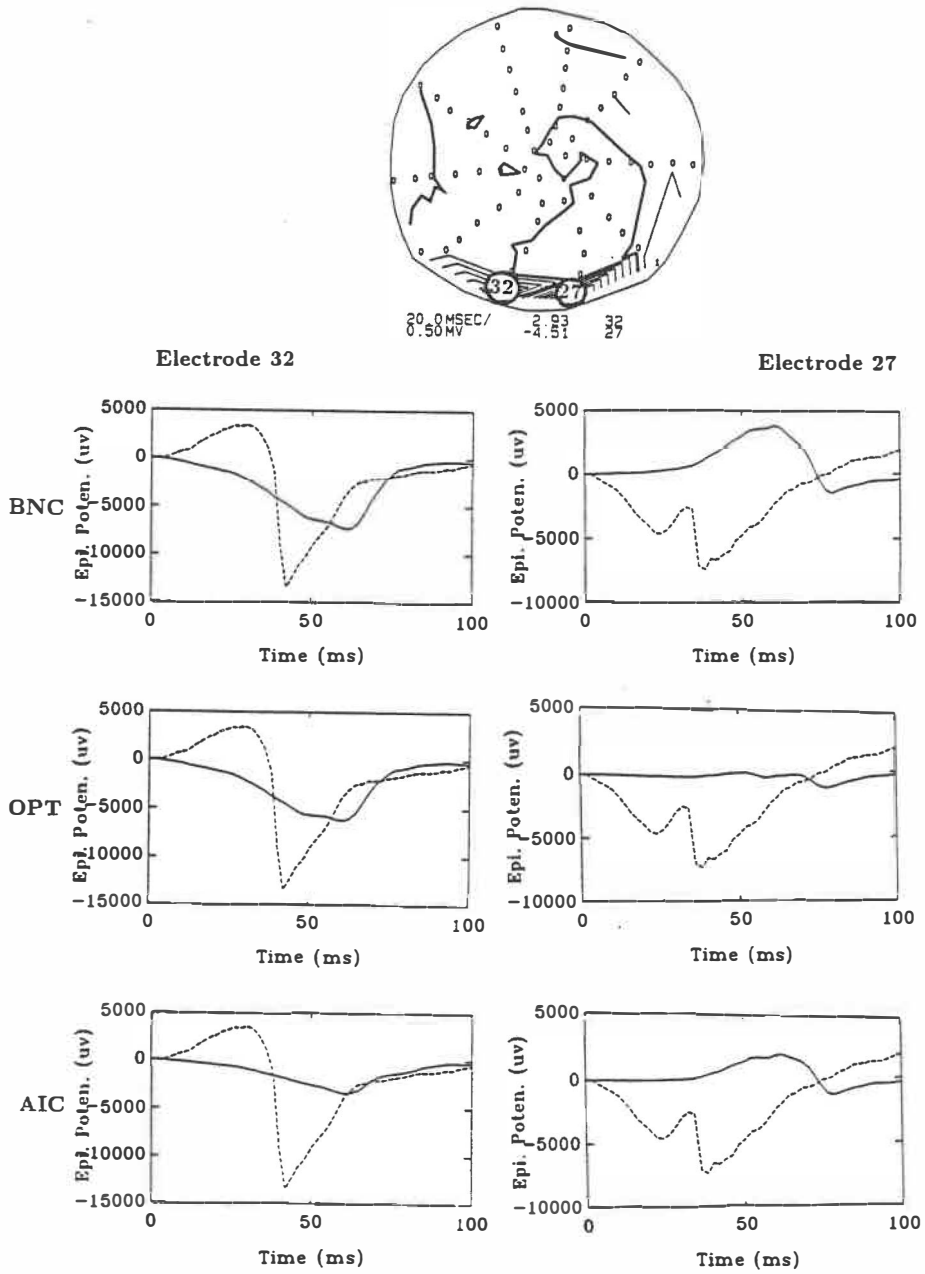

Figure 6.14: Comparison between the measured (- -) and recovered (–) epicardial electrograms for two lead locations, 32 and 27, using the T_1 model and the DimCon inverse method with the BNC, OPT and AIC estimators. The isopotential map measured at $20ms$ is shown for reference.

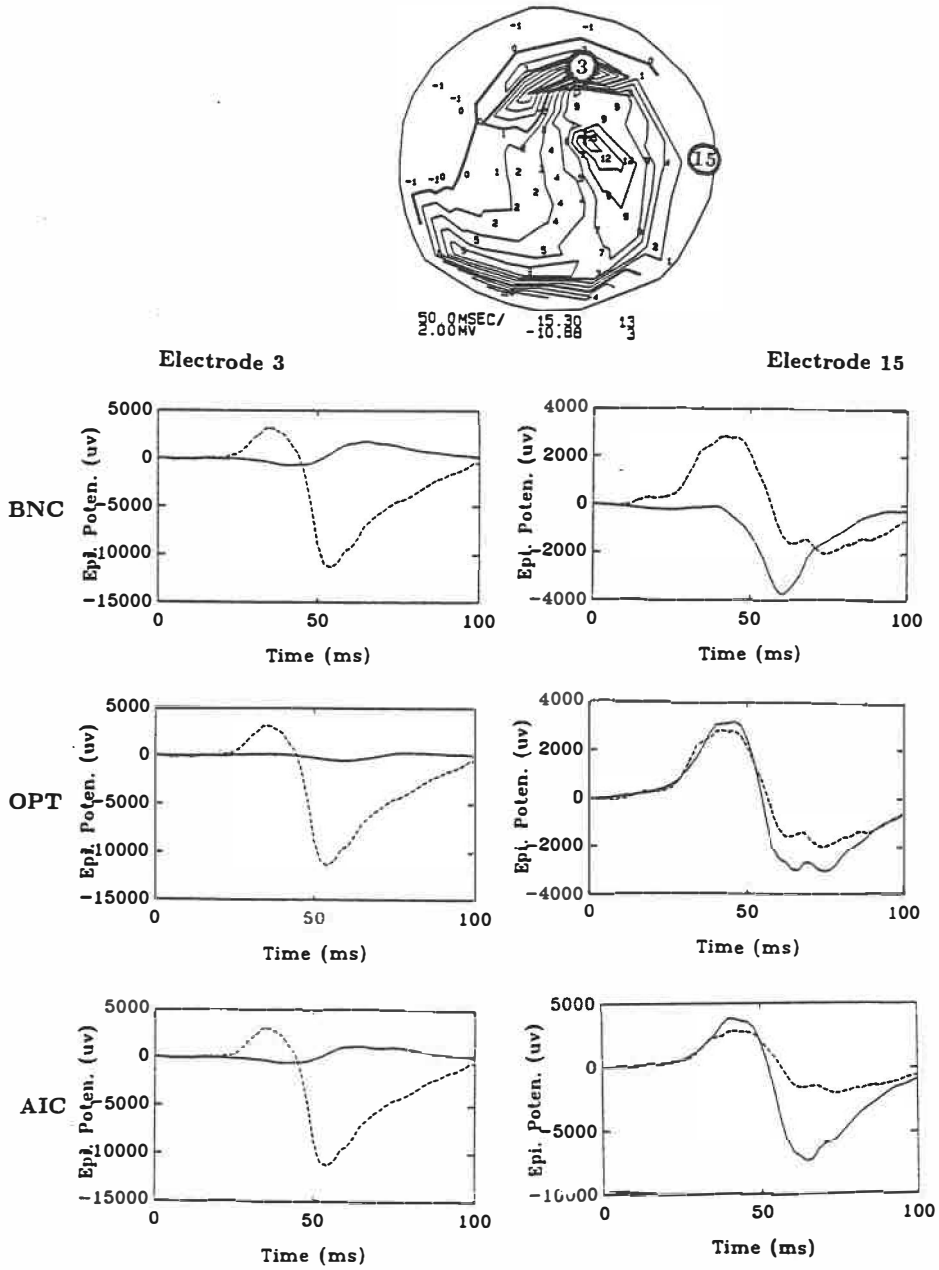

Figure 6.15: Comparison between the measured (- -) and recovered (–) epicardial electrograms for two lead locations, 3 and 15, using the T_1 model and the DimCon inverse method with the BNC, OPT and AIC estimators. The isopotential map measured at $50ms$ is shown for reference.

Table 6.5: Quantitative results obtained with the DimCon method. Average values of the optimal truncation level and accuracy criteria of the recovered epicardial electrograms obtained by applying the DimCon method with $\gamma^{DimCon} = 10^{-3}$ using the BNC, OPT and AIC estimators for all 6 torso models.

Model	*Estimator*	RE_h	CC_h	$\| \hat{\Phi}_b \| / \| \Phi_b \|$	$RMSD_b$	n^{DimCon}
T_1	BNC	0.942	0.523	0.914	52.5	57
LT_1		0.962	0.488	0.871	58.6	55
$HLST_1$		0.964	0.490	0.875	58.7	56
T_2		0.997	0.491	0.792	72.4	51
LT_2		0.967	0.541	0.874	56.7	56
$HLST_2$		0.988	0.496	0.786	72.5	52
T_1	OPT	0.819	0.674	0.809	81.6	11
LT_1		0.818	0.623	0.791	91.9	9
$HLST_1$		0.820	0.625	0.802	90.8	9
T_2		0.813	0.617	0.709	105.3	7
LT_2		0.821	0.632	0.761	97.7	9
$HLST_2$		0.813	0.622	0.726	104.7	7
T_1	AIC	1.079	0.505	0.883	44.5	10
LT_1		1.156	0.504	0.861	52.8	8
$HLST_1$		1.140	0.490	0.860	53.5	8
T_2		1.270	0.473	0.813	60.2	8
LT_2		1.139	0.469	0.857	46.8	9
$HLST_2$		1.289	0.463	0.817	61.8	8

6.2.4 Evaluation of the results

Comparison between the first and second sets of Table 6.4 with the fourth and fifth sets of Table 6.5 reveals that using the DimCon inverse method with either the BNC or OPT estimators improves the inverse results over the TikReg method. Comparing the third set of Table 6.4 with the sixth set of Table 6.5 shows that using the DimCon method with the AIC estimator improves the recovered epicardial electrograms in terms of both the relative error and the correlation coefficient

compared with the TikReg method using the CRESO estimator. However, the errors are high and these tables cannot provide a conclusive evaluation of the performances of the inverse methods and estimators. Indeed, the range of errors is higher than the variations between the methods. Therefore, it is important to examine the recovered electrograms by visual inspection. As seen in Fig. 6.14, the inverse electrograms are smoothed for all inverse procedures. Also electrode 27 shows a positive deflection instead of a negative deflection. The electrogram obtained with the OPT estimator is smoother than its counterpart obtained with the BNC estimator. None of the inverse procedures was able to recover correctly the electrogram from electrode 3 which was over the normal breakthrough region. This is consistent with the spatial results (Figs. 6.5-6.7). However, for other electrode locations the results are satisfactory. Such an example is electrode 15, for which the OPT estimator provides the best results.

6.3 Performance analysis of the spatial and temporal inverse solutions

The observed potential and geometrical data include natural noises. Unlike those inverse recovery experiments which use simulated data, as presented in chapter 5 or reported in the literature [73], here, errors perturb both the H and Φ_b matrices under natural conditions, and therefore limit the resolution of the inverse recovery,

$$\delta^{val}(t_i, \xi_j) = e_h^M + e(e^H, e_b^M, e^I), \tag{6.1}$$

where $\delta^{val}(.,.)$ defines the spatio-temporal discrepancy between the recovered and measured potentials, e_h^M and e_b^M are the epicardial and body surface potential errors due to measurement, e^H and e^I are the errors involved in the inverse recovery

due to the construction of the transfer matrix H and the inverse computation (inverse procedure and computational limitations), respectively.

In this chapter, the evaluation of different solutions to the inverse problem of electrocardiography, obtained by applying a matched-realistic volume conductor model with mixed regularization-truncation inverse methods, was carried out. This is considered an important step towards an application of the inverse procedure in clinical or experimental studies.

Inverse methods. Based on quantitative and qualitative performance criteria, the DimCon inverse method provides better results both in time and space (Tables 6.1-6.5) over the TikReg method. The reason lies in its formulation, which uses the advantage of both regularization and truncation, and finds a good balance between the recovery of the high-frequency components and the stability of inverse solutions. It uses a fixed regularization value during the iteration process to find an inverse solution according to an optimal truncation level. This two-step procedure reduces the effects of the two main errors, those appearing in the transfer matrix and those appearing in the body surface potentials. While the γ^{DimCon} parameter modifies the matrix H, the n^{DimCon} parameter sets limits on the magnification of the noise present in the body surface potentials and prevents excessive oscillations in the inverse solution.

The main computational advantage of the DimCon method over the TikReg method are: (i) The number of iteration steps required to determine the optimal dimension of the truncation level n^{DimCon} is fixed and is known in advance (for example, it is 63 in the present case), while the bounds of the regularization parameter γ in the TikReg method are not known. (ii) The interval between the successive n values is 1 in the DimCon method, while the interval of the successive

γ values is not defined. Both factors impose some uncertainties on deciding the initial and the interval values for γ during the optimization process.

The DimCon method reduces to the truncated singular value decomposition method (TSVD) if γ^{DimCon} is set to zero. The disadvantage of TSVD is that it fails when pushed beyond the resolution threshold set by the kernel. But in the DimCon method, the resolution threshold set by the kernel is modified by introducing $\gamma^{DimCon} = \alpha$. An approximate value for α is sufficient, such as one obtained from the literature, or determined with other method without intensive optimization.

The optimum truncation values obtained with the DimCon method ranged between 7 and 11. This is in agreement with the result of the singular expansion analysis applied to the transfer matrix of the models presented in chapter 5, which predicts an optimum level in the order of 9. The first singular values lead to stronger contributions to the body potentials than the rest, and the truncation will set a limit on the contribution of the body surface potentials on the recovered epicardial patterns.

Estimators. After selecting an inverse method, the problem is to balance the residual against the increasing oscillatory tendency of the recovered solution. The recovered solution is therefore dependent upon the strategy for determining an optimum value of the γ or n parameters. The OPT estimator requires the measured epicardial potentials and hence, it cannot be applied in practice, but it is useful when used as a reference for the other estimators. Both the CRESO and AIC estimators do not require *a priori* knowledge about the epicardial potentials. These two estimators cannot be compared directly to each other, since they are applied through different inverse methods. However, the solutions obtained with

the DimCon and the AIC estimator demonstrated better RE and CC in time or space than the TikReg method with the CRESO estimator (Tables 6.1-6.5). This can be due to the inverse method, their constraint characteristics, or both.

The BNC estimator provided the best results for both inverse methods when qualitative criteria such as the visual examination of the maps were considered. The main feature of the BNC estimator lies in its robust nature, which sets a lower constraint level on the solution space compared with the other estimators. Therefore, it increases the degrees of freedom for choosing a satisfactory regularization parameter or truncation level.

Inhomogeneities. By comparing the inverse maps, it was observed that the addition of conductivity inhomogeneities produced a deterioration of the results for both inverse methods (Figs. 6.2 and 6.3). This effect was not clear in the Tables 6.1-6.5, because the error present in the inverse solutions is higher than the variations due to inhomogeneities. This suggests that the conductivity values that were used might have been wrong, and also, that conductivity values should probably be measured so as to obtain a truly matched torso model.

Mesh resolution. No improvements in the inverse solutions occurred with mesh refinement. Therefore, a computer model with approximatly 5517 nodes seems adequate. It is desirable to minimize discretization errors by increasing the mesh resolution, but this must be balanced by considering the worsening of the condition number due to the increasing dependence of the adjacent rows and columns of the transfer matrix H as the resolution increases.

Errors in epicardial potential measurements. Several problems arise as the validation process is applied in man. The most important ones are the additional errors due to the invasive measurement of the epicardial potentials (air

exposure effects) and the determination of the epicardial lead locations in the computer model. It is important to note that these additional errors affect only the validation process and not the inverse solutions *per se*. Therefore, the actual inverse solutions will contain less errors than reported here.

Thoracic electrodes. It is noted that, here, the optimal number and location of the torso measurement sites has not been investigated. This problem has been studied in a spherical model by Iakovidis [37].

Gain factor. Most of the inverse solutions presented in this chapter exhibit an underestimation of the magnitudes of the potentials. This is because the solutions tend to be over-regularized or over-truncated. This can be corrected by using a modified inverse recovery process that can be divided into three steps. First, recover the epicardial potentials by an inverse procedure (e.g. DimCon). Second, find the value of the gain by forward simulation. Third, multiply the recovered potentials by this gain either uniformly (or non-uniformly along the time or among the leads with the help of a weighting function) to arrive at the final inverse solution.

Temporal versus spatial solutions. Temporal inverse solutions yielded lower $RMSD_b$, RE and higher CC values compared with the spatial inverse results. However, no clinically useful information could be consistently obtained from the visual inspection of the inverse epicardial electrograms. Thus, it is premature to use the temporal inverse results for detection of local activation and isochrone analysis.

Complexity of the source. One of the most striking results is that the quality of the inverse epicardial maps dependeds on the complexity of the measured epicardial maps. When the epicardial source was simple, such as during

pre-excitation (Figs. 6.2-6.4), the inverse maps obtained with estimators requiring no *a priori* information, such as the BNC or CRESO estimators, produced a faithful representation of the measured map and yielded clinically useful information, such as the presence and location of ventricular pre-excitation. When the epicardial sources became more complex, such as during fusion (Figs. 6.5-6.7), none of the inverse maps obtained with the different inverse methods were able to detect or localize the presence of two distinct breakthrough sites. The inverse maps obtained with different methods were either over regularized or showed spurious extrema. Considering the simulation results of chapter 5, which showed that the recovery of the same complex epicardial potentials is possible; this suggests that a higher degree of accuracy in the measurement of the conductivity values and geometrical data for the construction of the torso model may be needed in order to recover complex epicardial potential distributions.

Chapter 7

Conclusion

This thesis makes use of the finite-element model of the torso to study both forward and inverse relationship between epicardial potentials and body-surface electrocardiograms in man.

Forward problem of electrocardiography. The modeling of the human thorax first required representation of the cardiac bioelectric sources as an epicardial potential distribution and properties of the volume conductor, including heart, lungs and spinal region had to be defined. To determine the relationship between the cardiac sources and the electrocardiographic body surface potentials, the finite element method was used to construct the model of the human torso with two mesh resolutions. Finally, field distributions within the torso and on its conductivity interfaces were obtained by application of a preconditioned conjugate gradient method. The methodology made use of available software for solid modeling (PATRAN) and field computation (MagNet3D).

A cylindrically shaped volume conductor, for which an analytical solution exists, was first constructed to verify the accuracy and convergence of the FEM solution. Two series of numerical experiments were performed with different ex-

citation sites and different conductivities; the first series used a lower-resolution model while the second series used a higher-resolution model. The inclusion of the inhomogeneities altered the body surface potential distributions, such as the amplitudes of extrema, but did not substantially modify the pattern of distributions. The greatest effect found on the body surface potentials was due to the addition of the lungs. The spinal region produced only minor changes. Increasing mesh resolution did not influence noticeably the shape or the amplitude of the body surface potential maps; rather, it generally smoothed the isopotential profiles.

Inverse problem of electrocardiography. Theoretical analysis concerning the reduction of the integral equation into a discrete linear system, and the effects of perturbations in the transfer matrix or in the body surface potentials were first presented. This analysis showed that the stability and accuracy of the recovered source function are related to the condition number of the transfer matrix and that the accuracy and rate of convergence of the inverse solution may depend on the modeling approach used to represent the problem domain, (e.g., the number, type and order of the elements used for constructing the model), which affect the condition number; the numerical technique employed to stabilize the solution; the strength of the constraint structure imposed to obtain physically realizable solutions; and the profile of the source function so that it is sufficiently smooth (as characterized by its SVD) that the recovery of information beyond the fundamental frequency limit set by the kernel is not required.

The stability of the inverse problem of electrocardiography was assured by means of two classes of methods, the Tikhonov regularization and the control of dimensionality. Each method was used with three estimators to obtain the optimal value of the regularization parameter, γ, or the dimension, n, respectively.

The implementations of these six inverse procedures were validated by inverse simulations, using sets of simulated (noise-free) data; these inverse simulations demonstrated that the computational errors of all tested inverse procedures are very minor.

Performance analysis of the inverse solutions was then carried out in man by applying a matched-realistic volume conductor model. The inverse epicardial maps obtained with some of the estimators (BNC and CRESO) and torso models (T_1) reproduced important features of the measured maps, such as the pre-excitation region with close extrema near the actual site. However, large relative errors and low correlation coefficients were measured. This can be attributed to the measurement errors in epicardial potentials; namely electrode-location mismatch and altered potential values due to air-exposed electrodes during surgery. Further, the inverse maps computed later during the QRS complex showed that none of the inverse methods were able to recover the complex fusion patterns with multiple breakthrough sites.

Based on quantitative and qualitative performance criteria, the inverse method using control of dimensionality generally provided better or at least equivalent results with respect to the zero-order Tikhonov regularization method. The control of dimensionality method also has some computational advantages; the reason lies in its formulation which has the advantages of both regularization and truncation, and finds a good balance between the recovery of the high frequency components and the stability of the inverse solutions. The choice of the estimator had a more pronounced effect on the inverse solutions than the choice of the inverse method. This is because the final criteria for any inverse method depend on the bound set by the estimator. The narrower the imposed bound set on the solution space,

the more underestimation occurs in the inverse solutions. The BNC estimator provided the best results for both inverse methods when the maps were visually analysed. The main feature of the BNC estimator lies in its robust nature, compared with the other estimators. Therefore, it increases the degrees of freedom for choosing a satisfactory regularization parameter or truncation level.

The inclusion of inhomogeneities with conductivity data obtained from the literature produced a deterioration of the results, for both inverse methods. The influence of the inhomogeneities on both the pattern and magnitude of recovered distributions is not just a linear scaling; rather, distinct shape changes are manifest. This suggests that accurate measurements of the conductivity values of the major organs in the body are required. No improvement in the inverse solutions occurred with mesh refinement. Therefore, a computer model with approximately 5000 nodes seems adequate.

It appears that recovery of epicardial potential distributions in man by means of an inverse procedure is feasible. In this work, clinically useful information has been obtained from the recovered maps, namely the location of the pre-excitation site. However, the accuracy of the recovered epicardial potentials as obtained with the present inverse methods seemed to deteriorate in comparison with the invasively measured epicardial potentials as the degree of complexity of the source increases. An inverse method must consistently demonstrate that it can recover all types of excitation and repolarization processes, so that it can be clinically applied as a routine procedure. To reach this goal, further studies are needed, such as applying the inverse procedure to a wide population of patients with the WPW syndrome and different pre-excitation sites, and incorporating more physiologically acceptable constraints about the epicardial potentials. Also, more

accurate conductivity data for the major organs comprising in the thorax model will be needed. To test objectively the performance of the inverse solution, it will be necessary to improve the measurement techniques (e.g., better documented location of epicardial electrodes, using gated CAT scan to determine anatomical landmarks such as the position of septum, and increasing the number of thoracic electrodes).

Other applications. The heart-torso model and the computational procedures described in this thesis can be applied in physiological volume conductor problems such as: defibrillation and dispersive studies for both external and internal electric excitations, impedance imaging, cerebellar or spinal cord stimulation sudies, biomagnetic problems. The models can readily be used for parameter sensitivity analysis or quantitative investigations of the variables involved for the effective application of these techniques.

References

[1] H. Akaike. "A new look at the statistical model identification". *IEEE Trans. Automat. Contr.*, 19:716–723, 1974.

[2] N. Aronszajin. "A unique continuation theorem for solutions of eliptic partial differential equations or inequalities of second order". *J. Math. Pures App.*, 36:235–249, 1957.

[3] R.C. Barr, T.C. Pilkington, J.P. Boineau, and M.S. Spach. "Determining surface potentials from current dipoles with application to electrocardiography". *IEEE Trans. Biomed. Eng.*, 13:88–92, 1966.

[4] R.C. Barr, M III Ramsey, and M.S. Spach. "Relating epicardial to body surface potential distributions by means of transfer coefficients based on geometry measurements". *IEEE Trans. Biomed. Eng.*, 24:1–11, 1977.

[5] R.C. Barr and M.S. Spach. "Inverse solutions directly in terms of potentials". In C.V. Nelson and D.B. Geselowitz, editors, *The Theoretical Basis of Electrocardiology*, pages 298–304. Oxford University Press, 1976.

[6] R.C. Barr and M.S. Spach. "Inverse calculation of qrs-t epicardial potential from body surface potential distributions for normal and ectopic beats in the intact dog". *Circ. Res.*, 42:661–675, 1978.

[7] W-M Boerner, A.K. Jordan, and I.W. Kay. "Inverse methods in electromagnetics". *IEEE Trans. on Antennas and Propagation*, 29:185--417, 1981.

[8] G. Bonneau, G. Tremblay, P. Savard, R. Guardo, R. Cardinal A.R. LeBlanc, P.L. Page, and R.A. Nadeau. "An integrated system for intraoperarive cardiac activation mapping". *IEEE Trans. on Biomed. Eng.*, 34:415, 1987.

[9] R. Cardinal, P. Savard, D.L. Carson, J.B. Perry, and P. Pagé. "Mapping of ventricular tachycardia induced by programmed stimulation in canine preparations of myocardial infarction". *Circulation*, 70:136–148, 1984.

[10] J. Choi and T.C. Pilkington. "Effects of geometrical uncertainties on electrocardiography". *IEEE Trans. on Biomed. Eng.*, 28:325–334, 1981.

[11] L. Colin. *Proc. of the Workshop on Mathematics of Profile Inversion.* NASA Techn. Memorandum, 1972.

[12] P. Colli-Franzone, L. Guerri, B. Taccardi, and C. Viganotti. *The direct and inverse potential problems in electrocardiography. numerical aspects of some regularization methods and application to data collected in isolated dog heart experiments.* Lab. Anal. Numerica C.N.R., 1979.

[13] P. Colli-Franzone, L. Guerri, B. Taccardi, and C. Viganotti. "Finite element approximation of regularized solutions of the inverse potential problem of electrocardiography and applications to experimental data". *Calcolo*, 12:91–186, 1985.

[14] P. Colli-Franzone, L. Guerri, S. Tenatonia, C. Viganotti, S. Baruffi, S. Spaggiari, and B. Taccardi. "A mathematical procedure for solving the inverse

potential problem of electrocardiography. analysis of the time- space accuracy from experimental data". *Math. Biosci.*, 77:353, 1985.

[15] P. Colli-Franzone, B. Taccardi, and C. Viganotti. "An approach to the inverse calculation of epicardial potentials from body surface maps". *Adv. Cardiol.*, 21:50, 1978.

[16] Infolytica Corporation. *1500 Stanley st. No. 430.* Montreal, Quebec, Canada, H3A 1R3.

[17] J.J.M. Cuppen and Van Oosterom. "Model studies with the inversely calculated isochrones of ventricular depolarization". *IEEE Trans. Biomed. Eng.*, 31:652–659, 1984.

[18] A.A. Damen and J. van der Kam. "The use of the sigular decomposition in electrocardiography". *Med. Biol. Eng. Comput.*, 20:473–482, 1982.

[19] J. de Guise, R.M. Gulrajani, P. Savard, R. Guardo, and F.A. Roberge. "Inverse recovery of two moving dipoles from simulated surface potential distributions on a realistic human torso model". *IEEE Trans. Biomed. Eng.*, 32:126, 1985.

[20] D. Durrer, G.E. Freud R.Th. van Dam, M.J. Janse, F.L. Meijler, and R.C. Arzbaecher. "Total excitation of the isolated human heart". *Circulation*, 41:899–912, 1970.

[21] PDA Engineering. *1560 Brookhollow Drive, Santa Anna.* California, 92705.

[22] M. Foster. "An application of the wiener-kolmogorov smoothing theory to matrix inversion". *J. Soc. Ind. Appl. Math.*, 9:387, 1961.

[23] H.L. Gelernter and J.C. Swihart. "A mathematical-physical model of the genesis of the electrocardiogram". *Biophys. J.*, 4:285–301, 1964.

[24] D.B. Geselowitz. "Multipole representation for an equivalent cardiac generator". *Proc. IRE*, 48:75–79, 1960.

[25] G.H. Golub and C.F. Van Loan. *Matrix computations.* Johns Hopkins University Press, 1983.

[26] A.V. Goncharskii, A.S. Leonov, and A.G. Yagola. "A generalized discrepancy principle". *Zh. Vychisl. Mat. i Mat. Fiz.*, 13:294–302, 1973.

[27] R.M. Gulrajani. "Models of the electrical activity of the heart and computer simulation of the electrocardiogram". *CRC Crit. Rev. Biomed. Eng.*, 16:1–66, 1988.

[28] R.M. Gulrajani, F.A. Roberge, and G.E. Mailloux. "The forward problem of electrocardiography". In P.W. Macfarlane and T.D.V. Lawrie, editors, *Comprehensive Electrocardiography*, page Chap. 8. Pergamon Press, 1988.

[29] R.M. Gulrajani, P. Savard, and F.A. Roberge. "The inverse problem of electrocardiography: solutions in terms of equivalent sources". *CRC Crit. Rev. Biomed. Eng.*, 16:171–214, 1988.

[30] J. Hadamard. *Lectures on the Cauchy problem in linear partial differential equations.* Yale University Press, 1923.

[31] L.T. Hersh, R.C. Barr, and M.S. Spach. "An analysis of transfer coefficients calculated directly from epicardial and body surface potential measurements in the intact dog". *IEEE Trans. Biomed. Eng.*, 25:446–461, 1978.

[32] B.M. Horáček, R.G. de Boer, L.J. Leon, and T.J. Montague. "Human epicardial potential distributions computed from body-surface-available data". In K. Harumi K. Yamada and T. Musha, editors, *Advances in body surface potential mapping*, pages 47–54. University of Nagoya Press, 1983.

[33] L.G. Horan, N.C. Flowers, and D.A. Brody. "Body surface potential distribution in comparison of naturally and artificially produced signals as analyzed by digital computer". *Circ. Res.*, 13:373–387, 1963.

[34] T.J.R. Hughes. *The finite element method-linear static and dynamic analysis.* Prentic-Hall, 1987.

[35] G. Huiskamp. *Noninvasive determination of human ventricular activation.* PhD thesis, University of Nijmegen, Nijmegen, The Netherlands, 1989.

[36] G. Huiskamp and A. van Oosterom. "Tailored versus realistic geometry in the inverse problem of electrocardiography". *IEEE Trans. Biom. Eng.*, 36:827–835, 1989.

[37] I. Iakovidis. *Observability and the inverse problem in electrocardiography.* PhD thesis, Texas Tech University, 1990.

[38] Y. Kim. *A three-dimensional modifiable computer body model and its applications.* PhD thesis, University of Wisconsin, Madison, WI 53706, 1982.

[39] C.L. Lawson and R.J. Hanson. *Solving least square problems.* Prentice-Hall, 1974.

[40] G-C. Lo. *Estimation of epicardial electrical potentials from body surface meaurements based on a digital simulation of the human thorax.* PhD thesis,

Imperical College of Science and Technology, London,England, 1977.

[41] R.S. MacLeod. *Percutaneous transluminal coronary angioplasty as a model of cardiac ischemia: clinical and modeling studies.* PhD thesis, Dalhousie University, Halifax, Nova Scotia, Canada, 1990.

[42] R.O. Martin and T.C. Pilkington. "Unconstrained inverse electrocardiography: Epicardial potentials". *IEEE Trans. Biomed. Eng.*, 19:276–285, 1972.

[43] B. Messinger-Rapport and Y. Rudy. "Rgularization of the inverse problem in electrocardiography: a model study". *Math. Biosci.*, 89:79, 1988.

[44] P.N. Morse and H. Feshbach. *Methods of theoretical physics.* McGraw-Hill, 1953.

[45] R.A. Nadeau, P. Savard, G. Faugere, M. Shenasa, P. Page, R.M. Gulrajani, R.A. Guardo, and R. Cardinal. "Localization of pre-excitation sites in wolff-parkinson-white syndrome by body surface potential mapping and a single moving dipole representation". In R.T. van Dam and A. van Oosterom, editors, *Electrocardiographic body surface mapping.* Martinus Nijhoff Publ., 1986.

[46] M.Z. Nashed. *Ill-posed problems: theory and practice.* Reidel, 1981.

[47] M.Z. Nashed. "Operator-theoretic and computational approaches to ill-posed problems with application to antenna theory". *IEEE Trans. Antennas. and Propagat.*, 29:220–231, 1981.

[48] F. Natterer. "Numerical treatment of ill-posed problems". In G. Talenti, editor, *Lecture notes in mathematics, vol. 1225.* Springer, 1986.

[49] R. Okada. "Potentials produced by an eccentric current dipole in a finite-length circular conducting cylinder". *IRE Trans. Med. Electron*, 7:14–19, 1956.

[50] L.E. Payne. "Some general remarks on improperly posed problems for partial differential equations". *Lecture notes in mathematics*, 316:1–29, 1973.

[51] R. Plonsey. *Bioelectric phenomena.* McGraw-Hill, 1969.

[52] Y. Rudy and B. Messinger-Rapport. "The inverse problem of electrocardiography: solutions in terms of epicardial potentials". *CRC Crit. Rev. Biomed. Eng.*, 16:215–268, 1988.

[53] S. Rush, J.A. Abildskov, and McFee. "Resistivity of body tissues at low frequencies". *Circ. Res.*, 12:40, 1963.

[54] P. Savard, S. Boucher, R. Cardinal, and R. Giasson. "Localization of cardiac electrical activity by a single moving dipole during ventricular tachycardia in dog: Validation by epicardial activation mapping". In R.T. van Dam and A. van Oosterom, editors, *Electrocardiographic body surface mapping.* Martinus Nijhoff Publ., 1986.

[55] P. Savard, F.A. Roberge, J.B. Perry, and R.A. Nadeau. "Representation of cardiac electrical activity by a moving dipole for normal and ectopic beats in the intact dog". *Circ. Res.*, 46:415–425, 1980.

[56] A.M. Scher, A.C. Young, and W.M. Meredith. "Factor analysis of electrocardiogram". *Circ. Res.*, 8:519–526, 1960.

[57] R. Selvester, C.C. Collier, and R.B. Pearson. "Analog computer model of the vectorcardiogram". *Circulation*, 31:45–53, 1965.

[58] A. Vahid Shahidi and P. Savard. "3-d reconstruction and finite element mesh generation of the human heart-torso". *Proc. of the 14th C.M.B.E.C., Montreal, Quebec, Canada*, 14:95–96, 1988.

[59] A. Vahid Shahidi and P. Savard. "A volume conductor of the human thorax for field calculations". *Proc. of annual conf. on Eng. in Medicine and Biology*, 12:615–616, 1990.

[60] P.P. Silvester and R.L. Ferrari. *Finite elements for electrical engineers.* Cambridge University Press, 1983.

[61] P.P. Silvester and S. Tymchyshyn. "Finite-element modeling of the inhomogeneous human thorax". *Adv. Cardiol.*, 10:46–50, 1974.

[62] B. Soucy. *Etude des problemes direct et inverse de l'electrocardiographie a l'aide d'un modele experimental coeur-torse.* M.Sc.A. thesis, Ecole polytechnique de Montreal, 1990.

[63] K. Tanabe. "Statistical regularization of noisy ill-conditioned system of linear equations by akaike's information criterion". *Comput. Anal.*, 6:2–25, 1975.

[64] M.N. Morrow T.C. Pilkington and P.C. Stanley. "A comparison of finite element and integral equation formulations for the calculation of electrocardiographic potentials". *IEEE Trans. Biomed. Eng.*, 32:166–173, 1985.

[65] M.N. Morrow T.C. Pilkington and P.C. Stanley. "A comparison of finite

element and integral equation formulations for the calculation of electrocardiographic potentials. ii". *IEEE Trans. Biomed. Eng.*, 34:258, 1987.

[66] A.N. Tikhonov. "Solution of incorrectly formulated programs and the regularization method". *Sov. Math. Dokl.*, 4:1035, 1963.

[67] A.N. Tikhonov and V.Y. Arsenin. *Solution of ill-posed problems.* John Wiley, 1977.

[68] S. Toyama, K. Suzuki, T. Takahashi, and Y. Yamashita. "Epicardial isopotential mapping from body surface isopotential mapping in myocardial infarction". *J. Electrocardiol.*, 18:277–285, 1985.

[69] S. Twomey. "On the numerical solution of fredholm integral equations of first kind by the inversion of the linear system produced by quadrature". *J. ACM*, 10:97–101, 1963.

[70] S.J. Walker and D. Kilpatrick. "Forward and inverse electrocardiographic calculations using resistor network models of the human torso". *Circ. Res.*, 61:504, 1987.

[71] Y. Yamashita. "Theoretical studies on the inverse problem in electrocardiography and uniqueness of the solution". *IEEE Trans. Biomed. Eng.*, 29:719–725, 1982.

[72] Y. Yamashita and T. Takahashi. "On the properties of the inverse solution in ecg: determining epicardial from body surface potentials by using the finite element method". In S. Kaihara D.A.B. Lindberg, editor, *MEDINFO 80*, pages 264–268. North-Holland, 1980.

[73] Y. Yamashita and T. Takahashi. "Use of finite element method to determine epicardial from body surface potentials under a realistic torso model". *IEEE Trans. Biomed. Eng.*, 26:611–621, 1984.

[74] L. Zablow. "An equivalent cardiac generator which preserves topography". *Biophys. J.*, 6:535–536, 1966.

[75] O.C. Zienkiewicz. *The finite element method.* McGraw-Hill, 1977.

Appendix A

Shape functions and simplex coordinates

A.1 Shape functions

To derive shape functions for a 4-node tetrahedral element in terms of the global coordinate (x, y, z), let the *parameter function* in matrix form be

$$\hat{\phi} = \begin{pmatrix} 1 & x & y & z \end{pmatrix} \begin{pmatrix} a \\ b \\ c \\ d \end{pmatrix} \tag{A.1}$$

at node i , $\{i = 1, 2, 3, 4\}$, with respect to the positions (x_i, y_i, z_i) then $\hat{\phi}_i$ yields,

$$\begin{pmatrix} \hat{\phi}_1 \\ \hat{\phi}_2 \\ \hat{\phi}_3 \\ \hat{\phi}_4 \end{pmatrix} = \begin{pmatrix} 1 & x_1 & y_1 & z_1 \\ 1 & x_2 & y_2 & z_2 \\ 1 & x_3 & y_3 & z_3 \\ 1 & x_4 & y_4 & z_4 \end{pmatrix} \begin{pmatrix} a \\ b \\ c \\ d \end{pmatrix}. \tag{A.2}$$

Solving for the constant vector and substituting the results into equation (A.1) yields

$$\hat{\phi} = \begin{pmatrix} 1 & x & y & z \end{pmatrix} \begin{pmatrix} 1 & x_1 & y_1 & z_1 \\ 1 & x_2 & y_2 & z_2 \\ 1 & x_3 & y_3 & z_3 \\ 1 & x_4 & y_4 & z_4 \end{pmatrix}^{-1} \begin{pmatrix} \hat{\phi}_1 \\ \hat{\phi}_2 \\ \hat{\phi}_3 \\ \hat{\phi}_4 \end{pmatrix}, \tag{A.3}$$

which has the form

$$\hat{\phi} = \sum_{m=1}^{4} \alpha_m(x,y,z)\hat{\phi}_m \tag{A.4}$$

where the *shape functions* are given by

$$\alpha_1(x,y,z) = c_{11} + c_{21}x + c_{31}y + c_{41}z \tag{A.5}$$

$$\alpha_2(x,y,z) = c_{12} + c_{22}x + c_{32}y + c_{42}z \tag{A.6}$$

$$\alpha_3(x,y,z) = c_{13} + c_{23}x + c_{33}y + c_{43}z \tag{A.7}$$

$$\alpha_4(x,y,z) = c_{14} + c_{24}x + c_{34}y + c_{44}z \tag{A.8}$$

$$\tag{A.9}$$

where

$$c_{11} = \frac{1}{3!V}\det\begin{pmatrix} x_2 & y_2 & z_2 \\ x_3 & y_3 & z_3 \\ x_4 & y_4 & z_4 \end{pmatrix} \quad c_{21} = -\frac{1}{3!V}\det\begin{pmatrix} 1 & y_2 & z_2 \\ 1 & y_3 & z_3 \\ 1 & y_4 & z_4 \end{pmatrix} \tag{A.10}$$

$$c_{31} = \frac{1}{3!V}\det\begin{pmatrix} 1 & x_2 & z_2 \\ 1 & x_3 & z_3 \\ 1 & x_4 & z_4 \end{pmatrix} \quad c_{41} = -\frac{1}{3!V}\det\begin{pmatrix} 1 & x_2 & y_2 \\ 1 & x_3 & y_3 \\ 1 & x_4 & y_4 \end{pmatrix} \tag{A.11}$$

$$\tag{A.12}$$

and other c's can be found by cyclic permutation. Here V is the volume of tetrahedron in term of nodal coordinates

$$V = \frac{1}{3!}\det\begin{pmatrix} 1 & x_1 & y_1 & z_1 \\ 1 & x_2 & y_2 & z_2 \\ 1 & x_3 & y_3 & z_3 \\ 1 & x_4 & y_4 & z_4 \end{pmatrix}. \tag{A.13}$$

A.2 Simplex coordinates

Let an internal point $p(x,y,z)$ be defined within a tetrahedral element and four smaller tetrahedrons with volumes V_1, V_2, V_3 and V_4, as shown in Figure A.1.

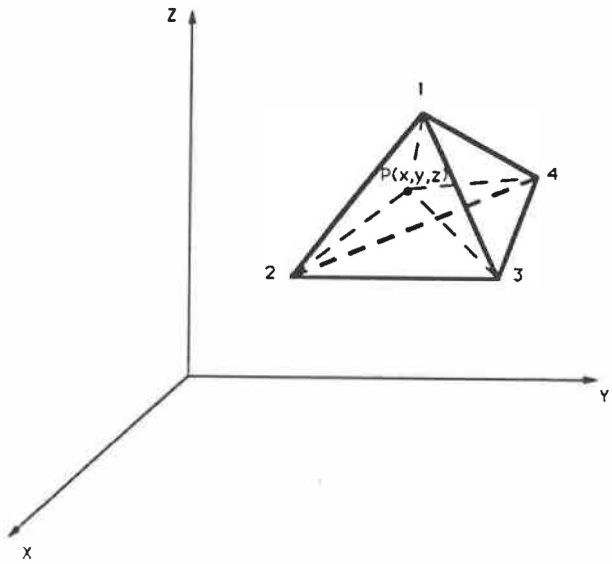

Figure A.1: Tetrahedral element.

Then define *simplex coordinates* $\psi_i\{i = 1, 2, 3, 4\}$ as follows

$$\psi_i = \frac{V_i}{V} \tag{A.14}$$

where V is the total volume of the tetrahedron (A.13). Therefore, we have

$$\sum_{i=1}^{4} \psi_i = 1. \tag{A.15}$$

Proposition: The simplex coordinates ψ_i are the same as the shape functions α_i.

Proof: Using the definition of ψ_i, we have

$$\psi_1 = \frac{1}{3!V}\det\begin{pmatrix} x_2 & y_2 & z_2 \\ x_3 & y_3 & z_3 \\ x_4 & y_4 & z_4 \end{pmatrix} - \frac{x}{3!V}\det\begin{pmatrix} 1 & y_2 & z_2 \\ 1 & y_3 & z_3 \\ 1 & y_4 & z_4 \end{pmatrix} \tag{A.16}$$

$$+\frac{y}{3!V}\det\begin{pmatrix} 1 & x_2 & z_2 \\ 1 & x_3 & z_3 \\ 1 & x_4 & z_4 \end{pmatrix} - \frac{z}{3!V}\det\begin{pmatrix} 1 & x_2 & y_2 \\ 1 & x_3 & y_3 \\ 1 & x_4 & y_4 \end{pmatrix}, \tag{A.17}$$

or,

$$\psi_1 = c_{11} + c_{21} + c_{31} + c_{41} = \alpha_1(x, y, z) \tag{A.18}$$

Similarly, ψ_2, ψ_3 and ψ_4, or in general

$$\psi_i = \frac{a_i + b_i x + c_i y + d_i z}{3!V} \tag{A.19}$$

where a_i, b_i, c_i and d_i are cofactors.

Appendix B

Coordinate transformation and integral formulas

Solution to equation (2.17) requires the integration of equations (2.18) over the elemental volume Ω^e, for the present case, a tetrahedral element. Transforming the cartesian coordinate into homogenous space coordinates ψ_1, ψ_2, ψ_3 and $\psi_4 = 1 - \psi_1 - \psi_2 - \psi_3$ demands the *Jacobian transformation* and yields the replacement of $d\Omega = dxdydz$ to:

$$d\psi_1 d\psi_2 \psi_3 \Big/ \frac{\partial(\psi_1, \psi_2, \psi_3)}{\partial(x, y, z)} \tag{B.1}$$

where,

$$\frac{\partial(\psi_1, \psi_2, \psi_3)}{\partial(x, y, z)} = \det \begin{pmatrix} \frac{\partial \psi_1}{\partial x} & \frac{\partial \psi_1}{\partial y} & \frac{\partial \psi_1}{\partial z} \\ \frac{\partial \psi_2}{\partial x} & \frac{\partial \psi_2}{\partial y} & \frac{\partial \psi_2}{\partial z} \\ \frac{\partial \psi_3}{\partial x} & \frac{\partial \psi_3}{\partial y} & \frac{\partial \psi_3}{\partial z} \end{pmatrix} \tag{B.2}$$

but the magnitude of the Jacobian is $\frac{1}{3!V}$, therefore,

$$dxdydz = 3!\, V d\psi_1 d\psi_2 d\psi_3. \tag{B.3}$$

Using equation (A.19) and the chain rule of differentiation, then equation (2.18) becomes,

$$A_{mn} = \sum_{i=1}^{4}\sum_{j=1}^{4} \sigma K_{ij} \int_{\Omega_e} 6(\frac{\partial \alpha_m}{\partial \psi_i}\frac{\partial \alpha_n}{\partial \psi_j}) d\psi_1 d\psi_2 d\psi_3 \tag{B.4}$$

with,

$$K_{ij} = \frac{b_i b_j + c_i c_j + d_i d_j}{36V}. \tag{B.5}$$

Let,

$$Q^{ij}_{mn} = -6 \int_{\Omega_e} (\frac{\partial \alpha_m}{\partial \psi_i} - \frac{\partial \alpha_m}{\partial \psi_j})(\frac{\partial \alpha_n}{\partial \psi_i} - \frac{\partial \alpha_n}{\partial \psi_j}) d\psi_1 d\psi_2 d\psi_3 \tag{B.6}$$

and replacing ψ_4 by $1 - \psi_1 - \psi_2 - \psi_3$, then equation (B.4) becomes,

$$A_{mn} = \sum_{i=1}^{3} \sum_{j=i+1}^{4} \sigma K_{ij} Q^{ij}_{mn}. \tag{B.7}$$

Q^{ij}_{mn} is a numerical array which will be calculated once for a given order of polynominal function but K_{ij} includes information about geometric shape, size and position of tetrahedron. Similarly, for the source term C we get,

$$C_m = 6V \int \alpha_m I_s \; d\psi_1 \; d\psi_2 \; d\psi_3. \tag{B.8}$$

Appendix C

Analytical solution of potential distribution for a solid cylinder

Consider a point source of strength I_s in an infinite homogeneous medium with conductivity σ, the potential distribution is

$$\phi_\infty = \frac{I_s}{4\pi\sigma R} \tag{C.1}$$

where R is the distance from a point p to the locaton of the dipole source. The inverse distance can be expressed as [49]

$$\frac{1}{R} = \frac{2}{\pi}\int_0^\infty cos\lambda(z-z')\sum_{m=0}^{\infty}(2-\delta_m^0)K_m(\lambda\rho)I_n(\lambda\rho')cosm(\theta-\theta')d\lambda \tag{C.2}$$

where K_m and I_m are modified Bessel functions of order m.

The potential distribution resulting from a dipole oriented in the positive z direction is obtained by partial differentiation of the point source with respect to z and replacing I_s by the dipole moment p_z, then we have [49]

$$\begin{aligned}\phi_{\infty_z} &= \frac{p_z}{2\pi^2\sigma}\int_0^\infty \lambda sin\lambda(z-z'). \\ &\sum_{m=0}^{\infty}(2-\delta_m^0 K_m(\lambda\rho)I_m(\lambda\rho')cosm(\theta-\theta')d\lambda \end{aligned} \tag{C.3}$$

In the case of a finite length circular cylinder and satisfying the boundary conditions we have

$$\begin{aligned}\phi_z &= \frac{p_z}{2\pi^2\sigma}\int_0^\infty f(a,\lambda)\lambda sin\lambda(z-z'). \\ &\sum_{m=0}^{\infty}(2-\delta_m^0)[K_m(\lambda\rho)C_1 I_m(\lambda\rho)]I_m(\lambda\rho')cosm(\theta-\theta')d\lambda \qquad (C.4)\end{aligned}$$

Using the condition

$$\frac{d\phi_z}{d\rho}\,|_{\rho=b} = 0 \qquad (C.5)$$

then,

$$C_1 = -\frac{K_m'(\lambda b)}{I_m'(\lambda b} \qquad (C.6)$$

where the primes denote differentiation with respect to the argument. Using the condition

$$\frac{d\phi_z}{d\rho}\,|_{z=0} = 0 \qquad (C.7)$$

excluding the term $sin\lambda z cos\lambda z'$. Taking double summation over the angle coordinate with index m, we get

$$\begin{aligned}\phi_z &= -\frac{p_z}{2a\pi\sigma}\sum_{n=0}^{\infty}(2-\delta_n^0)\frac{n\pi}{a}sin\frac{n\pi z'}{a}cos\frac{n\pi z}{a}. \\ &\sum_{m=0}^{\infty}(2-\delta_m^0)[K_m(\frac{n\pi\rho}{a}) - \frac{K_m'(\frac{n\pi b}{a})}{I_m'(\frac{n\pi b}{a})}I_m(\frac{n\pi\rho}{a})]. \\ &I_m(\frac{n\pi\rho'}{a})cosm(\theta-\theta') \qquad (C.8)\end{aligned}$$

Specific solution. Considering the potential at the boundaries, then substitute $\rho = b$ in equation (C.8) yields

$$\begin{aligned}\phi_z &= -\frac{p_z}{ab\pi\sigma}\sum_{n=0}^{\infty}(2-\delta_n^0)sin\frac{n\pi z'}{a}cos\frac{n\pi z}{a}. \\ &\sum_{m=0}^{\infty}(2-\delta_m^0)\frac{I_m(\frac{n\pi\rho'}{a})}{I_{m-1}(\frac{n\pi b}{a}) + I_{m+1}(\frac{n\pi b}{a})}cosm(\theta-\theta') \qquad (C.9)\end{aligned}$$

For a dipole located on the axis of the cylinder, i.e. $\rho' = 0$ and the solution simplifies to

$$\phi_z = \frac{-p_z}{ab\pi\sigma} \sum_{n=0}^{\infty} (2 - \delta_0^n) \frac{cos(\frac{n\pi z}{a}) sin(\frac{n\pi z'}{a})}{I_1(\frac{n\pi b}{a})} \quad . \tag{C.10}$$

Appendix D

Forward simulations

The purpose of this appendix is to present and analyze simulated body surface potential maps obtained by multiplying the vector comprising the 63 epicardial potentials measured at one time instant, by the transfer matrix associated with a given torso model.

Figure D.1 shows the measured thoracic maps at $10ms$ intervals during the QRS. It is interesting to note that the maps measured between 10 and $50ms$ reflect mostly the ventricular pre-excitation. According to accepted interpretation criteria, these maps reflect a left anterior pre-excitation site. The presence of the minimum on the upper anterior torso between 70 and $100ms$ reflect the normal breakthrough and the activation of the right ventricle.

Simulated maps obtained with the T_1 model between 10 and $50ms$ (Fig. D.2) show much more variability than the measured maps during the same time interval. This may be attributed to the small number of epicardial electrodes. Indeed, only three or four electrodes are sensing large potentials in the small pre-excitation region and the smooth progression of the activation is represented as discrete jumps between electrode sites. It is also noticed that on these simulated

maps the inferior torso is not positive as in the measured maps which is typical of a left anterior pre-excitation site. The simulated maps reflect more a left lateral pre-excitation site (specially at $20ms$). This can be explained by a rotation of the sock electrode array during the measurement of the location of the epicardial electrodes (section 5.3). During the rest of QRS ($70 - 100ms$), the simulated maps show a minimum on the anterior torso as in the measured maps, but the locations of the maximum are quite different. These differences can be attributed either to the measurement of the epicardial potentials (e.g. electrode array rotation, air exposure) or the torso model (e.g. conductivity). The simulated maps obtained with the other models (Figures D.3-D.6) show similar body surface potential distributions with maximum and minimum that are often located at the same sites.

Unlike the inverse problem of electrocardiography the forward problem is not ill-conditioned. Thus, forward simulations such as those described in this appendix are expected to produce less discrepancy between measured and simulated potentials than inverse solutions, such those described in chapter 6. The discrepancies that are observed in these forward simulations suggest that problems in the measurement of the epicardial potentials, such as electrode array rotation, may have been occurred and may hamper the evaluation of the inverse maps.

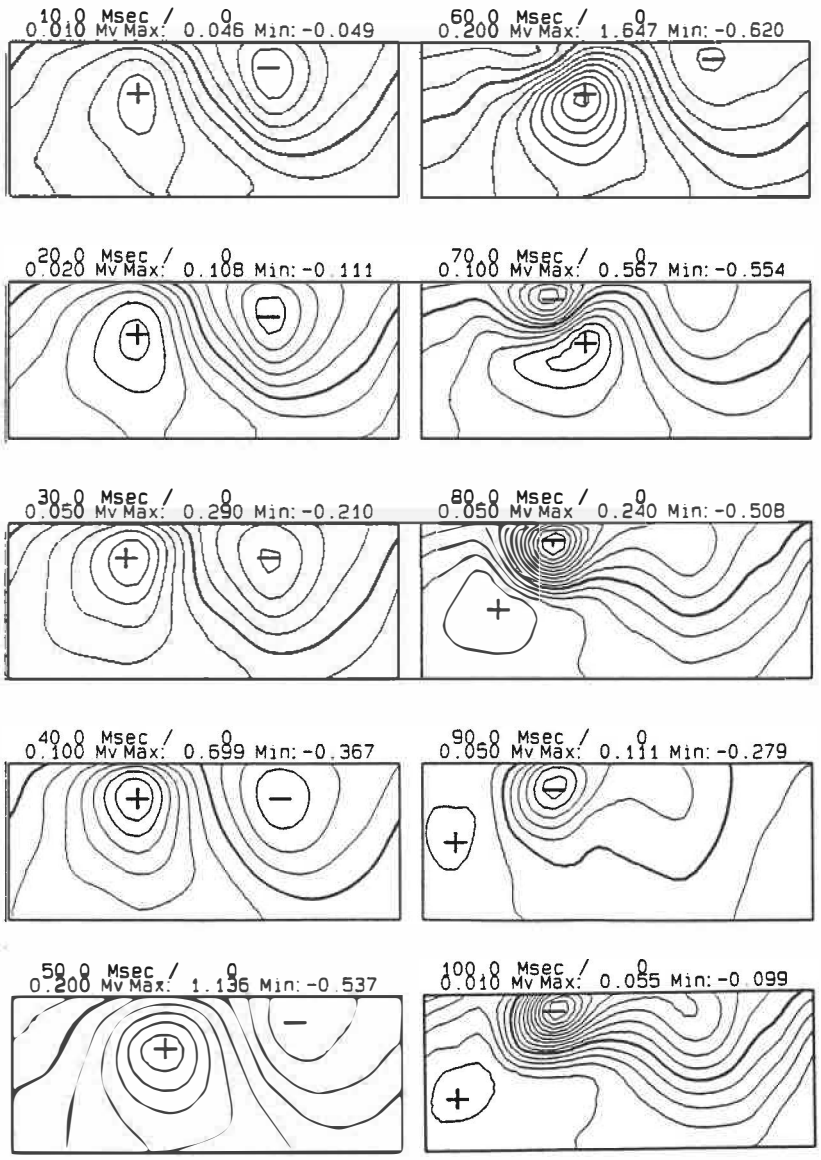

Figure D.1: Measured thoracic isopotential maps at $10 - 100ms$ time intervals. The torso surface is represented in a rectangular format with the anterior torso surface on the left and the posterior torso surface on the right.

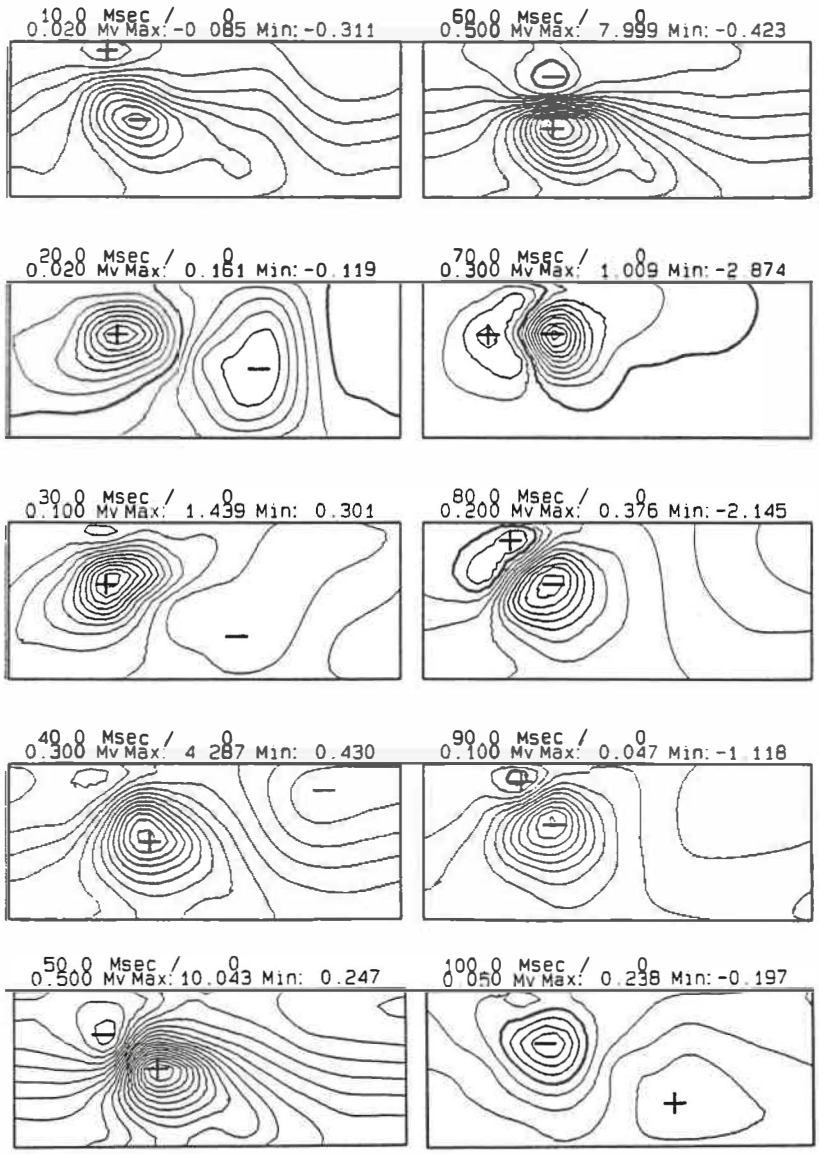

Figure D.2: Simulated thoracic isopotential maps using the T_1 model and the measured epicardial maps at $10 - 100ms$ time intervals.

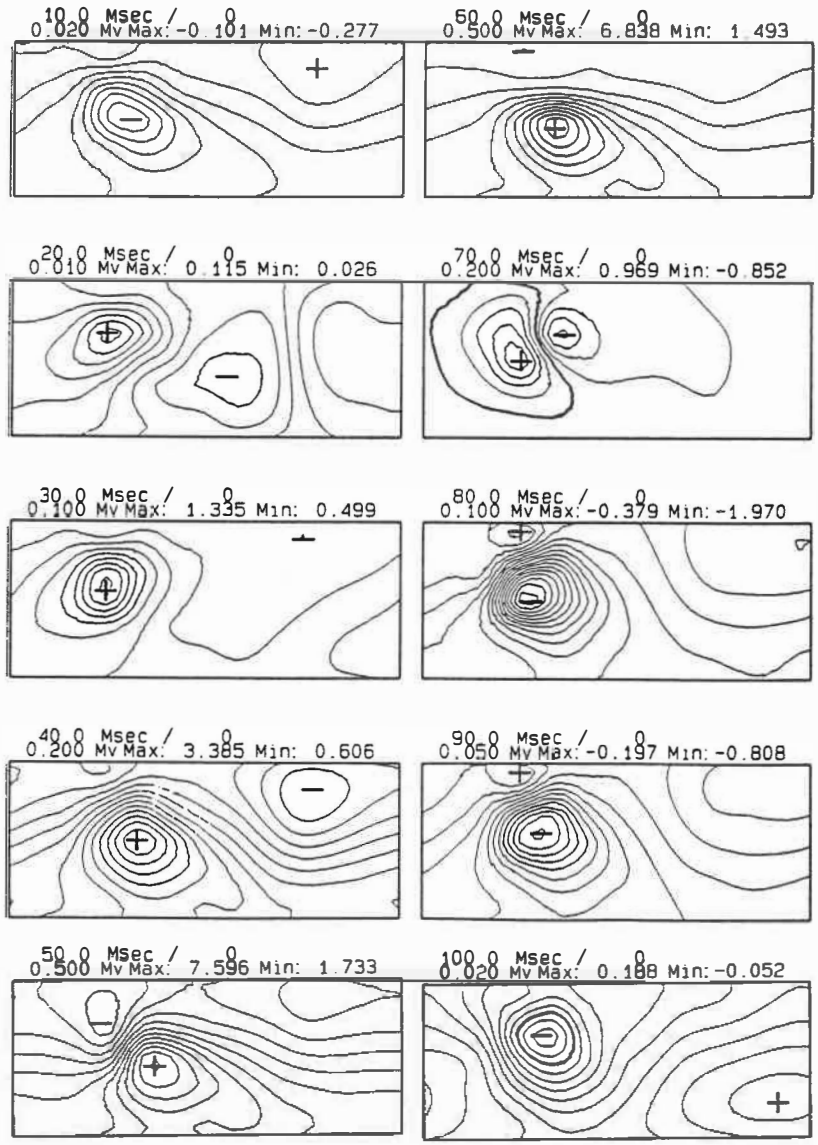

Figure D.3: Simulated thoracic isopotential maps using the LT_1 model and the measured epicardial maps at $10 - 100ms$ time intervals.

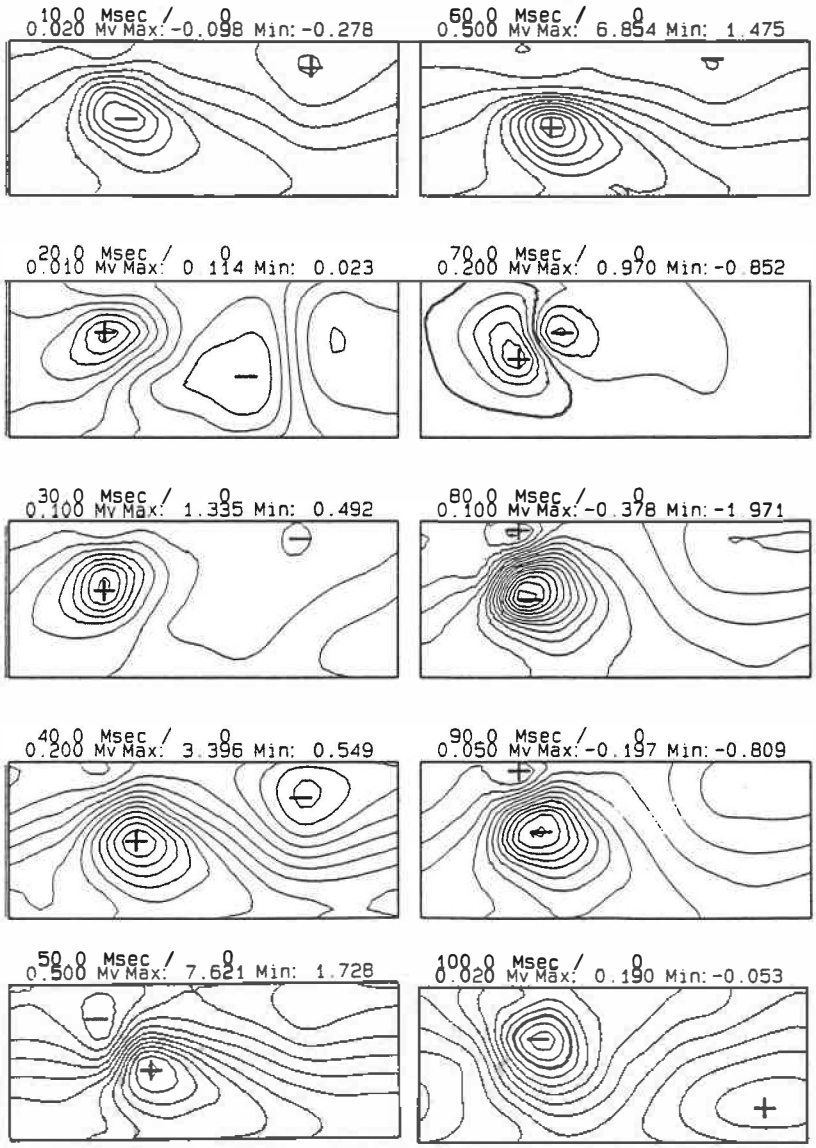

Figure D.4: Simulated thoracic isopotential maps using the $HLST_1$ model and the measured epicardial maps at $10 - 100ms$ time intervals.

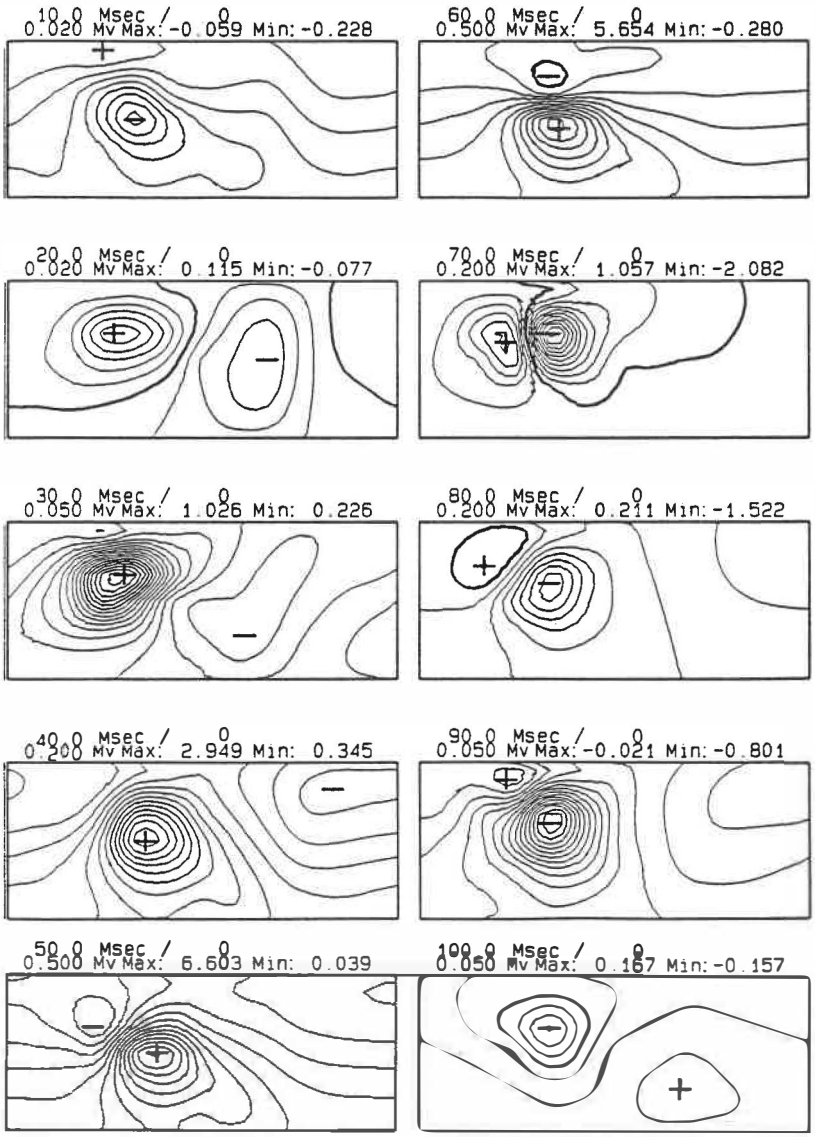

Figure D.5: Simulated thoracic isopotential maps using the T_2 model and the measured epicardial maps at $10 - 100ms$ time intervals.

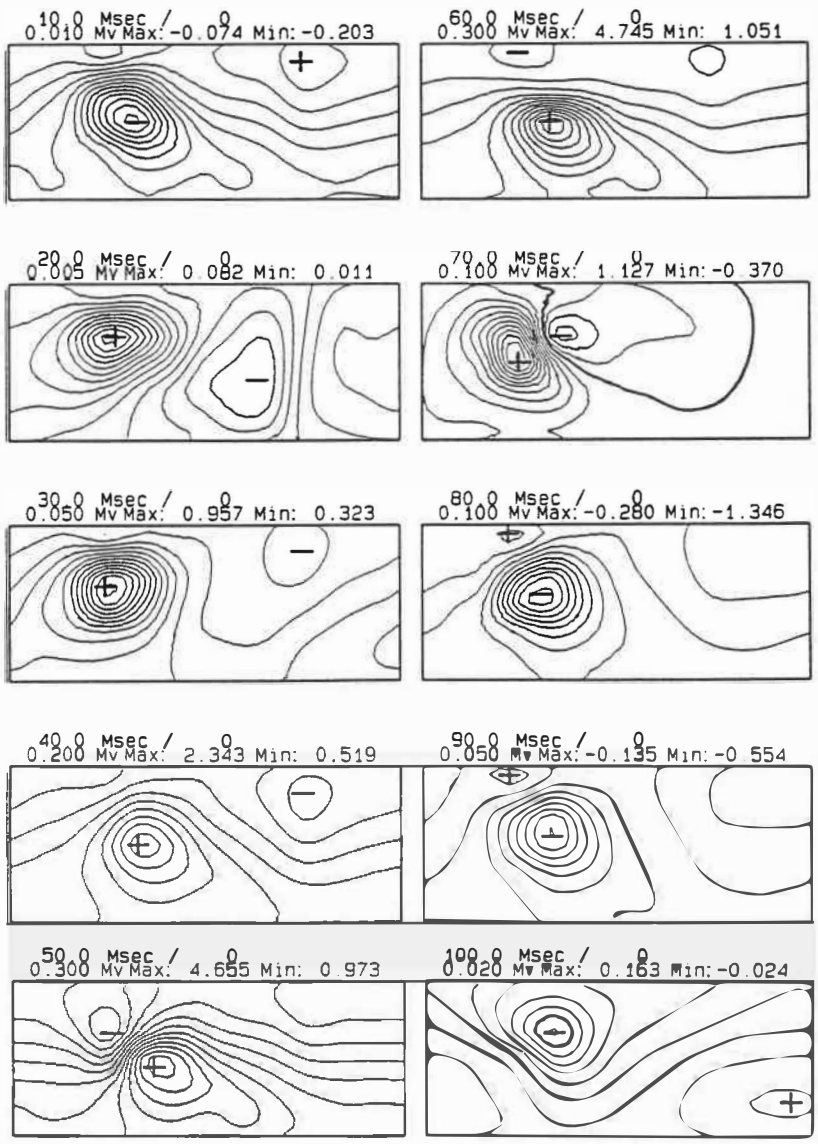

Figure D.6: Simulated thoracic isopotential maps using the LT_2 model and the measured epicardial maps at $10 - 100ms$ time intervals.

Appendix E

Transfer matrix

Solution to mixed boundary value problem of forward problem of electrocardiography results

$$\begin{pmatrix} S_{bb} & S_{bh} & S_{bf} \\ 0 & I & 0 \\ S_{fb} & S_{fh} & S_{ff} \end{pmatrix} \begin{pmatrix} \hat{\Phi}_b \\ \hat{\Phi}_h \\ \hat{\Phi}_f \end{pmatrix} = \begin{pmatrix} 0 \\ \Phi_h \\ 0 \end{pmatrix} \tag{E.1}$$

where,

$$\begin{aligned} \hat{\Phi}_b &\equiv \textit{Body surface potentials}, \\ \hat{\Phi}_h &\equiv \textit{Epicardial potentials}, \\ \hat{\Phi}_b &\equiv \textit{Free node potentials}, \\ \Phi_h &\equiv \textit{Prescribed epicardial potentials}. \end{aligned} \tag{E.2}$$

Eliminate the third row of equation (E.1), then we get

$$\hat{\Phi}_f = -S_{ff}^{-1}(S_{fb}\hat{\Phi}_b + S_{fh}\hat{\Phi}_h) \tag{E.3}$$

S_{ff} is a square matrix, well behaved generally, after substitution of equation (E.3) into equation (E.1), yields

$$\hat{\Phi}_h = \Phi_h \tag{E.4}$$

which describes the Dirichlet boundary conditions and

$$H\hat{\Phi}_h = \hat{\Phi}_b \tag{E.5}$$

where

$$H = (S_{bb} - S_{bf}S_{ff}^{-1}S_{fb})^{-1}(S_{bh}S_{ff}^{-1}S_{fh} - S_{bh}) \tag{E.6}$$

Equation (E.5) describes the relation between the epicardial and body surface potentials.

ÉCOLE POLYTECHNIQUE DE MONTRÉAL
3 9334 00278417 9

VAH

C
U
1
V